

NANO-SCALE TRANSPORT MECHANISMS ASSOCIATED WITH THREE-PHASE
CONTACT LINES

By

SHALABH CHANDRA MAROO

A DISSERTATION PRESENTED TO THE GRADUATE SCHOOL
OF THE UNIVERSITY OF FLORIDA IN PARTIAL FULFILLMENT
OF THE REQUIREMENTS FOR THE DEGREE OF
DOCTOR OF PHILOSOPHY

UNIVERSITY OF FLORIDA

2009

© 2009 Shalabh Chandra Maroo

To my parents for their endless love and support

ACKNOWLEDGMENTS

I am greatly thankful to my advisor, Dr. Jacob N. Chung, for all the time and efforts he has put in towards mentoring my dissertation work. I am indebted to him for his invaluable guidance, support and encouragement. His dedication and hard work towards research will be an everlasting source of inspiration for me.

I express my sincere gratitude to Dr. S. Balachandar, Dr. Youping Chen, Dr. Hai-Ping Cheng and Dr. James F. Klausner for serving as my supervisory committee members. Their precious advice and recommendations have considerably helped improve this work. My special acknowledgement goes to all my colleagues in my research group, especially, Tae-Seok Lee, Dr. Yun Whan Na and Dr. Cheng-feng Tai, with whom discussions have been very insightful and helpful. My utmost appreciation goes to my parents and family for their endless love and support which I have been blessed with in my life.

TABLE OF CONTENTS

	<u>page</u>
ACKNOWLEDGMENTS	4
LIST OF TABLES	8
LIST OF FIGURES	9
ABSTRACT	14
CHAPTER	
1 INTRODUCTION AND LITERATURE REVIEW	16
Introduction.....	16
Need for Molecular Dynamics Simulation	18
Literature Review	20
Nucleate Boiling.....	20
Critical Heat Flux	27
Droplet Impact and Spreading.....	28
Wall Models	34
Ultrathin Films, Disjoining Pressure and Hamaker Constant	37
Capillary Pressures at Nanoscale.....	41
Research Objectives.....	46
2 THEORY AND APPROACH	50
Molecular Dynamics Simulation	50
Force Calculation Algorithm	51
Brute Force Method.....	52
Linked List Method	52
Integrator Method	53
Non-Dimensional Units	53
Boundary Conditions	55
Periodic Boundary Condition (PBC).....	55
Mirror Boundary Condition.....	55
Thermal Wall Boundary Condition	56
Initial Structure	56
Simulation Stages	57
Statistical Sampling	58
Density.....	58
Energy.....	58
Temperature.....	59
Heat Flux	59
Thermal Conductivity.....	60
Pressure.....	60

Pressure Verification	61
Distinguishing Between Liquid Atoms and Vapor Atoms for Argon	65
Fluid-Wall Thermal Equilibrium Model	66
Model Validation	70
Internal energy and thermal conductivity	70
Heat equation	73
Maxwell speed distribution	82
Adiabatic Walls	85
3 TRANSIENT FILM EVAPORATION	88
Transient Film Evaporation	88
Heat Flux and Evaporation Rates	96
Evaluation of Hamaker Constant from Molecular Dynamics Simulation	96
Parameters Governing the Formation of Non-Evaporating Film	100
Heat Flux, Evaporation Flux, Hamaker Constant for Nanochannel	105
Varying Nanochannel Height h	106
Varying Film Thickness t_{film}	108
Vapor Pressure-Density Plots	111
Case 7 – Simultaneous Evaporation and Condensation	113
4 NANO-DROPLET IMPACT ON A HOMOGENEOUS SURFACE	116
Evaluation of Drop Temperature	117
Evaluation of Interface Markers, Interfacial Fit and Contact Angle	117
Droplet Impingement – Case 1	118
Droplet Impingement – Case 2	121
Droplet Impingement – Case 3 and Case 4	123
5 MENISCUS EVAPORATION AT NANOSCALE	125
Simulation Model	125
Results and Discussion – Case I	133
Results and Discussion – Case II	142
Meniscus Boundary Condition	148
Analytical Meniscus Boundary Condition	148
Curve-Fitted Meniscus Boundary Condition	150
6 CONCLUSION AND FUTURE WORK	153
Conclusion	153
Proposed Thermal Wall Model	153
Transient Film Evaporation	154
Simulation of Seven Cases in Nanochannel Film Evaporation	154
Nano-Droplet Impact on a Homogeneous Surface	155
Meniscus Evaporation at Nanoscale	156
Future Work	157
Molecular Dynamics Simulation (Nano Region)	157

Coarse-Grained Method (Micro Region)	159
Finite Volume Method (Macro Continuum Region).....	159
Multi-Scale Model and Matching Procedure	160
MD simulation and MD-CG matching (nano-micro matching).....	160
CG and FVM matching (micro-macro matching).....	161
LIST OF REFERENCES	163
BIOGRAPHICAL SKETCH	171

LIST OF TABLES

<u>Table</u>	<u>page</u>
2-1 Dimensionless Parameters	54
2-2 Simulation parameters for pressure verification	62
2-3 Change in internal energy for validation of proposed wall heat transfer model.....	73
2-4 Thermal conductivity for validation of proposed wall heat transfer model.....	73
3-1 Parameters for seven cases simulated in nanochannel.....	101
3-2 Case 1-3 results for film evaporation in nanochannel	108
3-3 Case 2, 4-6 results for film evaporation in nanochannel	109

LIST OF FIGURES

<u>Figure</u>	<u>page</u>
1-1	Flowchart showing the basic structure of molecular dynamics simulation17
1-2	Schematic of bubble growth, (a) overall picture at macro-scale (shaded region depicts the area covered by non-evaporating thin film), and (b) zoomed in nano- and micro-scale regions at the three-phase contact line21
1-3	Single Bubble Ebullition Cycle23
1-4	Expected variation of film thickness with film thickness37
1-5	Gradual and complete film evaporation simulated by Yi et al. (2002).....41
1-6	Phase diagram of water (Angell, 1988)45
1-7	Schematic of water phase diagram showing a metastable capillary bridge. The capillary bridge under tension acts like a water tube sealed with a piston, which leads to negative pressure. (Yang et al., 2008)45
1-8	Optical micrograph of a water plug in a 100 nm wide nanochannel (Tas et al., 200346
1-9	(a) Optical image (b) Schematic of water meniscus between a cantilever and a flat surface (Nosonovsky and Bhushan, 2008).....46
2-1	Arrangement of Pt wall atoms in fcc(111) structure; (a) 3-D view of the first three layers, (b) X-Y projection (top view) of the wall atoms57
2-2	Sketch for pressure contribution of atoms i, j61
2-3	Simulation domain at an intermediate timestep for pressure verification63
2-4	Temperature-density plot for liquid slab surrounded by vapor atoms63
2-5	Pressure-density plot for liquid slab surrounded by vapor atoms64
2-6	Surface tension-pressure plot for liquid slab surrounded by vapor atoms64
2-7	Plot to obtain the threshold number density and threshold radius for saturated liquid argon at 90 K66
2-8	Fluid-wall thermal equilibrium model68
2-9	Computational domain at an intermediate timestep for validation of proposed wall heat transfer model71

2-10	Variation of temperature and energy with time for validation of proposed wall heat transfer model (a) lower wall temperature is increased to 110 K while the upper wall temperature is decreased to 90 K; (b) lower wall temperature is increased to 130 K and the upper wall decreased to 90 K.....	72
2-11	1-D heat problem	74
2-12	Average temperature and energy variation with time of liquid argon time for validation of proposed wall heat transfer model.....	76
2-13	Temperature gradient along z-direction at different timesteps for $T_i=100$ K, $T_{up}=110$ K and $T_{low}=90$ K (smooth lines represent analytical solutions).....	79
2-14	Temperature gradient along z-direction at different timesteps for $h=23.657$ nm, $T_i=100$ K, $T_{up}=120$ K and $T_{low}=120$ K (smooth lines represent analytical solutions).....	80
2-15	Temperature gradient along z-direction at different timesteps for $h=44.357$ nm, $T_i=100$ K, $T_{up}=120$ K and $T_{low}=120$ K (smooth lines represent analytical solutions).....	81
2-16	Average domain temperatures from MD simulation and analytical equation with heating from both platinum walls for different nanochannel heights	82
2-17	Variation of number of liquid atoms with time in the simulation for verification with Maxwell Speed Distribution function.....	84
2-18	Velocity distribution of vapor argon atoms at final equilibrium with a non-evaporating film at the lower wall	85
2-19	Variation of average temperature and energy with time for adiabatic wall with higher wettability $\varepsilon = 0.894 \times 10^{-21}$ J	86
2-20	Variation of average temperature and energy with time for adiabatic wall with lower wettability $\varepsilon = 0.358 \times 10^{-21}$ J.....	87
3-1	Snapshot of transient film evaporation domain	89
3-2	Variation of average system temperature and energy with time for transient film evaporation.....	90
3-3	Variation of liquid film argon atoms in the domain with time for transient film evaporation.....	91
3-4	Projection of the Y-Z plane of the simulation domain at different time intervals for transient film evaporation	93
3-5	Number density profiles at different time steps for transient film evaporation	94
3-6	Averaged temperature distribution profile for transient film evaporation.....	94

3-7	Averaged number density profile for transient film evaporation.....	95
3-8	Evaporation flux and heat flux rates for transient film evaporation	97
3-9	Sketch showing the coordinates for calculating the interaction energy between (a) a Pt atom and Ar block (b) semi-infinite Pt block and Ar block	98
3-10	Snapshot of simulation domain of nanochannel	101
3-11	Variation of average system temperature and energy with time for case 4	102
3-12	Variation of vapor argon atoms with time for case 4.....	103
3-13	Snapshots of domain for case 4	104
3-14	Average density of domain at different times for case 4	104
3-15	Density-height plot showing non-evaporating liquid film thickness and equimolar surface position for case 6.....	105
3-16	Heat flux rate with time for varying nanochannel height (cases 1-3).....	107
3-17	Evaporation rate with time for varying nanochannel height (cases 1-3)	107
3-18	Heat flux rate with time for varying film thickness (cases 2, 4-6)	110
3-19	Evaporation rate with time for varying film thickness (cases 2, 4-6).....	110
3-20	Pressure-density plot of initial and final states for varying nanochannel height (cases 1-3).....	112
3-21	Pressure-density plot of initial and final states for varying film thickness (cases 2, 4-6)	113
3-22	Vapor pressure variation with time for case 7	114
3-23	Snapshots of domain at different time intervals for case 7.....	115
4-1	Variation of drop temperature and energy with time for drop impact (case 1)	119
4-2	Variation of drop-center height and drop velocity with time for drop impact (case 1) ...	119
4-3	Snapshots of x-z plane for drop impact (case 1).....	120
4-4	Variation of contact angle with time for drop impact (case 1)	121
4-5	Snapshots of x-z plane for drop impact (case 2).....	122
4-6	Variation of drop center height and drop velocity with time for drop impact (case 2) ...	122

4-7	Variation of contact angle with time for drop impact (case 2)	123
4-8	Snapshots of y-z plane for drop impact (case 3).....	124
4-9	Snapshots of y-z plane for drop impact (case 4).....	124
5-1	Schematic showing configuration of the computational domain.....	127
5-2	3D schematic of the computational domain.....	128
5-3	Schematic depicting division of nanochannels and liquid meniscus into 11 regions	130
5-4	Schematic showing two regions of an evaporating meniscus at times t_1 and t_2	131
5-5	Snapshots of x-z plane at different time steps for Case I.....	134
5-6	Variation of liquid atoms with time for regions 5-10 for Case I	135
5-7	Variation of vapor pressure with time for Case I.....	137
5-8	Average temperature of regions at initial and final time periods for Case I.....	137
5-9	Average heat and evaporation flux rates for regions 1-10 during the total heating period for Case I.....	139
5-10	Heat flux distribution along nano- and micro-layers at the base of the bubble	139
5-11	Variation of disjoining pressure along meniscus length for Case I	141
5-12	Variation of capillary pressure along meniscus length for Case I	141
5-13	Snapshots of x-z plane at different time steps for Case II	143
5-14	Variation of liquid atoms with time for regions 5-10 for Case II.....	144
5-15	Average temperature of regions at initial and final time periods for Case II	146
5-16	Average heat and evaporation flux rates for regions 1-10 during the total heating period for Case II	146
5-17	Variation of disjoining pressure along meniscus length for Case II.....	147
5-18	Variation of capillary pressure along meniscus length for Case II.....	147
5-19	(a) Schematic of a meniscus to compute forces acting by the extended meniscus region on liquid atoms in the bounded meniscus region, and (b) configuration for force interaction between an atom and a rectangular region	150

5-20	Schematic showing meniscus and nanochannels used in the present work to determine the force distribution along the meniscus length by the nanochannels.....	151
5-21	Force distribution on the meniscus by the nanochannel as a function of the distance from the nanochannel (a) F_x and F_y , (b) F_z	152
6-1	Schematic showing multi-scale method of solution for proposed work.....	158
6-2	Domain Decomposition method	162

Abstract of Dissertation Presented to the Graduate School
of the University of Florida in Partial Fulfillment of the
Requirements for the Degree of Doctor of Philosophy

NANO-SCALE TRANSPORT MECHANISMS ASSOCIATED WITH THREE-PHASE
CONTACT LINES

By

Shalabh Chandra Maroo

December 2009

Chair: Jacob N. Chung
Major: Mechanical Engineering

Nucleate boiling is one of the most efficient heat transfer mechanisms and has been widely featured in many high heat-flux engineering applications. But, the knowledge on the underlying basic transport mechanisms is quite limited and rather incomplete, due to the lack of fundamental understanding of the physics occurring at the three-phase contact line. The contact line region comprises of non-evaporating thin film region, evaporating thin film region and intrinsic meniscus region. The non-evaporating thin film is the main focus in this work. Its thickness is expected to be in the size of nanometers, and thus is studied here using molecular dynamics simulations. A novel ‘fluid-wall thermal equilibrium model’, to numerically simulate heat transfer between wall and fluid atoms, is proposed and verified against available experimental data and analytical methods. Nanoscale phase change process is studied by simulating evaporation of a thin liquid argon film on a platinum wall using the proposed model. A non-evaporating film is obtained on the platinum surface, and its Hamaker constant is evaluated. Additional simulations of thin film evaporation are done in a nanochannel to study the effect of varying nanochannel height and film thickness. Hamaker constant, vapor pressure, film thickness, and net evaporation and heat fluxes are evaluated. It is concluded that the creation of non-evaporating film is dependent on vapor pressure, substrate temperature and solid-liquid

molecular interaction strength. The vapor pressure and substrate temperature are dominant factors. Next, a nanoscale evaporating meniscus is simulated. Heat and mass transfer characteristics and pressure variation in the non-evaporating and interline regions are studied. High disjoining pressure and negative capillary pressures are obtained. It is shown that cavitation cannot occur as the capillary size is smaller than the critical cavitation radius, and the meniscus can exist in metastable state. A curve-fitted meniscus boundary condition is developed; a force function of the form $F_n = An^{-3} - Cn^{-2}$ can be applied at the boundaries of a liquid film to create curvature and form a meniscus. Also, impact of argon nano-droplet on platinum wall with varying wettability is simulated to study the variation of contact angle with time.

CHAPTER 1

INTRODUCTION AND LITERATURE REVIEW

Introduction

The advent of the computer sparked the interest in simulations on a molecular scale. Not many years after the digital computers appeared that the very first molecular simulations were performed. Since then, the spectacular growth in the computational power of the computer has made possible the usage of molecular simulations in solving problems of increasing complexity. As every substance is made from elementary particles (atoms/molecules) and if the basic dynamic parameters of these atoms (i.e. position, velocity and interaction force) can be determined, the physical properties of the substance, like temperature, pressure, etc can be obtained from those dynamic parameters using statistical methods. This forms the basis of Molecular Dynamics simulations. Using molecular dynamics, it is possible to solve a dynamic problem without making any approximations, within the limits exposed by machine accuracy. All molecular dynamics simulations follow Newton's second law in its simple form for simple atomic systems or in a more generalized form (Lagrangian/Eulerian formulation) for complex geometry systems. Thus, molecular dynamics can also be understood as a "virtual experiment" since the movement of atoms occurs naturally and the system evolves with time as in a real experiment. Molecular dynamics simulation consists of three basic parts:

- 1) A model for interactions between various system components like atoms, molecules, surfaces, etc which is commonly known as molecular interaction potential function.
- 2) An integrator method to obtain the positions and velocities of the molecules as the system evolves with time.
- 3) A statistical analysis of the dynamics parameters to obtain properties such as temperature, energy, etc

Figure 1-1 shows a basic molecular dynamics algorithm flowchart. The force on each molecule by all other molecules in the system can be determined by using the molecular interaction potential function. From this force, the equation of motion can be integrated over time to obtain the new positions and velocities of each molecule. This information can be statistically analyzed by space/time averaging to provide macroscopic physical properties, and thus the evolution of the system can be studied.

It should be noted here that molecular dynamics approximates electronic distributions in a rather coarse-grained fashion by putting either fixed partial charges on interaction sites or by adding an approximate model for polarization effects. In both cases, the time scale of the system is not dominated by the motion of electrons, but by the time of intermolecular collision events, rotational motions or intramolecular vibrations which are orders of magnitude slower than those of electron motions (Sutmann 2002). Most of the molecular dynamics simulations till date have been restricted to *nano* length and time scales as they strongly depend on computing power available. Molecular dynamics is nowadays applied to a huge class of problems, e.g. phase change, properties of liquids, defects in solids, fracture, surface properties, friction, molecular clusters, polyelectrolytes and biomolecules.

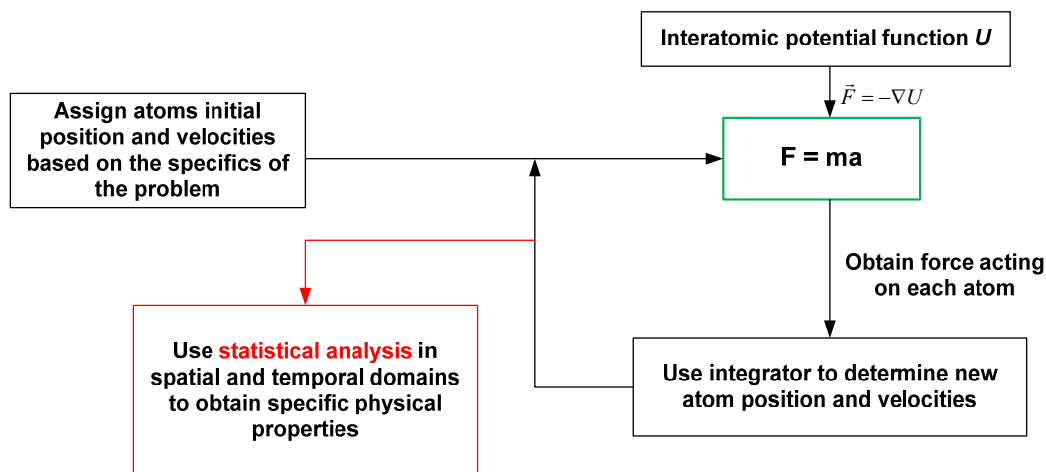


Figure 1-1. Flowchart showing the basic structure of molecular dynamics simulation

Need for Molecular Dynamics Simulation

Nucleate boiling is one of the most efficient heat transfer mechanisms and has been widely featured in many high heat-flux engineering applications. In many engineering applications, nucleate boiling heat transfer is the mode of choice. Boiling heat transfer has the potential advantage of being able to transfer a large amount of energy over a relatively narrow temperature range with a small weight to power ratio.

The critical heat flux, the maximum nucleate boiling heat flux, is closely related to the design and safe operation of boiling systems. But the knowledge on the underlying basic transport mechanisms is quite limited and rather incomplete, that has hindered development of a universal theory and corresponding model governing the boiling process from bubble dynamics and heat transfer during bubble growth and departure to critical heat flux phenomenon. This lack of fundamental understanding is the sole reason behind this work that is intended to unlock the core of the transport physics in boiling – a moving contact line with simultaneous heat and mass transfer.

The moving contact line is a three-phase phenomenon where immiscible gas-liquid interface meets the solid surface. Moving contact line is involved, usually playing the dominant role, in many natural and engineering processes such as rivulet, coating flows, and droplet impingement. Spray droplet cooling and heterogeneous nucleate boiling, both are highly effective heat transfer mechanisms, are dominated by the moving contact line with simultaneous heat and mass transfer around the contact line region. During nucleate boiling from a heated surface, vapor bubbles are nucleated and they start to grow owing to infusion of vapor mass generated mainly from the moving contact line region. The moving contact line moves outward during bubble growth period while it retracts back during the bubble departure stage. At higher heat fluxes, bubble-bubble interaction and coalescence are responsible mechanisms for achieving

high heat transfer rates in heterogeneous nucleate boiling where moving contact line also plays an important role. Bubble-bubble coalescence creates strong disturbances to the fluid mechanics and heat transfer of the micro-layer and the moving contact line beneath the bubbles. Because of the complicated nature, the detailed physics and its effects of moving contact line on the bubble-bubble interaction process have not yet been unveiled.

The critical heat flux on earth, which is the upper heat transfer limit in the nucleate boiling regime, represents a state of momentum and mass balance. Because the buoyancy force strength is relatively constant on earth, for heat fluxes lower than the critical heat flux, this force is more than that required for a complete removal of vapor bubbles formed on the heater surface. At the critical heat flux, the buoyancy force is exactly equal to the force required for a total removal of the vapor bubbles. For heat fluxes greater than the critical heat flux, the buoyancy force is unable to remove all the bubbles, thus resulting in the accumulation and merging of bubbles on the heater surface, which simultaneously leads to a total blanketing of the heater surface by a layer of superheated vapor. It is believed that bubble departure and vapor removal from the heater surface is dominated by vapor generation and bubble coalescence, both of which are hinged on the moving contact line dynamics, as a result, the moving contact line is closely related to the critical heat flux.

The no-slip boundary condition between a fluid flow and a solid surface is generally regarded as a cornerstone in the continuum hydrodynamics, owing to its proven applicability in diverse fluid flows. However decades ago, it was discovered that in immiscible gas-liquid two-phase flows over a solid surface, the moving contact line, defined as the intersection between the moving gas-liquid interface and the solid surface, is incompatible with the no-slip boundary condition (Moffatt 1964, Huh and Scriven 1971, Dussan and Davis 1974, Dussan 1976 and

1979). These reports showed that there is velocity discontinuity at the MCL which is now well-recognized as the contact-line singularity (Shikhmurzaev 2006 and Blake 2006). In the past two decades, it has been confirmed through molecular dynamic simulations that a near-complete slip indeed takes place at the MCL (Koplik et al. 1988, Thompson and Robbins 1989, and Thompson et al. 1993). This finding presented a challenge for the fluid mechanics community, due to a lack of viable solutions apart from *ad hoc* fixes that include analytical models (Phan et al. 2006, Qian et al. 2006, and Fuentes and Cerro 2007) and numerical models (Ding and Spelt 2007a,b). In the absence of a viable boundary condition which can re-produce the molecular dynamics results, an accurate continuum description of the moving contact line flows at the micro- or nano-scale remains an elusive goal which may never be solved explicitly by continuum fluid mechanics.

Literature Review

Nucleate Boiling

It has been widely accepted in literature that the contact line at the base of the bubble in nucleate boiling can be divided into macro- and micro-regions. The micro region is the ultrathin liquid film between the solid surface and the evolving liquid-vapor interface. The macro region is the region occupied by vapor and liquid, except the microlayer. The micro-region can be subdivided into two additional regions. Thus the three regions, as shown in figure 1-2, are:

- a) Non-evaporating thin-film region – liquid is adsorbed on the heater surface and forms a non-evaporating layer with molecular forces having controlling influence
- b) Evaporating thin-film region – maximum evaporation and heat transfer occurs in this region and the liquid is fed from the bulk liquid through the intrinsic meniscus region
- c) Intrinsic meniscus region – fluid mechanics in this region is governed by the conventional equation of capillarity

There is a region between the non-evaporating thin film region and the evaporation thin film region over which the film varies in thickness and curvature to accommodate the transition between the two regions. This is called the interline region and is the thinnest portion of the meniscus over which vaporization can occur. Since it is the thinnest, it is also the location where the evaporation rate is the highest.

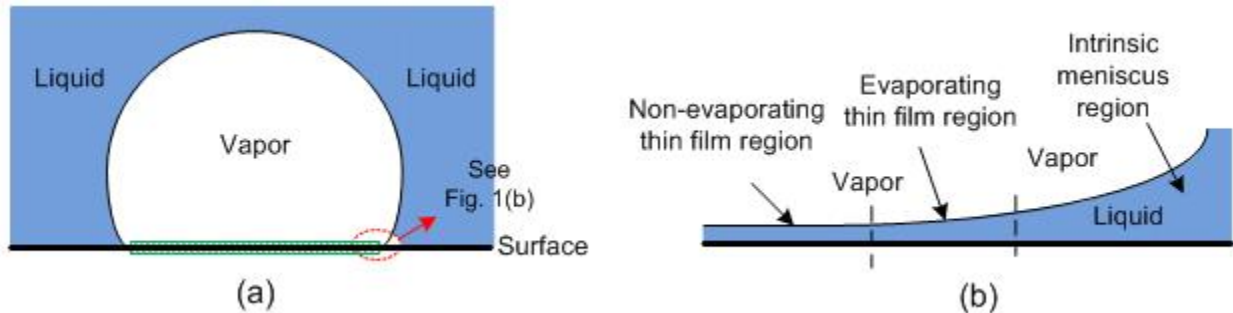


Figure 1-2. Schematic of bubble growth, (a) overall picture at macro-scale (shaded region depicts the area covered by non-evaporating thin film), and (b) zoomed in nano- and micro-scale regions at the three-phase contact line

Boiling has been studied extensively during the last few decades which include experimental work, and theoretical models to predict the exact nature of boiling in various conditions. Since the boiling process is very complex, its complete understanding still poses significant challenges and researchers have not converged on a definite precise model. The past efforts can be categorized into three broad groups (Dhir 2006):

- 1) Empirical correlations – experimental data was obtained for boiling heat transfer as a function of several independent variable like heater size, heating method, heater thickness, system pressure, liquid temperature, flow conditions, etc. This data was correlated by many researchers. Although the correlations have been helpful in application to practical situations, they serve their useful purpose only when applied in the range of the database used in developing the correlations.

- 2) Mechanism-based correlations – This involved studying some of the individual subprocesses to develop mechanistic models for predicting heat fluxes as a function of wall superheat or other independent variables. An expression for partial nucleate boiling heat flux was written based on the contributions of three mechanisms by: transient conduction into the liquid during the waiting period over the region influenced by vapor bubbles, natural convection over the remaining regions of the heater and evaporative heat transfer from the microlayer underneath the bubble. The expression required the knowledge of three key parameters: number density of active sites, bubble diameter at departure and bubble release frequency. A number of attempts have been made to develop correlations or models for these parameters, but with limited success.
- 3) Numerical simulation – In order to have a credible predictive model of nucleate boiling, one must include all subprocesses which occur and not guess how one parameter influences the overall process. Thus, a complete numerical simulation of the process is asked for – a tool which has been developed only recently. The region of interest is divided into micro- and macro- regions as mentioned before. Lubrication theory has been widely used to solve for the radial variation of microlayer thickness, while complete conservation of mass, momentum and energy are solved for both phases in the macroregion.

As reported in Chen and Chung (2002, 2003a), a typical ebullition cycle for a single bubble is composed, as shown in Figure 1-3, of two basic stages: (1) bubble nucleation (Step A) which takes place spontaneously with the departure of the preceding bubble (Step F), and (2) bubble growth (Steps B, C, D and E). There is only one heat flux spike for a single bubble ebullition cycle that is the result of the combined bubble departure and nucleation process. The boiling heat

transfer is closely associated with the bubble's contact line movement and dry area on the heater surface.

Chen and Chung (2003b) and Chen et al. (2004) further examined the effects of heater size on the boiling characteristics. They concluded that the boiling curve obtained from the microheater is composed of two regimes which are separated by a peak heat flux. It is suggested that in the lower superheat regime, the boiling is dominated by liquid rewetting and micro-layer evaporation, while in the higher superheat regime, conduction through the vapor film and micro-convection plays the key heat transfer role as the heater is covered by vapor all the time.

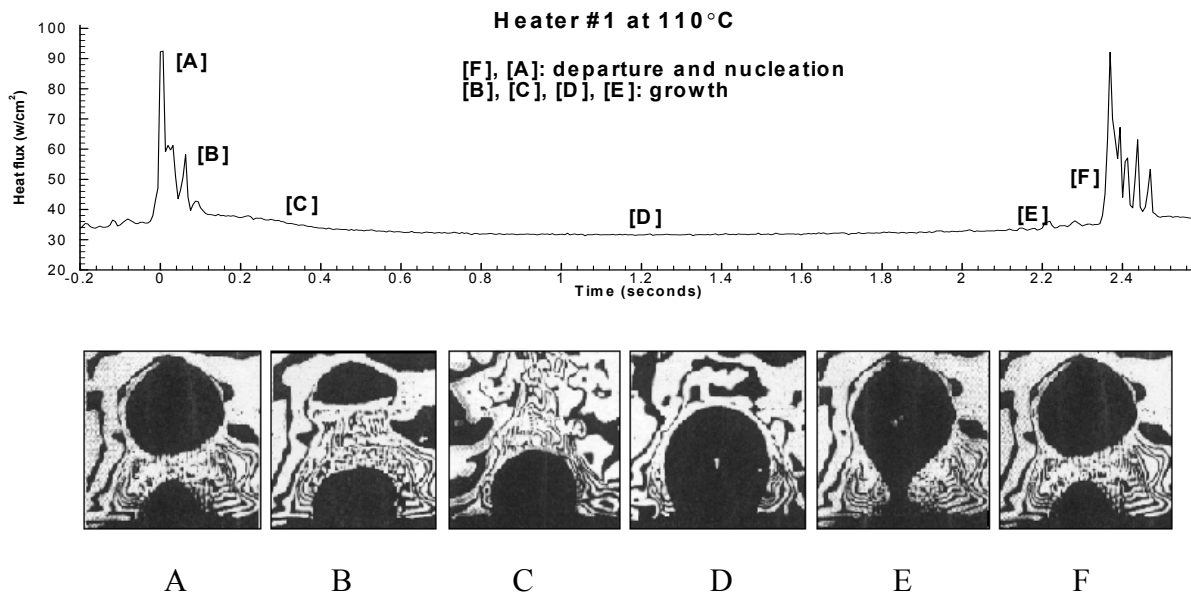


Figure 1-3. Single Bubble Ebullition Cycle

Liao et al. (2004) presented a physical model to predict the early stage bubble growth in saturated heterogeneous nucleate boiling. The microlayer was taken to be in the form of a wedge. The structure of the thin unsteady liquid thermal boundary layer is revealed by the asymptotic and numerical solutions. The authors find that in some cases, the heat transfer from the thin

unsteady thermal boundary layer near the rapidly growing bubble can be larger than that from the microlayer.

Son (2001) proposed a numerical method based on a level set technique for capturing the phase interface which included the effect of phase change at the interface as well as to achieve mass conservation. The modified level set method was applied for numerical simulation of bubble rise and growth in a stationary liquid. Wu et al. (2007) coupled the level set method with the moving mesh method to simulate subcooled nucleate boiling.

Genske and Stephan (2006) modeled the macro-region by solving the Navier-Stokes equation for both vapor and liquid phase using finite element method. The microregion was wedge shaped and moving mesh was used for free surface simulation. Flow inside and around a growing bubble and its influence on the overall heat transferr was considered.

Tomar et al. (2005) used the coupled level-set and volume-of-fluid method to simulate bubble growth in water at near critical pressure for different degrees of superheat. The coupled algorithm was said to conserve mass and capture the complicated interfaces very accurately. The effect of superheat and saturation pressure on frequency of bubble formation was analyzed.

Mukherjee and Dhir (2004) numerically studied bubble dynamics and associated wall heat transfer during lateral bubble merger. They solved the incompressible Navier-Stokes equation and captured the liquid-vapor interface using the level set formulation. Mergers of two bubbles, three bubbles in a line and three bubbles in a plane were simulated assuming axisymmetry. The contact angle between the wall and the bubble was taken to be constant throughout the simulation. The authors acknowledge the fact that the results are sensitive to contact angle.

Mukherjee and Kandlikar (2007) used a static contact angle and dynamic contact angle models based on the contact line velocity and the sign of contact line velocity to numerically study the growth and departure of single vapor bubbles from a heated wall. The liquid-vapor interface is simulated using the level-set technique. The effect of microlayer evaporation at the bubble base was neglected. The authors concluded that correct motion of the contact line can be simulated when the dynamic contact angle is represented as a function of interface velocity. However, the numerical model was not validated with experimental results.

Recently, a few researchers attempted to observe nano-bubble nucleation using molecular dynamics simulations. Vapor nucleation in a liquid confined in a nanochannel cannot be achieved by increasing the temperature of the wall only. Hence, the studies were associated with varying system pressure by using metastable liquid, increasing the nanochannel volume and thermally contract the liquid by lowering the temperature. The nucleation occurs when the pressure reached the spinodal line.

Maruyama and Kimura (2000) simulated heterogeneous nucleation of vapor bubble on a solid surface using molecular dynamics in a nanochannel. Liquid argon was placed between parallel solid platinum surfaces and gradually expanded until a vapor bubble was nucleated. The wettability of the lower surface was varied by changing the potential parameter between argon and solid molecule.

Nagayama et al. (2006) carried out molecular dynamics simulations to examine the bubble behavior confined in a nanochannel with emphasis on nucleation phenomenon. A metastable liquid confined in a nanochannel with an inlet driving force was simulated. Nano-sized bubbles were observed under different conditions of solid-liquid interfacial wettability. The authors also found that the vapor pressure inside the nano-bubble disagrees with the macroscopic

Young-Laplace equation. Park et al. (2001) formed a similar bubble using molecular dynamics with the liquid initially in metastable condition. No solid surfaces were included in this simulation. The surface tension of the bubble, calculated from the density profile and from the normal and transverse components of pressure tensor, was found to increase very slightly with decrease of bubble radius.

Schoen et al. (2005) investigated the phase transition of a simple liquid bounded between two parallel walls a few nanometers apart with molecular dynamics simulation. The authors used the fact that since some fluids (argon in their case) thermally contract on cooling, the lower wall temperature was reduced to the extent that the fluid started to crystallize starting from the bottom surface creating a “frozen” bubble in crystallized state. It was found that the confining walls primarily affect the crystallization process. The authors also noted that vapor nucleation in a liquid confined in a nanochannel cannot be achieved by increasing the temperature of the wall only.

Wu and Pan (2003) studied bubble nucleation in a homogeneous Lennard-Jones liquid under heating with a constant mean negative pressure using molecular dynamics. Velocity-scaling temperature control is used to raise the system temperature while the system volume is expanded to keep the mean pressure nearly constant. No solid surfaces were included in the simulation. Bubble nucleation is observed as the system pressure-temperature reaches the spinodal line. The authors find very good agreement of nucleation rate between simulation and prediction from classical theory.

Ren and E (2007) studied the physical process near a moving contact line using molecular dynamics by placing two species of fluid particles between two solid walls and then shearing the walls with a constant speed in opposite directions. This simple geometry was chosen

based on the assumption that the outer flow does not change the physics of the inner region at this length scale. They evaluated the friction force and stresses around the contact line region and suggested boundary conditions, based on force balance, at the contact line and at the wall away from the contact line. The authors implemented these boundary conditions in a continuum model by solving the incompressible Navier-Stokes equation for a similar setup by having two immiscible fluids confined between two parallel solid walls with external force acting on the fluid. The two fluids interact identically with the wall, and values for the different parameters in the boundary conditions were assumed. The dependence of the apparent and dynamic contact angles on the contact line velocity and friction coefficient was studied. The authors concluded that: (a) shear rates are well described by linear models for all practical purposes, (b) Young's stress dominates over the viscous stress inside the contact line region, and (c) the Navier boundary condition describes the friction dynamics at the fluid-solid interface away from the contact line region accurately. The authors point out the fact that further work needs to be done in order to study more complex processes.

Critical Heat Flux

The boiling curve was first identified by Nukiyama (1934) more than sixty years ago. Since then the critical heat flux has been one of the major focus of boiling heat transfer research. A plethora of empirical correlations for the critical heat flux are now available in the literature, although each is applicable to somewhat narrow ranges of experimental conditions and fluids. There have been three mechanistic models suggested in the past : 1) vapor escape path instability model (Zuber, 1959, Lienhard and Dhir, 1973), 2) macrolayer dryout model (Haramura and Katto, 1983) and 3) vapor stem merging model (Dhir and Liaw, 1989).

Sakashita and Kumada (1993) proposed that the critical heat flux is caused by the dryout of a liquid layer formed on a heating surface. They also suggested that a liquid macrolayer is

formed due to the coalescence of bubbles for most boiling systems, and that the dryout of the macrolayer is controlled by the hydrodynamic behavior of coalesced bubbles on the macrolayer. Based on these considerations, a new critical heat flux model is proposed for saturated pool boiling at higher pressures. In the model, they suggest that a liquid macrolayer is formed due to coalescence of the secondary bubbles formed from the primary bubbles. The detachment of the tertiary bubbles formed from the secondary bubbles determines the frequency of the liquid macrolayer formation. The critical heat flux occurs when the macrolayer is dried out before the departure of the tertiary bubbles from the heating surface.

Sadasivan et al. (1995) suggested that identifying the physical characteristics such as active nucleation site distribution, static versus dynamic contact angles, and advancing versus receding angles would help understand the heater surface rewetting behavior, thus again showing the importance of microlayer region. The consensus is that a satisfactory overall mechanistic description for the critical heat flux still remains elusive.

Droplet Impact and Spreading

Droplets are encountered in day-to-day life and the phenomena related to them are so common that they are usually overlooked. The basic physics of droplet dynamics is extremely intriguing and understanding them in detail is of immense scientific significance. The act of droplet impingement and spreading can be seen in a wide range of applications like spray cooling of surfaces (semiconductor chips, electronic devices, etc), spray combustion, ink-jet printing, lubrication, crop spraying, etc. Thus, droplet impact dynamics can be accompanied by mass, momentum and energy transfer. The spreading phenomenon is governed by the dynamic contact angle and the moving contact line. Full characterization of the effect of the surface wettability and roughness on droplet growth is still to be achieved, and there is no complete

agreement on the boundary conditions to be implemented at the moving contact line. Oblique impacts of droplets are also insufficiently studied and understood.

Droplet impact and spreading on horizontal surfaces have been studied on the continuum level by many researchers. Fukai et al. (1993) studied the deformation of a spherical droplet impingement on a surface using deforming finite elements and grid generation. The singularity at the contact line is removed by imposing a net interfacial force given by the equilibrium surface-tension coefficients of the joining phases during flow with the capillary force neglected at the contact line. They used two fluids: water and tin in their simulations and showcased the occurrence of droplet rebounding and mass accumulation around its periphery on spreading.

Davidson (2000) analyzed the axisymmetric spreading of an inviscid drop impingement on a solid surface using a boundary integral method for different Weber numbers. The author concluded that surface tension forces are responsible for the accumulation of liquid in a rim around the periphery of the spreading drop for low Weber numbers, whereas viscous forces govern the accumulation for high Weber numbers. Reznik and Yarin (2002) studied the spreading of an axisymmetrical drop on a horizontal surface under the influence of gravity and surface tension for different Bond numbers by assuming inertial forces to be negligible and using the creeping flow regime approximation.

Francois and Shyy (2003) applied the immersed boundary method to simulate droplet impact on a flat surface with heat transfer. Both the static and dynamic contact angle models were considered. The computed 3D drop shapes compared well with the previous experimental results. The wall heat flux distribution under the droplet was governed by its dynamics with a larger spread resulting in a wider area of heat exchange.

Fedorchenko et al. (2005) studied the late-stage of drop spreading by modifying the sheet flow equations to account for the viscous drag and obtained an analytical solution. They also proposed a simplified kinematic model which takes into account viscous and capillary effects and shows the influence of Reynolds and Weber numbers on drop spreading dynamics.

Park et al. (2003) developed a theoretical model based on energy balance to predict the maximum spreading ratio at low impact velocity assuming the shape of the drop to be a spherical cap while spreading on the surface, and validated their model with experimental results showing good agreement between the two. Fukai et al. (1998) studied the maximum spreading diameter and spreading time for droplet impact on a surface by solving the Navier-Stokes equations for an axisymmetric system and neglecting the gravitational effect for a wide range of Reynolds and Weber number.

Pasandideh-Fard et al. (1996), Bussmann et al. (1999), Sikalo et al. (2005), Gunjal et al. (2005) and Lunkad et al. (2007) simulated the droplet impact and spreading using the volume-of-fluid (VOF) method. Pasandideh-Fard et al. (1996) solved the Navier-Stokes equation using a modified SOLA-volume of fluid method to model drop impact on surfaces. Experimentally measured values of dynamic contact angles were used as a boundary condition for the numerical model. The computer generated images matched well with photographs. Assumption of a constant contact angle made the model predictions less accurate. A simple analytical expression was developed to estimate the maximum spread of a droplet on a surface. Bussmann et al. (1999) developed a 3D model of droplet impact onto asymmetric surfaces. Two cases are studied: oblique impact of the droplet onto an inclined surface and onto a sharp edge. Contact angles, measured from photographs, are applied as boundary conditions at the contact line. A simpler model is proposed which requires only the values of the rapidly advancing and receding contact

angles. The simulation results matched well with the photographic data. Sikalo et al. (2005) assumed that the liquid and gas phases share the same velocity field. They noted that numerical simulations which assume a fixed advancing/receding contact angle do not predict the receding phase of the droplet spreading well. The singularity near the contact line was replaced by a local force with some defined dependence on the instantaneous advancing/receding contact line velocity. Gunjal et al. (2005) noted that the agreement between the experimental and numerical results improved when the average contact angle variation with time was implemented instead of using an equilibrium contact angle value. Lunkad et al. (2007) used both dynamic contact angle (DCA) and static contact angle (SCA) models. For horizontal surfaces, they concluded that results from both the models matched well with experiments for less wettable surface whereas for highly wettable surface the DCA model is needed. They also noted that SCA models fail to predict the observed partial or full rebound regimes of droplet impact on inclined surfaces.

As can be seen from the different continuum simulations of droplet spreading, no complete consensus has been reached so far on the dynamic of the problem. This can be owed due to the fact that it is governed by a number of factors and comprises of many different phenomenon occurring at diverse length and time scales. Among the various parameters, the variation of the contact angle and the motion of the contact line are most intriguing and have not been clearly understood. The divergence in the solution caused by the no-slip model near the contact line has lead to researchers proposing different boundary conditions to remove the singularity but their physical origin and validity is not clear. Some researchers have experimentally measured the advancing and receding contact angle, and used these two values in their models to account for the variation in the contact angle. This process is both cumbersome and still an approximation as the dynamic contact angle changes continuously with time. The

microscopic region near the contact line is experimentally inaccessible. It should also be noted that at the actual molecular level, the three phases meet in a small region with finite dimensions and not at a line as assumed in continuum analysis. Thus this microscopic contact angle may be different from the experimentally measured contact angle (Sikalo et al., 2005). All these facts lead to the necessity of molecular modeling in the region near the contact line. With the advent of high-speed computing, molecular dynamics has become an increasingly important tool in gaining a better understanding of fundamental processes by simulation each atom and performing virtual experiments. It becomes possible to vary any governing parameter and to study its dominance on the overall process. Francois and Shyy (2003) acknowledged the need of multiscale modeling that couples the continuum simulation with molecular dynamics in regions surrounding the contact line as a more fundamental approach to understand droplet dynamics.

Maruyama et al. (1998) used molecular dynamics to simulate equilibration of an argon liquid droplet on a platinum wall. The wall was represented by three types of models: three layers of harmonic molecules, one layer of fixed molecules and a simple one-dimensional function. The fluid-fluid and fluid-solid interaction was governed by the Lennard-Jones potential. The contact angle was measured by fitting a circle to the two-dimensional density profile. The contact angle was correlated with the integrated depth of the surface potential. The effect of temperature on the contact angle could not be obtained. The authors also studied the simultaneous evaporation and condensation of droplets, and concluded that their measured contact angles were the same as that at the equilibrium condition.

Kimura and Maruyama (2003) studied the spreading of a water droplet on a platinum surface using molecular dynamics. The water molecules were modeled with the SPC/E potential and the platinum wall was represented by three layers of harmonic molecules modeled as a

constant temperature heat bath. The water-platinum interaction was simulated by two different potential functions. The spreading rate of the water droplet was determined by measuring the area of the water-platinum interface, and was proportional to the one-third power of time at early stage and one-fifth power of time at the later stage.

Ingebrigtsen and Toxvaerd (2007) determined the contact angles of droplets constituting of Lennard-Jones particles on a solid surface using molecular dynamics simulations. The surface, called the “9-3” L-J potential, was modeled by integrating the potential energy between an L-J particles and a semi-infinite continuum of uniformly distributed L-J particles. The domain volume was divided into parallel sheets and the local density variation was obtained using an empirical tanh function in order to determine the equilibrium contact angle. The angles determined matched fairly well with those obtained from Young’s equation for medium and weak fluid-wall interactions, but over predicted them for strong interactions.

Adao et al. (1999) used molecular dynamics simulations to show that the equilibrium contact angle of a sessile drop placed on a heterogeneous substrate follows Cassie’s law. The homogeneity is modeled by having the substrate composed of two species, one which interacts strongly with the liquid and other which interacts weakly. The Lennard-Jones potential is used for all interactions. The contact angle is determined by dividing the droplet into horizontal layers, computing the density of the particles as a function of the distance from the centre and then locating the extremity of the layer as the distance where the density falls below a cutoff value of 0.5 times the liquid density. The authors concluded that the equilibrium contact angle does not change if the sizes of the heterogeneities are of molecular scale, and that the dynamics of such MD drops can be described by the molecular kinetic theory. Gentner et al. (2004) extended this work to include drop impact for cases having low inertia with the droplet molecule consisting of

16-atom chains. The shape of the drop was fitted by a sphere for zero impact velocity, and approximated by a spheroid when the initial speed is not zero. They measured the associated base radii and contact angle versus time and concluded that the spreading velocity is a unique function of the driving capillary force.

Thus, molecular dynamics has been used in the recent years to model drop impact and spreading providing some insight into the moving contact line and the overall process. Droplet spreading coupled with evaporation, oblique drop impacts, droplet condensation are a few problems which need to be captured accurately using molecular dynamics. Extensive effort is still required to understand the physics and fundamentals of the phenomenon.

Wall Models

As molecular dynamics is becoming an increasingly important tool in gaining a better understanding about numerous heat transfer research problems, many problems in this field require modeling the fluid-solid wall boundary condition across which the heat transfer takes place. Numerous models have been proposed and developed in literature.

Abraham (1978), in a pioneering study, used four wall models to study the interfacial fluid density profile of solid/liquid interface systems using Monte Carlo simulations: a) Lennard Jones (L-J) atoms were placed and constrained to remain at the lattice sites of first two planes of an fcc solid termed L-J (100) wall b) discrete centers of interaction in each solid plane were replaced by a continuous distribution of Lennard-Jones atoms with uniform planar density leading to the L-J 10-4 wall model, c) proposed “Boltzmann weighted” wall whose potential is proportional to the probability that a single molecule is at a distance z from the (100) wall irrespective of its x, y coordinates, d) the “Hard wall” whose potential is infinite if an atom penetrates the wall structure, and zero otherwise.

Xu and Li (2007), Thompson and Troian (1997), Priezjev (2007), Voronov et al. (2006) arranged the solid wall atoms in a crystalline structure, and remained fixed during the whole computation process. The fluid atoms were coupled with a thermostat to assign a specific temperature to the fluid. Koplik et al. (1989), to study microscopic aspects of slow viscous flows past a solid wall, set the wall atoms into an initial fcc lattice structure and assigned them a heavy mass $m_H=10^{10}m$ allowing them to move according to the equations of motion. The walls would retain their integrity during the course of the simulation as well as conserve energy in collisions, but eventually disintegrate theoretically.

Xu and Zhou (2004) studied Poiseuille flow in a nanoscale channel using a thermal wall model. The wall atoms are arranged in a fcc structure and remain fixed during the simulation. According to the model, when a liquid particle strikes the wall, all three components of velocities are reset to a biased Maxwellian distribution and the direction of the z-component velocity is set away from the wall; the criteria for liquid atom 'striking' the wall was not mentioned.

Markvoort and Hilbers (2005) looked into the dependence of wetting on solid-gas interface for different density gases. The walls were constructed in a different simulation by randomly placing the wall atoms, governed by L-J potential, in a simulation box and giving them a high temperature. The domain was then cooled down and the system crystallized which was placed in a wider box forming a wall. None of the wall atoms were fixed or restricted. However, it was seen that as the mass of the wall was so large compared to a single gas particles that a single collision hardly affected the wall and the wall atoms keeps their positions.

Drazer et al. (2005) used molecular dynamics simulation to study the behavior of closely fitting spherical and ellipsoidal particles moving through a fluid-filled nanoscale cylinder. The

cylindrical wall was composed of atoms of mass $m_w=100$ tethered to fixed lattice sites by a stiff linear spring. Heat transfer between wall and fluid was not considered in the model.

Spijker et al. (2008) developed a new particle wall boundary condition to replace solid walls. The new condition is based on averaging the contributions of an explicit solid wall and allows for different crystal lattices to be included. Wemhoff and Carey (2005) replaced the solid wall by deriving a wall potential to bind a liquid argon film to the imaginary wall, in order to reduce computational cost. The wall potential depends on the approximated values of Hamaker constant for metal-metal and fluid-fluid interaction. The system pressure was adjusted to an equilibrium value using a flux boundary. The model did not include heating/cooling of fluid by the wall atoms.

Yang (2006) simulated a plane wall where the wall atoms were anchored to their respective lattice sites by a harmonic restoring force. The wall atoms interacted by the L-J potential, and a Gaussian isokinetic thermostat was used to adjust the wall temperature to a constant value at each time step. Ziarani and Mohamad (2008) used a similar method of spring force but used velocity rescaling to achieve constant wall temperature instead of a thermostat. In addition, the first five molecules at the two end of each layer were completely frozen to avoid walls being washed away by fluid molecules.

Maruyama and Kimura (1999), Ohara and Suzuki (2000), Yi et al. (2002), Nagayama and Ceng (2004), Schoen et al. (2005) modeled the solid wall as (111) fcc structure made up of three layers of solid atoms governed by a harmonic potential. Outside the three layers, ‘phantom’ molecules were used to maintain the solid atoms at a specified mean temperature, resembling a Langevin thermostat.

The reason that such various models have been introduced in the past is that no one particular model has been accepted by all researchers; the biggest concern being the actual physics of the any heat transfer model may not be properly depicted. Wall models need to be thoroughly validated to show their physical soundness.

Ultrathin Films, Disjoining Pressure and Hamaker Constant

For ultrathin films, attractive forces exist between the liquid molecules and the molecules of the solid surface. These attractive forces act to pull the liquid into the layer as if the pressure in the layer were reduced by an amount P_d , known as the disjoining pressure. Variation of disjoining pressure with film thickness is shown in figure 1-4. A thin film can exist in equilibrium on a solid surface even when its vapor pressure in the surrounding gas is below the normal saturation pressure for the system temperature (Carey, 1992). Such a non-evaporating film can be seen in the microlayer region at the contact line in nucleate boiling at the base of the bubble as discusses before and shown in figure. The thickness of a non-evaporating film is a function of the surrounding vapor pressure and substrate temperature (Wayner, 1999). The thickness of these non-evaporating thin films is expected to be in the size of nanometers, and thus can be studied using molecular dynamics. Only a handful of researchers have studied nano-thin film evaporation on a solid surface using molecular dynamics simulation.

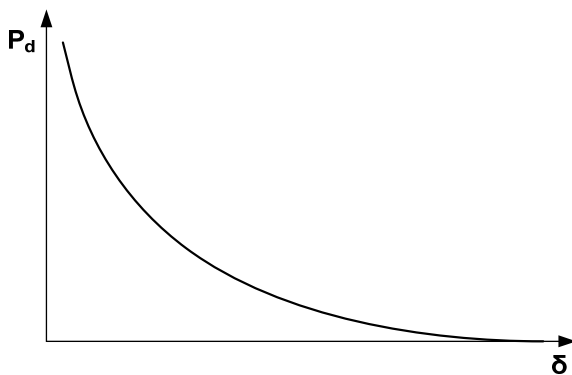


Figure 1-4. Expected variation of film thickness with film thickness

Maruyama and Kimura (1999) applied molecular dynamics simulation to study thin film evaporation and condensation in a nanochannel. An argon vapor region was sandwiched between two argon liquid layers which were in contact with two platinum solid walls. The platinum wall was represented by three layers of harmonic molecules, and the temperature of the wall was controlled by a layer of phantom molecules which are excited by a random force of Gaussian distribution. The aim of the study was to demonstrate that thermal resistance cannot be neglected over a solid-liquid interface when the system size is very small.

Wu and Pan (2006) simulated a thin argon film evaporation on Pt surface, without the temperature effect, in vacuum. They obtained the evaporation/condensation coefficient; noticed the mean temperature for the interface region to be 2-3 K lower than that inside the liquid and the interface thickness to increase with temperature. They concluded that the net evaporation rate of thin liquid film into vacuum in a closed system may be modeled based on Schrage approach.

Yi et al. (2002) studied the evaporation of a thin liquid argon layer on a Pt surface in an argon vapor atmosphere. The Pt surface was modeled as constant temperature using the Langevin thermostat, similar to Maruyama and Kimura (1999). The wall was heated to two temperatures of 150 K and 300 K respectively from an initial equilibrium temperature of 110 K. In the former case a gradual evaporation of the liquid film occurred, while in the latter the Leidenfrost phenomenon was observed. In both the cases, a complete evaporation of the liquid film was obtained. The gradual evaporation is shown in figure 1-5.

Wemhoff and Carey (2005) replaced the solid wall by deriving a wall potential to bind a liquid argon film to the imaginary wall, in order to reduce computational cost. The wall potential depends on the approximated values of Hamaker constant for metal-metal and fluid-fluid interaction. The system pressure was adjusted to an equilibrium value using a flux boundary.

Equilibrium properties were evaluated at different temperatures; film evaporation was not studied.

In the literature available (on molecular dynamics), there has been no mention of any observed non-evaporating thin film in simulations. Van der Waals forces play a central role in all phenomena involving intermolecular forces. Van der Waals force is constituted by three distinct types of forces: induction force, orientation force and dispersion force. The dispersion contribution almost completely dominates the van der Waals energy in the interaction between two dissimilar atoms of which one is non-polar (Israelachvilli, 1994). Dispersion forces act between all atoms and molecules, are always present and contribute to events like adhesion, surface tension, physical adsorption, wetting, liquid and thin films, etc. These forces may be repulsive or attractive, and may also tend to mutually align or orient the atoms between which they are acting. Hamaker constant is introduced to relate the interfacial free energies to the dielectric properties of the materials and to use the surface excess convention for thin films. Hamaker (1937) performed an analysis where he attributed the adhesion between particles to the dispersion forces (also called London forces). The London potential is the interaction between two atoms and by assuming additivity, he obtained the Van der Waals interaction energy between bodies consisting of many molecules by integrating London's pair potential of dispersion interaction. All of the Hamaker's equations can be split into a purely geometrical part and a constant A (widely known as Hamaker constant) which depends on the nature of interaction between the two bodies. The Hamaker constant is a very helpful parameter and can be used to calculate the van der Waals force of interaction, dispersion energy, adhesive pressure, etc. It can also determine the magnitude of spreading of a film on different surfaces (Israelachvilli, 1994). A larger value of the Hamaker constant will result in a wetting film,

whereas a comparatively smaller value leads to a non-wetting film. The Hamaker constant A is defined as (Wayner, 1999):

$$A = \pi^2 C \rho_1 \rho_2 \quad (1.1)$$

where ρ_1 and ρ_2 are the number of atoms per unit volume in the two volumes and C is a coefficient describing the interaction between two atoms. Non-evaporating thin films play an important role in the microlayer region of nucleate boiling and meniscus evaporation, and thus the knowledge of Hamaker constant is essential. For example, numerical simulation of nucleate boiling requires the value of Hamaker constant to determine the non-evaporating film thickness (Dhir, 2001). Not many Hamaker constant values for different fluid-solid combinations are available in literature. Hamaker constant values can be evaluated using Derjaguin and Lifshitz theories, but serve as approximations at best for non-retarded van der Waals forces. A more exact procedure would be to obtain it experimentally using an atomic force microscope (AFM) and then determining its value from measured force-distance curves (Butt, 2005). The Hamaker constants obtained will thus be limited to those particular set of pressure, temperature and materials for which the AFM was used restricting the usage of the values. Thus, additional development in the field of computational molecular dynamics to emphasize interfacial mass transfer is required to have an impact on change-of-phase heat transfer systems (Wayner, 1999).

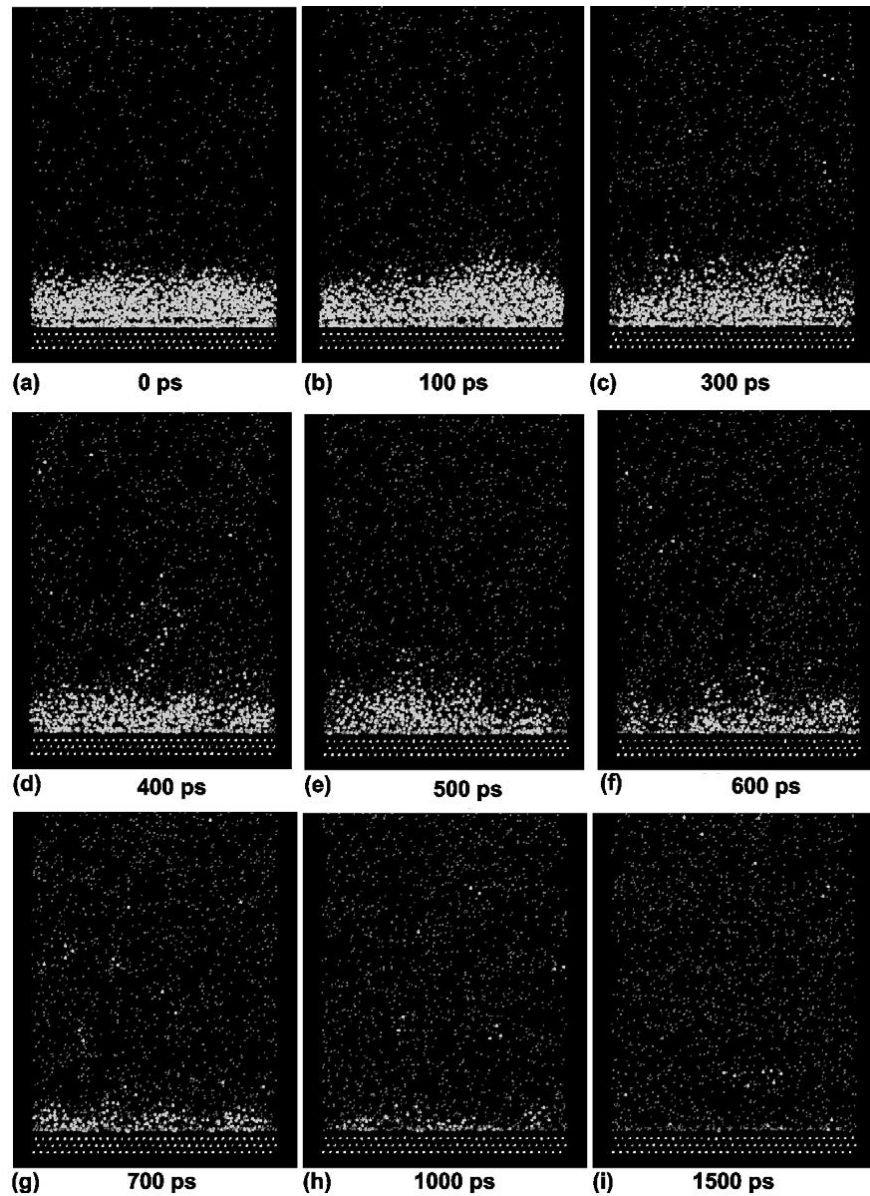


Figure 1-5. Gradual and complete film evaporation simulated by Yi et al. (2002)

Capillary Pressures at Nanoscale

The properties of materials at nanoscale are different from those at macroscale due to the length-scale effects like high surface-to-volume ratios and different dominating physical mechanisms acting at nanoscale. Capillary forces are often present in small mechanical systems and can become very significant at nanoscale. For example, capillary bridges form when water condenses (even under low relative humidity) at the contact spots during the contact of two solid

bodies in air. At nanoscale these capillary bridges can usually be under high negative pressures. The phase diagram of water, shown in Fig. 1-6, shows the stable, metastable and unstable regions (Angell, 1988). In the top right-hand corner water is stable as a liquid. To the left of T_b , the locus of boiling points, water can exist in a metastable state as a superheated liquid in the absence of nucleation centers. To the left of T_h , ordinary density fluctuations are sufficient to cause prompt spontaneous cavitation resulting in homogeneous boiling. Similar arguments hold below T_m , the locus of melting points. T_s is the spinodal of speculated stability limits of water. In the past, the region between T_h and T_s was experimentally accessible as water would cavitate to the left of T_h at macroscale. However, it has been recently possible to have water exist at highly metastable states at nanoscale. When pressure is below the liquid-vapor transition line of water phase diagram, vapor is the most stable state although the transition involves energy barriers. Random fluctuations are large enough to overcome these barriers at macroscale, but at nanoscale the barriers are large compared to the scale of the system and thus metastable state can exist for long intervals of time. An interesting example of metastable state is “stretched” water, i.e., water under tensile stress of negative pressure. Pressure and surface tension affect the formation of bubbles inside a liquid which act towards expanding and collapsing the bubble respectively. Formation of a cavity of volume V requires work equal to PV where P is the pressure of the liquid. Formation of liquid-vapor interface bounding the bubble requires work equal to $\gamma_{LV}A$ where γ_{LV} is the interfacial tension and A is the area of the interface. . The work required to fill the bubble reversibly with vapor of pressure P_v is negative and equal to $-P_vV$. Value of P_v is negligible to P and is neglected (Fisher, 1948). Hence, the net work associated with reversible formation of a spherical vapor bubble of radius r is:

$$\begin{aligned}
 W &= \gamma_{LV}A + PV \\
 &= 4\pi r^2\gamma_{LV} + (4/3)\pi r^3P
 \end{aligned}$$

Thus, for maximum work there is a critical radius of the cavitation R_c defined as:

$$R_c = -\frac{2\gamma_{LV}}{P}$$

If the radius of a bubble is greater than R_c , it can grow unrestricted. No cavitation can occur if the size of the capillary is smaller than R_c . Thus, the liquid can be in a metastable state to the left of T_h line (in Fig. 1-6) and the pressure inside it may be negative.

Briggs (1955) heated water in a thin-walled capillary tube open to atmosphere. The author heated the tubes upto 267°C for about 5 sec before explosion occurred, and concluded that during the time before explosion occurs, the water must be under an internal negative pressure. When the temperature is raised to a point where the forces of cohesion no longer equal or exceed the increasing negative pressure, the system explodes. Thus, water was able to withstand an internal negative pressure of over 51 atm.

Yang et al. (2008) measured the pull-off force between a Si AFM tip and Si samples, as shown in Fig. 1-7, in UHV and in air under different relative humidity values. As there is no water condensation and there no capillary bridges in UHV, subtracting the pull-off force in UHV from that in air results in the capillary force values. Very high negative pressures, down to -160 MPa, were obtained in the capillary bridge. The authors mention that no vapor bubble nucleation occurred in the experiments since the size of the capillary bridges was smaller than the critical cavitation radius.

Tas et al. (2003) created water plugs by filling water in a hydrophilic silicon oxide nanochannel of approximate height of 100 nm. The authors found out that the tensile capillary forces were so strong on this scale that the water plugs were at negative pressure. This negative

pressure induced bending of the thin nanochannel capping layer which results in a visible curvature of the liquid meniscus as shown in Fig. 1-8 The amount of bending of the channel capping was calculated and the negative pressure was found out to be 17 ± 10 bar. The absence of cavitation was explained by the fact that the critical radius for cavitation is comparable to the nanochannel height.

Tyree (2003) discussed the transport system that drives sap ascent from soil to leaves in plants and trees. For very tall trees like redwoods (*Sequoia sempervirens*) which can grow over 100 m high, H. H. Dixon (1986) proposed that a pulling force was generated at the evaporative surface of leaves and that this force was transmitted downwards through water columns under tension to lift water from the roots. This theory, called the cohesion-tension theory, assumes both adhesion of water to the conduit walls and cohesion of water molecules to each other. Plants transport nearly pure water in the xylem conduits at negative fluid pressures of the order of -1 to -10 MPa. Thus, the cohesion-tension theory proposes that water is transported in metastable state. The previous mentioned experimental techniques have experimentally shown the existence of water in metastable state, which can be a major step towards confirming the principles of cohesion-tension theory.

Another important consequence of the water pressure reduction in capillary bridges is the possibility of boiling at temperatures lower than saturation temperatures at corresponding vapor pressure. If the capillary is large enough for cavitation to occur, the pressure inside the capillary bridge will be at a reduced pressure compared with the ambient and the boiling point will be depressed. Figure 1-9 shows the reported observation of boiling in a meniscus between the cantilever and a flat Si sample under laser irradiation that provided a temperature rise of only up to 45°C (Nosonovsky and Bhushan, 2008).

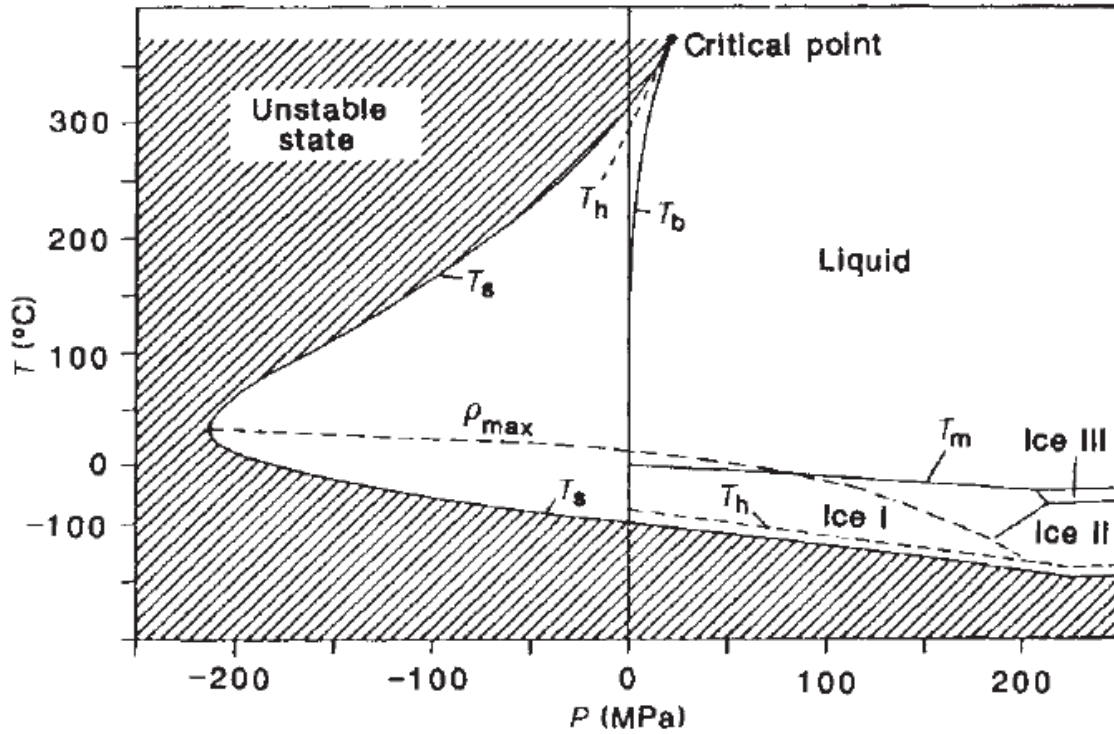


Figure 1-6. Phase diagram of water (Angell, 1988)

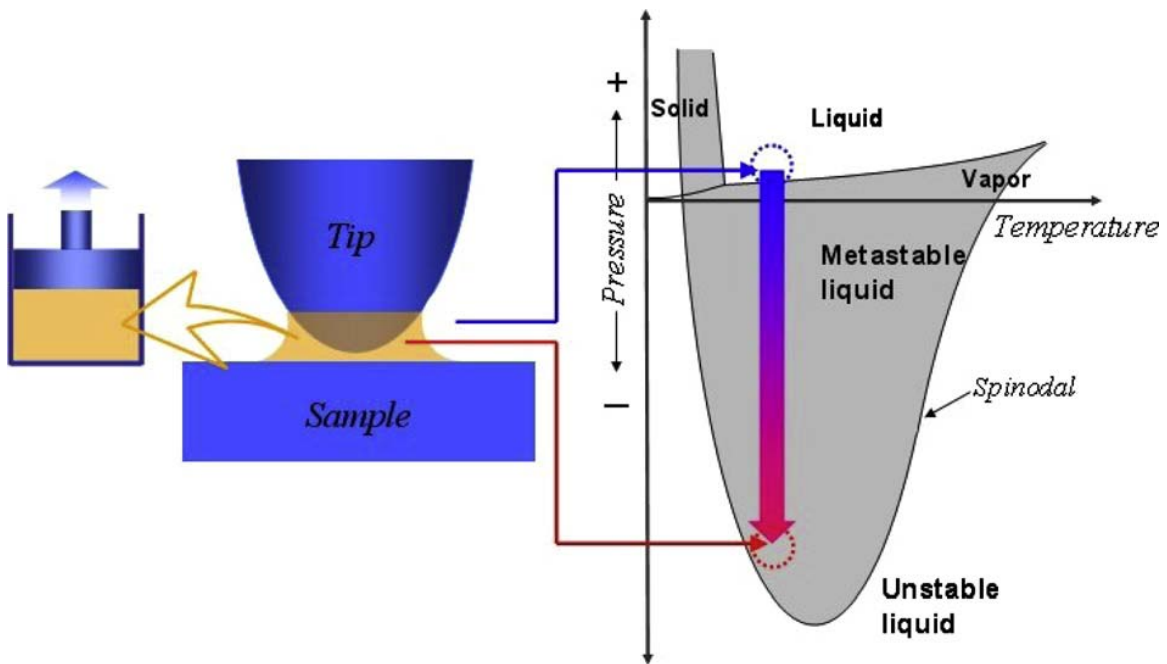


Figure 1-7. Schematic of water phase diagram showing a metastable capillary bridge. The capillary bridge under tension acts like a water tube sealed with a piston, which leads to negative pressure. (Yang et al., 2008)

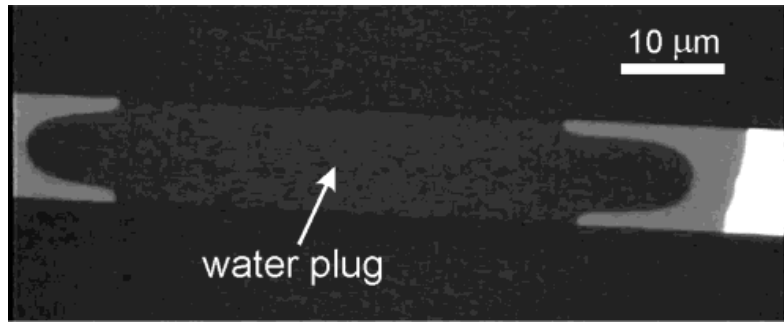


Figure 1-8. Optical micrograph of a water plug in a 100 nm wide nanochannel (Tas et al., 2003)

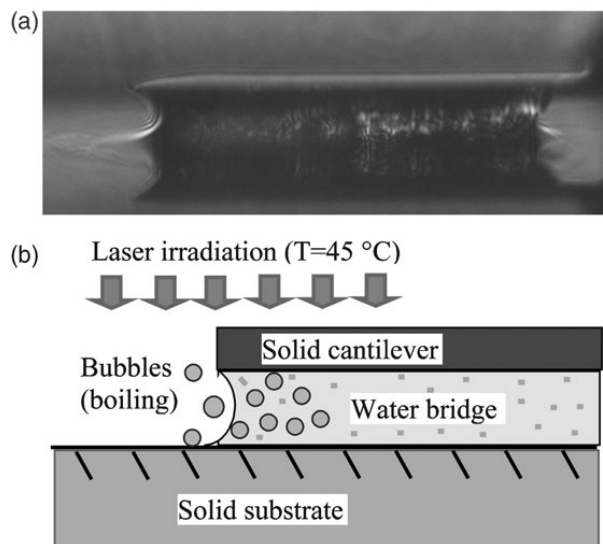


Figure 1-9. (a) Optical image (b) Schematic of water meniscus between a cantilever and a flat surface (Nosonovsky and Bhushan, 2008)

Research Objectives

In spite of the numerous numerical and experimental advances and decades of research in the field of multi-phase physics, the moving contact line problem observed in a) bubble nucleation and growth and b) droplet spreading and impact has still not been fundamentally understood due to the complex subprocesses involved which work at various length and time scales simultaneously. In numerical simulations, the classical no-slip boundary condition leads to singularity at the contact line and the validity of the alternative *ad hoc* models proposed is far

from being established. Exceptionally high-resolution experimental hardware, that is not currently available, is required to study the motion of the contact line at the molecular level. Researchers have agreed on the fact that molecular dynamics simulations of the moving contact line can lead to gaining deeper insight into the fundamentals of the problem.

The most accurate model can be developed if the problem is solved using molecular dynamics for the entire domain of interest. But currently the roadblock to this method of solution is that simulating a bubble on the *millimeter* scale in molecular dynamics would require more than billions of atoms which is not currently possible with the available computing hardware. The contact line region is of the order of a few molecular diameters (*nanoscale*), whereas the bubble grows on the *millimeter* scale. Thus, the best possible solution would be to couple the molecular dynamics with the continuum mechanics. Two feasible approaches, with respect to nucleate boiling, are:

1. The problem is formulated by applying the molecular dynamics simulation to the nanoscale region near the vicinity of the contact line and then coupling that with the continuum mechanics for the remainder of the domain. The coupled system is then solved simultaneously.
2. Simulate the nanoscale vicinity around the moving contact line with molecular dynamics in conditions that mimic nucleate boiling and extract useful information/models to be used at larger length-time scales.

The first approach, also called the hybrid atomistic-continuum model, has been implemented by a few researchers [O'Connell and Thompson (1995), Hadjiconstantinou (1999), Flekkoy et al. (2000), Wagner et al. (2002), Buscalioni and Coveney (2004), Ren and E (2005), Nie et al. (2006), Liu et al. (2007)]. The difficulty with this approach is that it would be still very

computationally demanding to simulate a bubble on the *millimeter* scale and would definitely require simulating billions of atoms on the molecular level. Decoupling the time-scales is also an unresolved issue since time steps in molecular dynamics is of the order of picoseconds, while in continuum mechanics it is in micro to milliseconds. The work done so far by researchers using the hybrid method has been based on nano-length scales only for the entire domain, with the aim of showing the validity of the hybrid approach by comparing the results obtained with fully molecular ones. Thus, solving problems involving coupling *nano* and *micro/millimeter* length and time scales using the first approach has yet to become a success.

The second approach, which is also known as the information passing scheme (Chen and Fish, 2006), is adopted in this proposal. The objective of this approach is to simulate the local nanoscale vicinity around the moving contact line by molecular dynamics, then study and analyze the molecular dynamics results to extract useful information/models which can be used in larger length-time scale simulations. Thus, the basic idea here is to extract useful information from molecular dynamics simulation to obtain a deeper understanding of the physics occurring which cannot be captured in experiments due to the length scale involved.

The non-evaporating thin film is the main focus in this work. Its thickness is expected to be in the size of nanometers, and thus is studied here using molecular dynamics simulations. The specific goals of this proposal are to:

- 1) simulate thin film evaporation using molecular dynamics, study the physics obtained and evaluate useful properties using statistical mechanics
- 2) simulate droplet impingement and spreading on surfaces of varying wettability and evaluate moving contact angle variation with time

- 3) use molecular dynamics to model an evaporating meniscus in order to gain a fundamental understanding of the physics occurring at the three-phase interline region coupled with the non-evaporating region

Chapter 2 outlines the molecular dynamics theory and the algorithms used along with statistical sampling approach. A novel thermal wall model is introduced and validated to simulate heat transfer between wall and fluid. Chapter 3 shows the results obtained from simulation of thin film evaporation and the occurrence of non-evaporating thin film. A method to calculate the Hamaker constant from molecular dynamics simulations is outlined, which has not been attempted in literature before. The transient film evaporation is extended to seven cases in order to study the effect of nanochannel height, initial film thickness and wall temperature on the formation of non-evaporating film. Chapter 4 studies the impact of a nano-droplet on a wall with varying surface wettability. Variation of contact angle with time is evaluated. The wall temperature is also changed to observe the Leidenfrost phenomenon. Chapter 5 simulates the evaporation of a meniscus at nanoscale. Two cases, with partial and complete wall heating, are studied. Heat and mass transfer characteristics and pressure variation in the non-evaporating and interline regions are studied. A curve-fitted meniscus boundary condition is also developed. The dissertation ends with conclusions and future work in Chapter 6.

CHAPTER 2 THEORY AND APPROACH

Molecular Dynamics Simulation

The most rudimentary model for a substance capable of existing in any of the three states of matter – solid, liquid and gas – is based on atoms interacting with one another, without considering their quantum origins. The interactions are responsible for providing the two principal features of an interatomic force: a) resistance to compression (repulsion at close range), and b) binding atoms together in liquid and solid states (attraction over a range of separation). Potential functions exhibiting these characteristics can have many forms, and when chosen properly, provides accurate models for real substances. Usually this function comes from experimental data or quantum mechanics calculations. The interaction force between the atoms can be derived from the potential function U by the following relation: $\vec{F} = -\nabla U$. Summing up all the forces acting on one atom by all other atoms yields the total force acting on that atom. The best known potential function is the Lennard-Jones (LJ) potential. This function was originally proposed for liquid argon. For a pair of atoms i and j located at \vec{r}_i and \vec{r}_j , the potential energy as defined by the LJ potential is:

$$U_{LJ}(r_{ij}) = \begin{cases} 4\varepsilon \left[\left(\frac{\sigma}{r_{ij}} \right)^{12} - \left(\frac{\sigma}{r_{ij}} \right)^6 \right] & r_{ij} < r_{cut} \\ 0 & r_{ij} \geq r_{cut} \end{cases} \quad (2.1)$$

where $r_{ij} = |\vec{r}_i - \vec{r}_j|$. The parameter ε governs the strength of the interaction, and σ defines a length scale. The interaction repels at close range, then attracts, and is eventually cut off at some separation r_{cut} (known as the cut-off radius) to reduce computational cost while serving as a reasonable approximation and still providing good accuracy to the simulations. The LJ potential

is the most widely used potential for molecular simulations, and provides accurate representation for the properties of argon (Sadus, 1999). In order to smoothly truncate the LJ potential and remove the discontinuity at the cut-off distance, a few modifications have been suggested in literature. The modified LJ model proposed by Stoddard and Ford (1973) has been used in this work for both argon-argon and argon-platinum interactions:

$$U_{MLJ}(r) = 4\varepsilon \left[\left\{ \left(\frac{\sigma}{r} \right)^{12} - \left(\frac{\sigma}{r} \right)^6 \right\} + \left\{ 6 \left(\frac{\sigma}{r_{cut}} \right)^{12} - 3 \left(\frac{\sigma}{r_{cut}} \right)^6 \right\} \left(\frac{r}{r_{cut}} \right)^2 - \left\{ 7 \left(\frac{\sigma}{r_{cut}} \right)^{12} - 4 \left(\frac{\sigma}{r_{cut}} \right)^6 \right\} \right] \quad (2.2)$$

The above potential form is employed for both argon-argon and argon-platinum atom interaction with the following values [6]: $\sigma_{Ar-Ar} = 3.4 \times 10^{-10} \text{ m}$, $\varepsilon_{Ar-Ar} = 1.67 \times 10^{-21} \text{ J}$,

$\sigma_{Ar-Pt} = 3.085 \times 10^{-10} \text{ m}$, $\varepsilon_{Ar-Pt} = 0.894 \times 10^{-21} \text{ J}$. The mass of an argon atom is $6.69 \times 10^{-26} \text{ kg}$,

$\varepsilon/k_B = 120.95 \text{ K}$ and time step is 5 fs. The ε and σ parameters in Lennard-Jones (LJ) potential are obtained by analysis of the experimental data for second virial coefficients, transport coefficients, constants of the critical, melting or boiling points, or other properties (Hirschfelder et al. 1964). The author presents the equations (in the sections as mentioned above), which when fitted with the experimental data, give the LJ parameters. The experimental values of viscosity of argon are listed by Johnston and Grilly (1948), and isotherm data (for virial coefficient evaluation) is listed by Michels et al. (1949). Recently, other methods have been introduced to obtain the parameters, like using ab-initio quantum mechanical and molecular mechanical potentials (Martin et al. 2002).

Force Calculation Algorithm

In a typical molecular dynamics simulation, as much as 95% of the computing time is spend in examining the complete set of $N(N-1)/2$ pairs, identifying those pairs separated by less than the cutoff distance and computing the forces for this subset (Allen and Tildesley, 1989).

Hence, the algorithm used for force evaluation becomes very important. For simulations regarding liquid-vapor phase change (where density continuously keeps changing), the two most widely used algorithms are:

Brute Force Method

In this method, to compute the total force on an atom i , the force acting on i due to all other atoms 1 to N has to be calculated. Thus, all pairs of atoms are examined. This is simplest to implement, but very inefficient when the interaction cut-off radius is small compared to the linear size of the domain. The amount of computation needed grows as order of N^2 (or $N(N-1)/2$ by taking advantage of Newton's third law).

Linked List Method

This algorithm is a cell-based method and involves data organization, and is particularly efficient for simulations involving a large number of molecules ($N \geq 1000$) (Allen and Tildesley, 1989). The computational domain is divided into cells with each side of the cell being greater than or equal to r_{cut} . At any time step, the atoms are binned into their appropriate cells. Two arrays, head-of-chain array (HEAD) and linked-list array (LIST), are created during the binning process. The HEAD array contains the identification number of one of the atoms binned into that cell, and this number acts as a pointer to the LIST array which contains the number of all the atoms in that cell in a sequential order. Thus, this method reduces the task of finding neighbors of a given atom to checking in 27 cells – the cell the atom is in and 26 neighboring cells. Particular care has to be taken in this method when dealing with vapor or liquid regions, as some of the cells might not contain any atom. For a three dimensional system, there are on average $N_c = N/M^2$ atoms in each cell. The computing power is of the order of $27NN_c$ (or $13.5 NN_c$). This algorithm results in faster computation speeds and is implemented in this work.

Integrator Method

The equation of motion needs to be integrated in order to obtain the positions and velocities of the atoms at every time step. Thus, after calculating the force acting on each atom i from the potential function, Newton's second law is used to determine the acceleration:

$$\vec{F}_i = m_i \vec{a}_i \Rightarrow \frac{d^2 \vec{r}_i}{dt^2} = \frac{\vec{F}_i}{m_i} \quad (2.3)$$

where \vec{F} is the force acting on atom i , and m and \vec{a} are its mass and acceleration respectively.

Using the acceleration, the position and velocities are obtained via the integrator method for time $t + \Delta t$. The integrator method used in this work is the Velocity-Verlet method:

$$r(t + \Delta t) = r(t) + \Delta t v(t) + \frac{\Delta t^2 a(t)}{2} \quad (2.4a)$$

$$v(t + \Delta t/2) = v(t) + \frac{\Delta t a(t)}{2} \quad (2.4b)$$

$$v(t + \Delta t) = v(t + \Delta t/2) + \frac{\Delta t a(t + \Delta t)}{2} \quad (2.4c)$$

The advantage of this method is that the calculation of velocities is in phase with that of the positions. Also, this method calculates the velocities more accurately than the other common Verlet and leap-frog methods (Sadus, 1999). Thus, after the new positions and velocities are obtained at time $t + \Delta t$, the whole process is repeated again i.e. force computation from linked cell algorithm, using Newton's second law and then integrator method to advance the system in time.

Non-Dimensional Units

The use of dimensionless parameters in molecular dynamics is very helpful due to several reasons (Rapaport, 2004). The values of various parameters are extremely small as they are associated to the atomic scale. Implementation of dimensionless parameters makes it possible to

work with values which are not far from unity. Also, these units remove any risk of facing computer hardware related problem of not being able to represent such small values.

Dimensionless units simplify the equations of motion as the parameters defining the model are reduced. Also, it helps in scaling of certain computed properties and a single model can be used to describe a whole class of problems. The dimensionless parameters, denoted with an asterisk (*), used here are defined in Table 2-1.

Table 2-1. Dimensionless Parameters

Parameter	Dimensionless form
Energy	$U^* = \frac{U}{\varepsilon_{Ar}}$
Mass	$m^* = \frac{m}{m_{ref}}$
Distance	$r^* = \frac{r}{\sigma_{Ar}}$
Velocity	$v^* = v \left(\frac{m_{ref}}{\varepsilon_{Ar}} \right)^{1/2}$
Time	$t^* = \frac{t}{\sigma_{Ar}} \sqrt{\frac{\varepsilon_{Ar}}{m_{ref}}}$
Temperature	$T^* = \frac{k_B T}{\varepsilon_{Ar}}; \quad T^* = \frac{1}{N(\text{dim})} \sum \vec{v}_i \cdot \vec{v}_i$
Density	$\rho^* = \rho \sigma^3$
Pressure	$P^* = \frac{P \sigma^3}{\varepsilon}$

The force acting on an atom i due to interactions for argon-argon and argon-platinum can be deduced (from derivation of potential function) to the following equations:

Argon – Argon interaction

$$\ddot{r}_i^* = 48 \sum_{j(\neq i)} \left(r_{ij}^{*-14} - 0.5 r_{ij}^{*-8} - r_{cut}^{*-14} + 0.5 r_{cut}^{*-8} \right) \vec{r}_{ij}^* \quad (2.5)$$

Argon – Platinum interaction

$$\ddot{r}_i^* = 48 \left(\frac{\mathcal{E}_{Ar-Pt}}{\mathcal{E}_{Ar}} \right) \sum_{j(\neq i)} \left(\left[\frac{\sigma_{Ar-Pt}}{\sigma_{Ar}} \right]^{12} r_{ij}^{*-14} - 0.5 \left[\frac{\sigma_{Ar-Pt}}{\sigma_{Ar}} \right]^6 r_{ij}^{*-8} - \left[\frac{\sigma_{Ar-Pt}}{\sigma_{Ar}} \right]^{12} r_{cut}^{*-14} + 0.5 \left[\frac{\sigma_{Ar-Pt}}{\sigma_{Ar}} \right]^6 r_{cut}^{*-8} \right) \vec{r}_{ij}^* \quad (2.6)$$

Boundary Conditions

In the present work, the computational domains are in the form of a cuboid. This imposes a total of six boundaries, two each in the x, y and z directions. Thus, the same number of boundary conditions is required. Three boundary conditions are used in this work depending on the problem simulated.

Periodic Boundary Condition (PBC)

A system that is bounded but free of physical walls can be constructed by using this boundary condition. This is equivalent to considering an infinite, space-filling array of identical copies of the simulation region. An atom that leaves the simulation region through a particular boundary face immediately reenters the region through the opposite face. Also, atoms lying within the cutoff distance of a boundary interact with atoms near the opposite boundary. Thus, periodic boundaries have to be in multiples of two.

Mirror Boundary Condition

This boundary condition simulates an imaginary adiabatic wall. The collision of atom with this wall is perfectly elastic; momentum and energy are conserved. If an atom, which is close to the wall at time t , crosses this boundary at atom $t + \Delta t$, it will be placed inside the boundary as if it has been reflected by a mirror. The atom will be assigned the same position as it was at time t with the velocity directed away from the wall.

Thermal Wall Boundary Condition

A novel ‘fluid-wall thermal equilibrium model’ to numerically simulate heat transfer between wall and fluid atoms in molecular dynamics is introduced in this work. The details of this proposed model, and its validation is discussed in later section.

Initial Structure

The domain in the simulations consists of argon fluid and platinum wall(s). Platinum atoms, arranged in fcc (111) structure as shown in figure 2-1, constitute the platinum wall with the interatomic distance as defined in literature (Yi et al., 2002). As will be discussed later, the platinum atoms remain stationary throughout the simulation. For argon fluid, the distance between the argon atoms is calculated as follows: knowing the volume occupied by liquid (or vapor) argon, the saturation density at the equilibration temperature (from argon thermodynamic tables) is used to obtain the total mass of liquid (or vapor) argon, which divided by the mass of an argon atom gives the total number of liquid (or vapor) argon atoms. The distance between the atoms is then obtained assuming they are arranged in a simple cubic structure. The argon atoms are arranged by this interatomic distance thus defining the initial structure of the domain. The argon atoms are assigned initial random velocities, such that the average temperature of the domain is the desired temperature. No initial acceleration is given to the argon atoms. The results of a simulation of ample duration are not sensitive to the initial state.

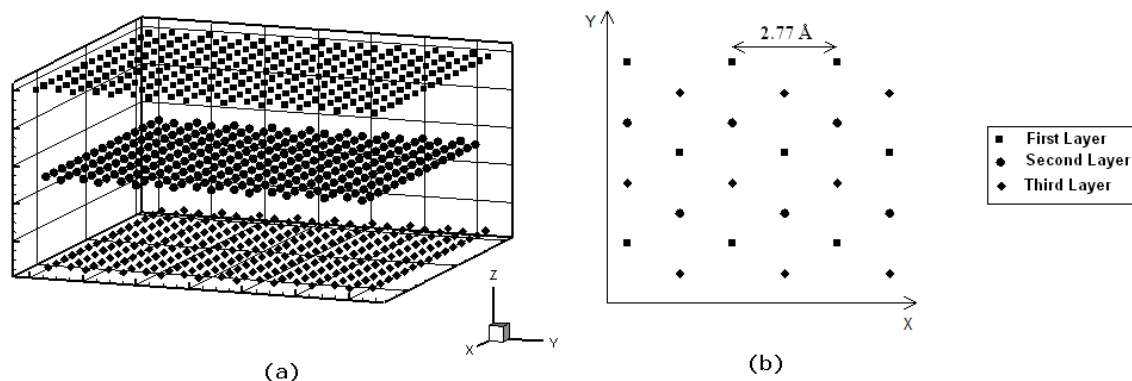


Figure 2-1. Arrangement of Pt wall atoms in fcc(111) structure; (a) 3-D view of the first three layers, (b) X-Y projection (top view) of the wall atoms

Simulation Stages

All the simulations in this work are given an initial temperature. A simulation procedure is implemented to make the argon fluid reach equilibrium at the desired temperature from the initial structure outlined in the previous section. The simulation process is divided into two stages to achieve the above. In the first stage, a velocity-scaling period is used where the velocity of each argon atom is scaled at every time step to maintain the system at a constant temperature (Sadus, 1999). The velocity of each component of an atom i is scaled from its actual velocity to a new velocity in the following way:

$$v_{ix}^{new} = v_{ix} \sqrt{\frac{T_d}{T_a}}; \quad v_{iy}^{new} = v_{iy} \sqrt{\frac{T_d}{T_a}}; \quad v_{iz}^{new} = v_{iz} \sqrt{\frac{T_d}{T_a}} \quad (2.7)$$

where T_d and T_a are the desired and actual system temperatures respectively. This is followed by a second stage, called the equilibration period, where the velocity scaling is turned off and the atoms are allowed to move naturally. This is done to remove the artificial motion which the atoms were subjected to in the first stage. The system temperature fluctuates about the desired temperature in this period. A third stage can follow in the simulation procedure if an external

wall is present in the computational domain. In this stage, named the heating period, heat transfer from the wall occurs and the actual physics of the problem is observed and studied.

Statistical Sampling

Statistical mechanics provides the link between thermodynamics and random atomic behavior. Thermodynamic properties such as pressure, temperature, energy, etc can be calculated by averaging the atoms positions, velocities, interatomic potential and forces. In this work, several properties have been evaluated by using statistical mechanics equations.

Density

With phase change being the main focus in this work, calculation of density becomes quite important. The domain is divided into equal slices in z-direction. The number of atoms in each slice is counted to compute the density. Hence, if the slice thickness is Δz and N_i is the number of atoms in slice i , then the instantaneous density of that slice can be found out as:

$$\rho(z_i) = \frac{m N_i}{l_x l_y \Delta z} \quad (2.8)$$

where l_x and l_y are the x and y dimensions of the domain respectively, and m is the mass of the atom. The average density can be computed by time-averaging the instantaneous density as follows: $\rho_i = \langle \rho(z_i) \rangle$. The average density can be plotted along the height (z-direction) of the domain to see the density gradient at different times. Number density calculates the average number of atoms in a slice, and can be found out using the same equation as above but without the m term.

Energy

The total energy E of the domain can be obtained by adding up the kinetic E_{kin} and potential E_{pot} energies. The kinetic energy can be computed from the individual momenta of the atoms, while the potential energy is the sum of interatomic interactions.

$$E_{kin} = \sum_{i=1}^N \frac{1}{2} m v_i^2 \quad (2.9)$$

$$E_{pot} = 4\epsilon \left[\left\{ \left(\frac{\sigma}{r} \right)^{12} - \left(\frac{\sigma}{r} \right)^6 \right\} + \left\{ 6 \left(\frac{\sigma}{r_{cut}} \right)^{12} - 3 \left(\frac{\sigma}{r_{cut}} \right)^6 \right\} \left(\frac{r}{r_{cut}} \right)^2 - \left\{ 7 \left(\frac{\sigma}{r_{cut}} \right)^{12} - 4 \left(\frac{\sigma}{r_{cut}} \right)^6 \right\} \right] \quad (2.10)$$

$$E = E_{kin} + E_{pot} \quad (2.11)$$

Temperature

The equipartition principle is used to calculate the temperature. For N atoms, each with three degrees of freedom, the instantaneous temperature of the domain is:

$$T = \frac{2E_{kin}}{3Nk_B} = \frac{1}{3Nk_B} \sum_i m v_i^2 \quad (2.12)$$

Temperature gradient along the height of the domain can be computed by dividing the height into equal slices, and computing the average temperature of each slice, similar to the calculation of density as mentioned before.

Heat Flux

The microscopic heat flux Q for a one-component system of N particles interacting via pair potentials in a control volume V can be written as follows (de Andrade and Stassen, 2004):

$$Q = \frac{1}{V} [Q_k + Q_p + Q_w] \quad (2.13)$$

where,

$$Q_k = \frac{1}{2} \sum_{i=1}^N m v_i^2 \vec{v}_i \text{ is the kinetic energy transported by mass flow}$$

$$Q_p = \frac{1}{2} \sum_{i=1}^N \sum_{j \neq i}^N U(r_{ij}) \vec{v}_i \text{ is the flux of potential energy due to mass flow}$$

$Q_w = -\frac{1}{2} \sum_{i=1}^N \sum_{j \neq i}^N r_{ij} \frac{dU(r_{ij})}{dr_{ij}} \hat{r}_{ij} \bar{v}_i \cdot \hat{r}_{ij}$ is directed along the intermolecular separation by the force

displacing the pair of particles i and j by r_{ij} , and accounts for the coupling of this work term to the mass flow

Thermal Conductivity

From the definition of temperature, the temperature gradient dT/dz can be computed when the system reaches equilibrium. The heat flux can be computed as described above. Thus, the thermal conductivity can be calculated as follows:

$$k_{simul} = -Q/(dT/dz) \quad (2.14)$$

Pressure

Weng et al. (2000) suggested an improved method to estimate local pressure distributions by combining the work by Nijmeijer et al. (1988) and Daiguji and Hihara (1999) with Kirkwood and Buff's theory (Rowlinson and Widom, 1982). This method takes into account that an intermolecular force contributes to local pressure in each plane between the two molecules. The domain is divided into equal slices in the desired direction. The local normal pressure component p_N and tangential pressure component p_T are expressed as:

$$p_N(\text{slab } k) = \langle n(k) \rangle k_B T - \frac{1}{V_{slab}} \left\langle \sum_{i,j}^k \left(\frac{z_{ij}^2}{r_{ij}} U'(r_{ij}) f_{k,ij} \right) \right\rangle \quad (2.15)$$

$$p_T(\text{slab } k) = \langle n(k) \rangle k_B T - \frac{1}{V_{slab}} \left\langle \sum_{i,j}^k \left(\frac{\frac{1}{2}(x_{ij}^2 + y_{ij}^2)}{r_{ij}} U'(r_{ij}) f_{k,ij} \right) \right\rangle \quad (2.16)$$

where $n(k)$ is the number density in slab k , V_{sl} is the volume of slab k and $f_{k,ij}$ is $L_{k,ij}/|z_{ij}|$. The

first terms in both the equations are the contribution from kinetic motion of molecules while the

second terms are the contribution from the interatomic force. The length $L_{k,ij}$ is defined as the size of the interval in which the intermolecular force between molecules i and j is effective in the slab k . For example, consider the force between atoms i and j as shown in figure 2-2. If neither atom is in a slab, such as slab 3, $L_{3,ij} = L_{\text{slab}}$; if one atom is in a slab, such as slab 1, $L_{1,ij} = L_1$. If both atoms are in the same slab, such as atoms p and q , $L_{7,ij} = |z_{ij}|$. Surface tension, defined as the difference between the local normal and tangential pressure components, can be expressed as:

$$\gamma = \frac{1}{2} \int_0^{L_z} (p_N - p_T) dz \quad (2.17)$$

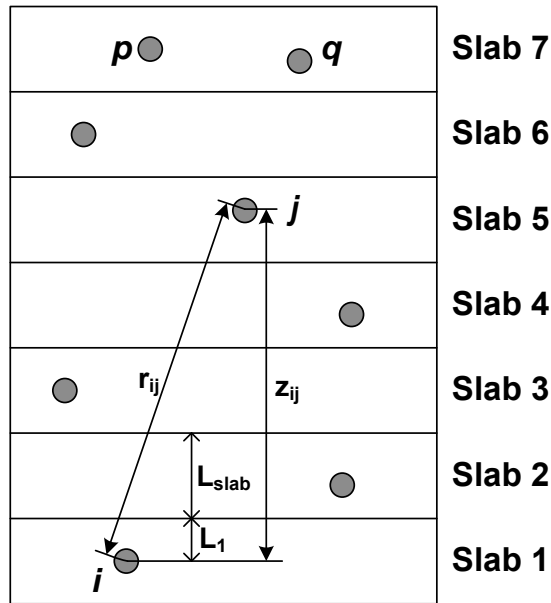


Figure 2-2. Sketch for pressure contribution of atoms i, j

Pressure Verification

The method described in above section is used to evaluate pressure distributions. For verification, pressure and surface tension are calculated in a computational domain consisting of a liquid layer surrounded by vapor, as shown in figure 2-3, for six different temperature cases. The domain parameters for all the cases are listed in table 2-2. Periodic boundary condition is

applied to all six boundaries. The domain is divided into slabs of thickness 0.34 nm in the z-direction. The timestep is taken as 5 fs. Velocity scaling is done for the initial 500 ps and then the system is allowed to equilibrate for an additional 1000 ps. The Statistical values are averaged over the final 100,000 timesteps. Temperature-density, pressure-density and surface tension-pressure plots are shown in figures 2-4, 2-5 and 2-6 respectively, in which the results from simulation are compared to experimental values from thermodynamic tables for argon (NIST webbook). It can be seen that the values match very well.

Table 2-2. Simulation parameters for pressure verification

Temperature (K)	l_x (nm)	l_y (nm)	l_z (nm)	Liquid layer thickness (nm)	Number of argon atoms
90	6.20	6.20	14.63	6.20	4949
100	6.20	6.20	14.63	6.20	4949
110	6.20	6.20	14.63	6.20	4949
120	6.20	6.20	14.63	6.20	4949
130	4.79	4.79	13.33	4.79	2213
140	6.20	6.20	12.51	4.08	3215

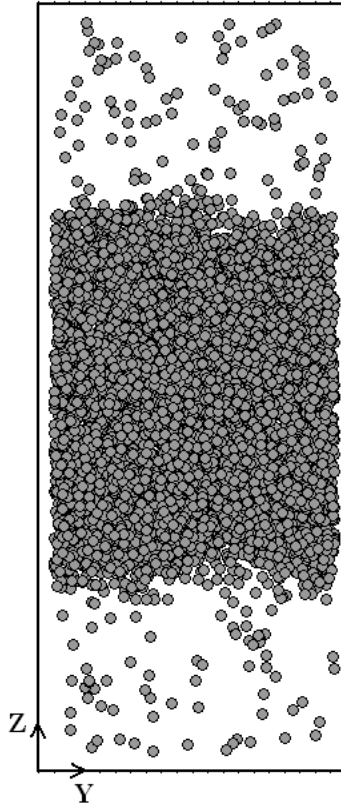


Figure 2-3. Simulation domain at an intermediate timestep for pressure verification

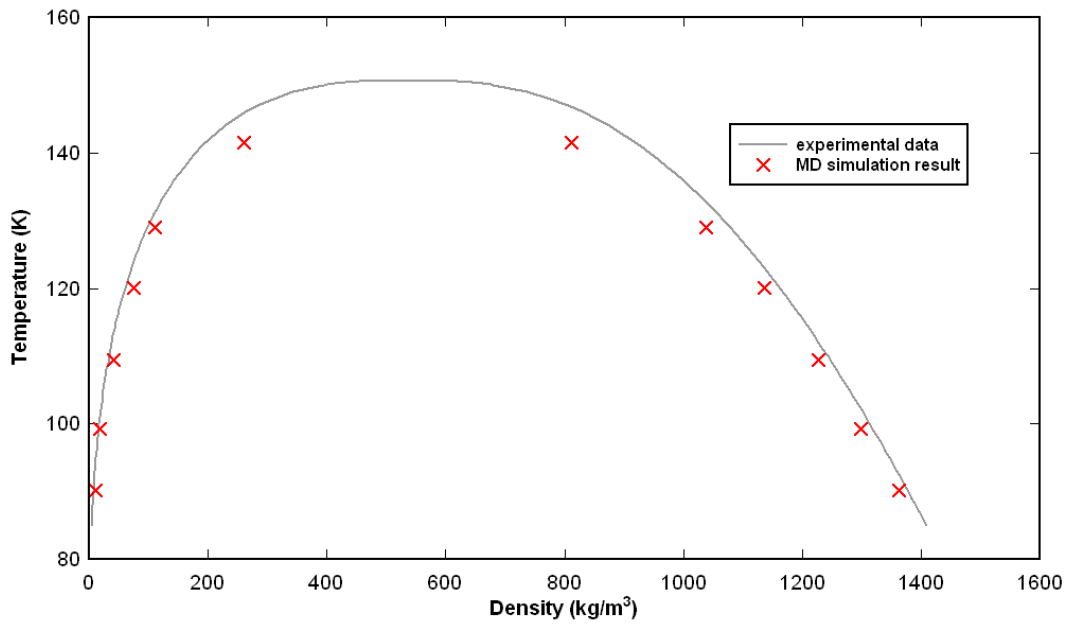


Figure 2-4. Temperature-density plot for liquid slab surrounded by vapor atoms

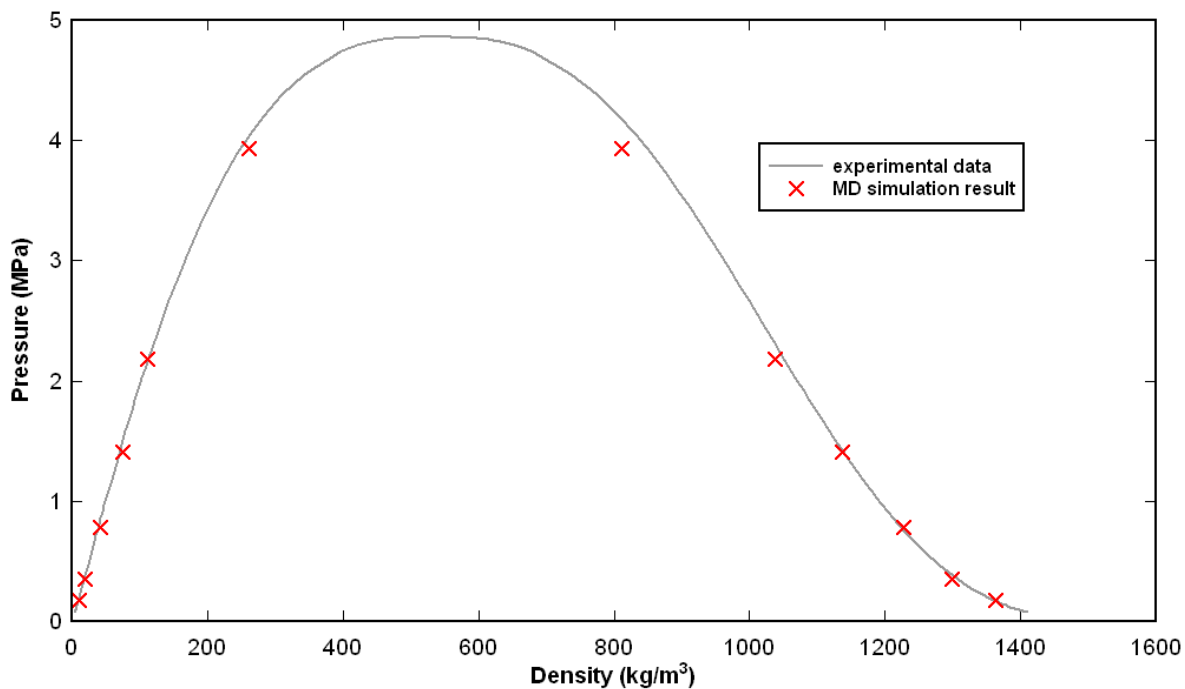


Figure 2-5. Pressure-density plot for liquid slab surrounded by vapor atoms

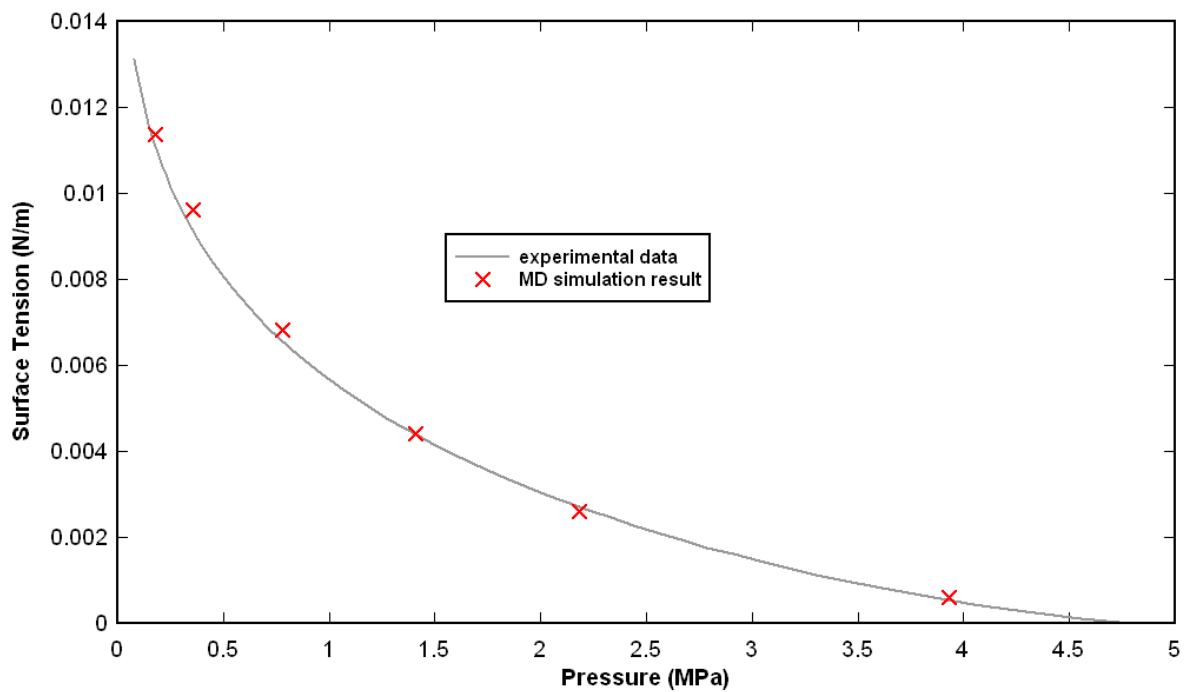


Figure 2-6. Surface tension-pressure plot for liquid slab surrounded by vapor atoms

Distinguishing Between Liquid Atoms and Vapor Atoms for Argon

An important part of the simulation is to define a criterion to label a fluid atom as “liquid” or “vapor”. The argon atoms in the liquid phase are differentiated from the argon atoms in the vapor phase based on the minimum number of neighboring atoms within a certain radius. Thus in order to obtain this threshold number density and threshold radius for a saturation temperature of 90 K, a computational domain of size 4.72 nm×4.72 nm×4.42 nm is constructed with periodic boundary conditions in x, y and z directions. The domain consists of 2028 argon atoms in saturated liquid state at 90 K. Velocity-scaling is done for 0-100 ps and then the system is allowed to equilibrate for an additional 1000 ps. The minimum threshold number of all the atoms is determined within a radius (ranging from 0.41 nm to 0.59 nm at steps of 0.01 nm at every 0.25 ps (i.e. total of 4000 times) during the equilibration period. The average of these values is plotted against the radius in figure 2-7. The plot also shows the number of times (in %) when the minimum threshold number at a certain time step falls below the average. Threshold radius of 0.53 nm is chosen as the criterion and the average threshold number is rounded off to the lower integer. Thus, if an argon atom has 7 or more neighboring atoms within a radius of 0.53 nm it is said to be a “liquid” atom or else a “vapor” atom.

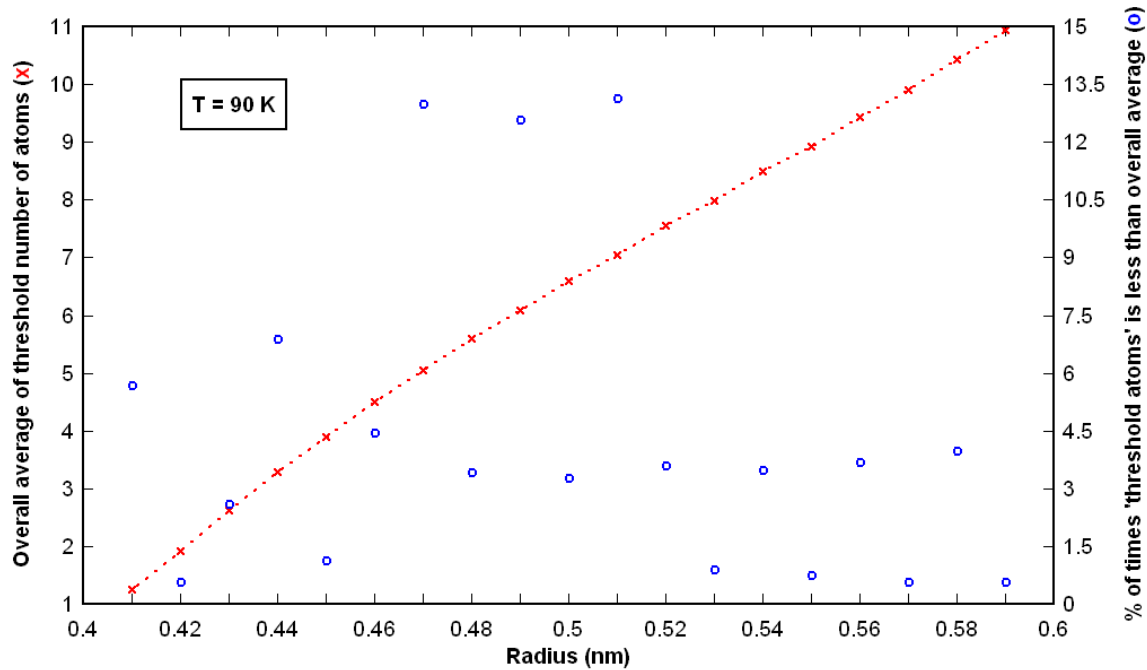


Figure 2-7. Plot to obtain the threshold number density and threshold radius for saturated liquid argon at 90 K

Fluid-Wall Thermal Equilibrium Model

The heat transfer from the heated wall to the fluid is simulated with the following wall-fluid interaction mechanism. The heated wall-fluid thermal energy transfer interaction is constituted of two parts: 1) interaction potential model, and 2) proposed ‘fluid-wall thermal equilibrium model’ (to numerically simulate heat transfer between wall and fluid atoms). The interaction potential model, using the LJ potential, is a standard method as it has been used by many researchers for argon-platinum interaction in molecular dynamics approach. The fluid-wall thermal equilibrium model is presented in details below.

Figure 2-8 shows the schematic of the fluid-heated wall thermal equilibrium model. The Pt atoms constituting the heated wall are assumed to be fixed in space, and do not move at any time during the simulation as for a solid, their range of movement is relatively much restricted than those of the fluid atoms. In addition, it is also aided by the fact that the mass of a Pt atom is

roughly five times that of an argon atom. The fluid-wall thermal energy exchange is simulated as follows: the Pt wall is at a specified constant temperature, and an argon atom reaches this temperature (i.e. the atom is assigned a corresponding velocity by instantaneous velocity re-scaling; direction of the atom is not changed) by “coming in thermal equilibrium with” the *temperature of the wall*. The force due to the wall atoms on the fluid atoms is either attractive or repulsive depending on the distance between the two due to the nature of the Lennard-Jones potential. A distance r_{cr} , less than r_{cut} , is defined as the neutral position of wall influence. Accordingly, any fluid atom on the $z = r_{cr}$, as shown in figure 2-8, would experience a zero force from the first layer wall atom that is located at the shortest distance from this fluid atom. It is noted that this fluid atom would experience only attractive forces from other wall atoms as the distance between this fluid atom and other wall atoms are all larger than that shortest distance. Therefore any fluid atom will have to get below $z = r_{cr}$ (i.e. in region 3) to have any chance of experiencing a repulsive force from the wall atoms. Based on the above scenarios, the fluid atoms can be divided into three groups based on their locations in the respective regions near the wall as shown in figure 2-8.

Region 1. $z > r_{cut}$: The fluid atoms which are above the cutoff radius do not experience any force from the wall atoms.

Region 2. $z < r_{cut}$ & $z > r_{cr}$: In this region, the fluid atoms only experience an attractive force by the wall atoms due to the nature of the L-J potential.

Region 3. $z < r_{cr}$: In this region, the fluid atoms can experience either an attractive force or a repulsive force due to the wall atoms.

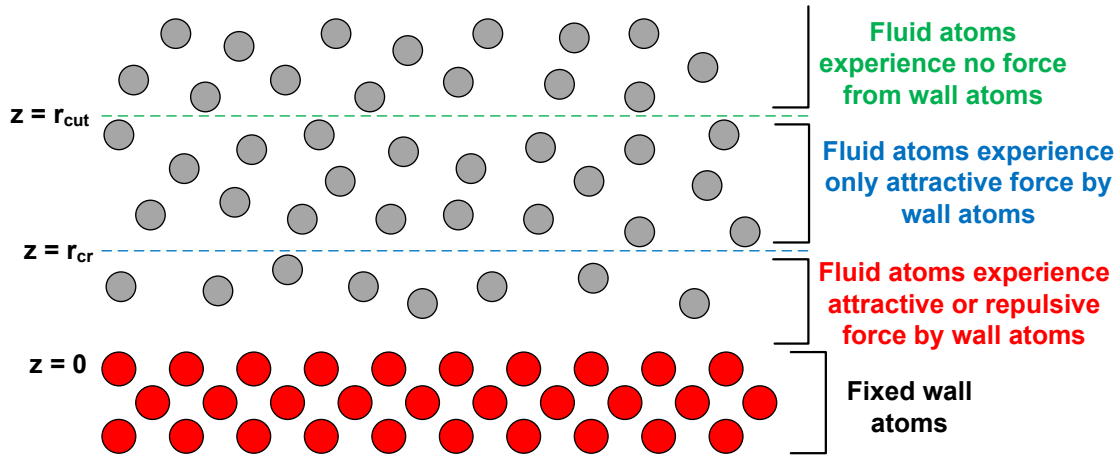


Figure 2-8. Fluid-wall thermal equilibrium model

The physical mechanism of a fluid receiving heat from a solid wall is composed of a two-stage force interaction that results in an energy transfer from the hot wall to the fluid atoms. During the first stage, the fluid atom is accelerated towards the wall atoms by the attractive force. The fluid atom would then reach a zero force point before being bounced back by a repulsive force. If the fluid atom is heated up, the rebounded fluid atom would possess more kinetic energy than its original kinetic energy before the interaction. Therefore, a fluid atom is considered to be heated up to the wall temperature only when: (a) the atom is in region 3 as it can only experience a repulsive force from wall atoms in this region and the repulsive force is the indispensable second stage of the heat exchange interaction mentioned above (b) the magnitude of the z -component force due to the wall atoms $|\ddot{r}_{z-fluid-wall}|$ is greater than the z -component of the attractive/repulsive force due to the neighboring fluid atoms, $|\ddot{r}_{z-fluid-fluid}|$. This condition is based on the concept that the fluid atom must be primarily dominated by the wall force in order to satisfy the requirement that it is receiving energy from the wall atoms. These proposed criteria allow us to numerically simulate the energy exchange due to collisions between the fluid atoms and the wall. The criteria are summarized as:

Thus, if $\left. \begin{array}{l} \text{fluid atom is in Region 3} \\ \text{AND} \\ \left| \ddot{r}_{z-\text{fluid-wall}} \right| > \left| \ddot{r}_{z-\text{fluid-fluid}} \right| \end{array} \right\}$ fluid atom is heated up at the wall temperature. At each

time step, the fluid atoms which meet the above criteria are identified and randomly assigned temperatures within ± 1 K of the wall temperature such that the mean value of the temperatures for these atoms equals the wall temperature.

The step-change in wall temperature incorporated in this model theoretically corresponds to a wall with an infinite thermal conductivity, and the heating time period of the wall is neglected. This was again taken as a reasonable assumption for highly conductive metallic materials since the heating time period for three-molecular layers of platinum would be in the order of 1-10 pico seconds or less. Thus, it is reasonable to neglect the wall heating time and not to affect the physical conclusions. Maruyama and Kimura (1999) used Langevin thermostat to increase the temperature of Pt wall atoms by 10 K; they conclude that the solid wall temperatures “quickly respond” to the temperature change, which strengthens our assumption of neglecting the heating time period for platinum. Regarding the role of electrons in the platinum heater, Yamamoto et al. (2000) studied the structure of a Pt(111)/dipolar liquid interface by fully self-consistent combination of first-principles calculation based on quantum mechanics for the metal and reference hypernetted-chain (RHNC) theory for the liquid. The metal region is represented by a supercell with repeated slabs each of which consists of eleven Pt(111) layers. The liquid is modeled as hard spheres of diameter 0.28 nm embedded with point dipoles. For the liquid molecules, the metal acts as a hard wall. It is assumed that the two phases interact only through electrostatic fields and there is no charge or mass transfer between the two phases. The electrostatic density profile for the metal, density and orientational structure of liquid molecules, and electrostatic potential across the interface and evaluated and discussed. The authors compare

the density and orientation profiles in liquid for metal wall and inert wall (where the liquid feels no electric field). They see that a layer of liquid molecules, which is orientationally ordered, is formed near the metal surface, but extends to about only three molecular diameters from the surface. The density and orientational structure decays very rapidly with distance from the metal surface. The authors mention that their result is in good accord with the recent experimental observations.

Model Validation

The proposed model is validated by evaluating both state-dependent and time-dependent properties. Molecular dynamics simulations are conducted by placing liquid argon between two platinum walls. The validation is divided into two sections.

Internal energy and thermal conductivity

The computational domain is a cuboid with dimensions of 4.794 nm \times 4.794 nm \times 8.238 nm. The domain comprises of 3718 argon atoms at liquid saturation density of 100 K. The Pt walls are placed at $z = 0$ and $z = 8.238$ nm and is made up of a total of 2101 Pt atoms. The fluid-wall boundary condition suggested in this paper is applied here. The initial system temperature is 100 K. The domain, at an intermediate time step, is shown in figure 2-9. The time step is 5 fs. The velocity-scaling period is from 0-500 ps while the equilibration period is from 500-1000 ps. The domain reaches equilibrium during the equilibration period, which is then followed by the heating period. At the start of the heating period (1000-2000 ps), the wall temperature is step-changed to a different temperature and the heating-cooling process of the liquid argon is observed. Two different cases are simulated: (CASE a) lower wall temperature is increased to 110 K while the upper wall temperature is decreased to 90 K, and (CASE b) lower wall temperature is increased to 130 K and the upper wall decreased to 90 K.

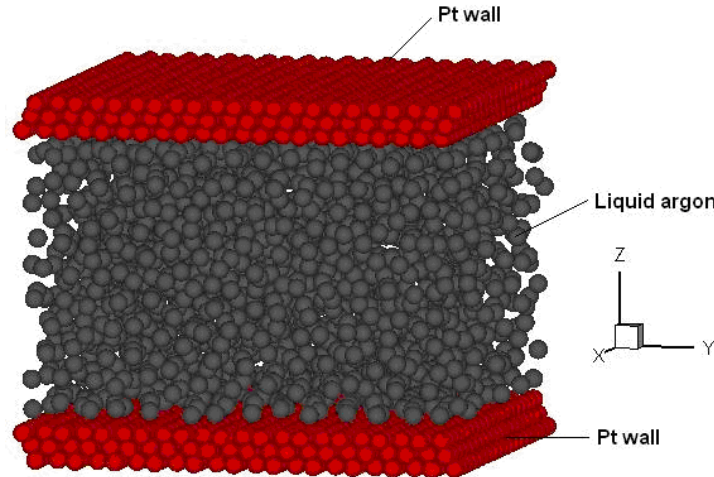
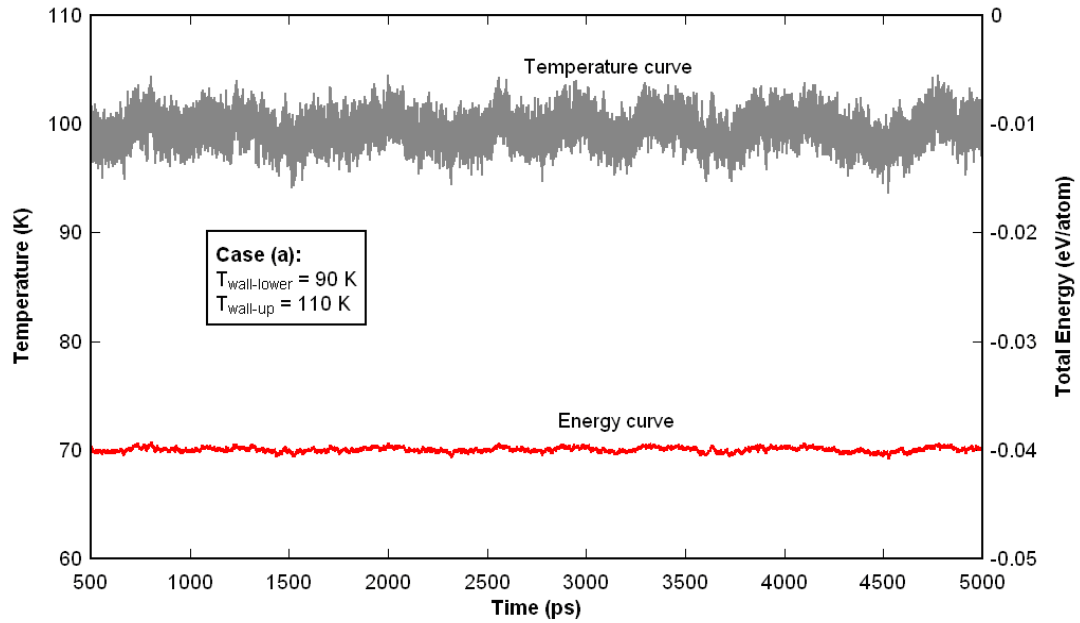
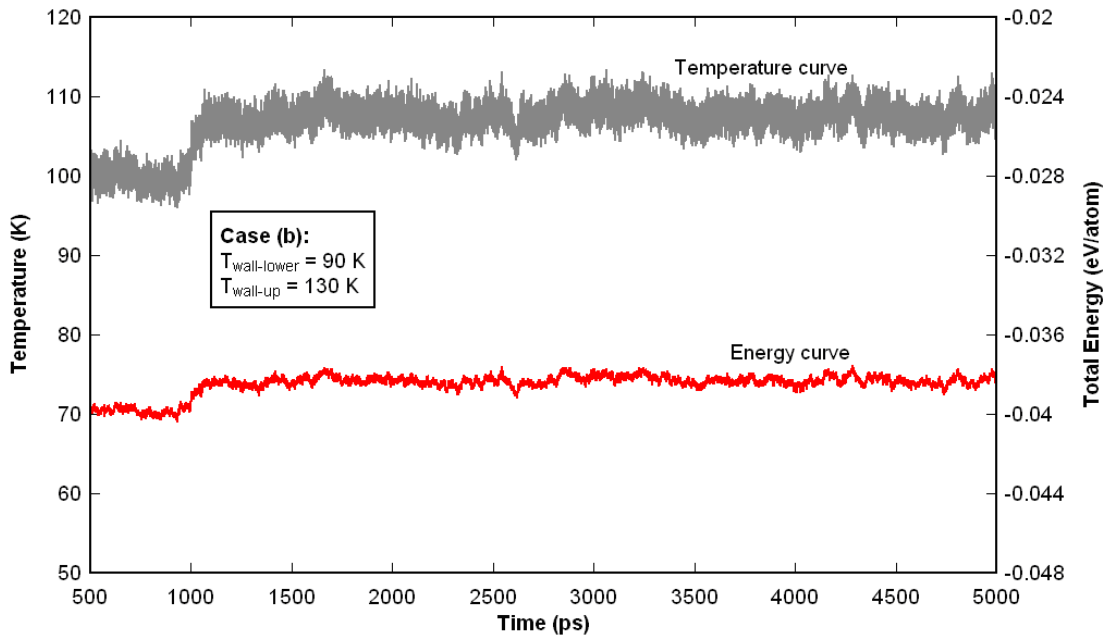


Figure 2-9. Computational domain at an intermediate timestep for validation of proposed wall heat transfer model

The average energy and temperature of the system is evaluated at the initial and final states, and the plots are shown in figure 2-10 (scaling period is not shown). The system temperature for both the cases reaches a value close to the average temperature of the two walls. The values are listed in Table 2-3. The difference in internal energy calculated in the simulation is compared to that obtained from the experimental thermodynamic properties of argon using Engineering Equation Solver which implements a high accuracy equation of state (Klein, 2007). The thermal conductivity of argon is also calculated in the simulations, as outlined in section 2.8.5. The temperature gradient dT/dz is evaluated along the height of the channel and thermal conductivity is determined. These values are compared to the experimental values from thermodynamic properties as listed in Table 2-4. The experimental k values listed are for saturated liquid argon at 100 K and 110 K. The thermal conductivity and change in internal energy values obtained match well with the experimental values for the two cases simulated, which can only happen if the proposed wall-fluid boundary condition is numerically correct. It should be noted here that the internal energy of the fluid is evaluated over the complete fluid domain (including the atoms in the vicinity of the wall).



(a)



(b)

Figure 2-10. Variation of temperature and energy with time for validation of proposed wall heat transfer model (a) lower wall temperature is increased to 110 K while the upper wall temperature is decreased to 90 K; (b) lower wall temperature is increased to 130 K and the upper wall decreased to 90 K

Table 2-3. Change in internal energy for validation of proposed wall heat transfer model

	Equilibration Period (avg. over 500-1000 ps)		Heating Period (avg. over 3000-5000 ps)		Δu_{simul} (kJ/mol)	Δu_{EES} (kJ/mol)	% Error
	Temp. (K)	Internal Energy (kJ/mol)	Temp. (K)	Internal Energy (kJ/mol)			
Case a	99.40	-3.8546	99.54	-3.8546	0	0	–
Case b	99.95	-3.8430	107.83	-3.6925	0.1505	0.155	2.90

Table 2-4. Thermal conductivity for validation of proposed wall heat transfer model

	Heating Period (avg. over 3000-5000 ps)			k_{simul} (W/m.K)	k_{exp} (W/m.K)	% Error
	Temp. (K)	Heat flux (MW/m ²)	Temp. gradient (K/nm)			
Case a	99.54	265.96	-2.331	0.114097	0.10887 [at 100 K]	4.80
Case b	107.83	471.20	-4.316	0.109175	0.09589 [at 110 K]	13.85

Heat equation

Although the previous validation effort provides us with physical soundness of the proposed model, both the thermal conductivity and the change in internal energy are state dependent but time independent. Thus to further validate our model, a similar simulation is performed where the temperature gradient in liquid argon, at different time intervals, is compared with that of the 1-D analytical solution obtained from the heat equation. A 1-D problem, as shown in figure 2-11, can be defined as:

$$\frac{\partial T(z,t)}{\partial t} = \frac{1}{\alpha} \frac{\partial^2 T(z,t)}{\partial z^2} \quad (2.18)$$

Initial condition: $T(z, t = 0) = T_i$

Boundary conditions: $T(z = 0, t) = T_{low}$

$$T(z = h, t) = T_{upp}$$

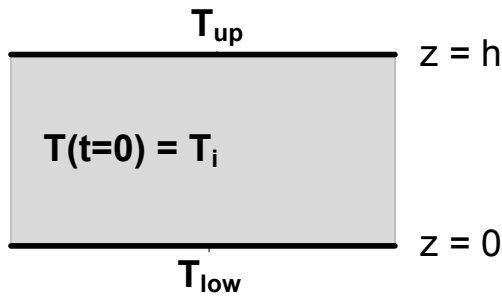


Figure 2-11. 1-D heat problem

The solution to the above equations can be shown to be:

$$T(z,t) = T_{low} + (T_{up} - T_{low}) \frac{z}{H} + \sum_{n=1}^{\infty} \frac{2}{n\pi} \left[(T_{up} - T_i)(-1)^n - (T_{low} - T_i) \right] \sin\left(\frac{n\pi}{H} z\right) e^{-\alpha \left(\frac{n\pi}{H}\right)^2 t} \quad (2.19)$$

where H is the nanochannel height and α is the thermal diffusivity of fluid.

Equation 2.19 will be used to find the analytical solution of temperature gradient in liquid argon at different time intervals. Any of the previous works in literature have not attempted to validate their wall-fluid heating/cooling models by comparing temperature gradient in liquid to analytical solution of the heat equation. Heat conduction is conventionally treated as a diffusion process on the concept of local thermal equilibrium. The local-equilibrium condition breaks down when the characteristic length L is smaller than a mechanistic length, such as the mean free path. For

example, heat conduction across a dielectric thin film when the thickness is much smaller than the phonon mean free path or energy transport across a thin film whose thickness is much smaller than the mean free path, conventional Fourier's law cannot be directly applied. The hyperbolic heat equation, with no heat generation, is defined as:

$$\nabla^2 T = \frac{1}{\alpha} \frac{\partial T}{\partial t} + \frac{\tau_q}{\alpha} \frac{\partial^2 T}{\partial t^2} \quad (2.20)$$

where τ_q is a kind of relaxation time similar to the average time between atomic collisions. The solution of the hyperbolic heat equation is in the form of a propagating wave whose amplitude decays exponentially as it travels. Zhang (2007) shows a sample calculation to compare the heat transfer between Fourier's heat equation and the hyperbolic heat equation for very small and large τ_q . For small τ_q , the parabolic heat equation incorrectly predicts a continuous temperature distribution without any wavefront. But as time passes on, the first order time derivative (i.e. the diffusion term) in the hyperbolic heat equation above dominates. After a sufficiently long time, usually 5 to 10 times τ_q , a local equilibrium is reestablished and the thermal field can be described by the parabolic heat equation. Also, at steady state, the hyperbolic and parabolic equations predict the same results. In the present work, the temperature increase of the wall occurs at 1000 ps. The time step of the MD simulation is taken as 5×10^{-15} s, which is around the same order as the average atomic collision time in liquid argon (10^{-14} to 10^{-15} s). Based on the above theory, the parabolic heat equation should be applicable after ~ 10 to 20 timesteps. The MD simulation is run till 2500 ps, i.e. for an additional 1500 ps (=300,000 timesteps) after the temperature of wall was increased. Thus, the parabolic heat equation results hold during the majority of the time period over which the temperature gradients are evaluated and averaged, as it is much greater than τ_q .

The velocity-scaling period is from 0-500 ps, the equilibration period is from 500-1000 ps followed by the heating period (1000-2500 ps) where the wall temperatures are step-changed to desired temperatures. The computational domain is a cuboid with dimensions of 5.939 nm×5.939 nm×23.657 nm. The domain comprises of 16384 argon atoms at liquid saturation density of 100 K. The Pt walls are placed at $z = 0$ and $z = 23.657$ nm and are made up of a total of 3224 Pt atoms. The initial system temperature is 100 K. The time step is 5 fs. At the end of equilibration period (i.e. $t=1000$ ps), the upper wall temperature is increased to 110 K and the lower wall temperature is decreased to 90 K.

Figure 2-12 shows the variation of average system temperature and energy with time. The system temperature fluctuates about a mean value of 100.43 K and the system mean energy is -0.041164 eV/atom, during the equilibration period. The average system temperature and energy evaluated in the final 500 ps is 99.60 K and -0.041374 eV/atom.

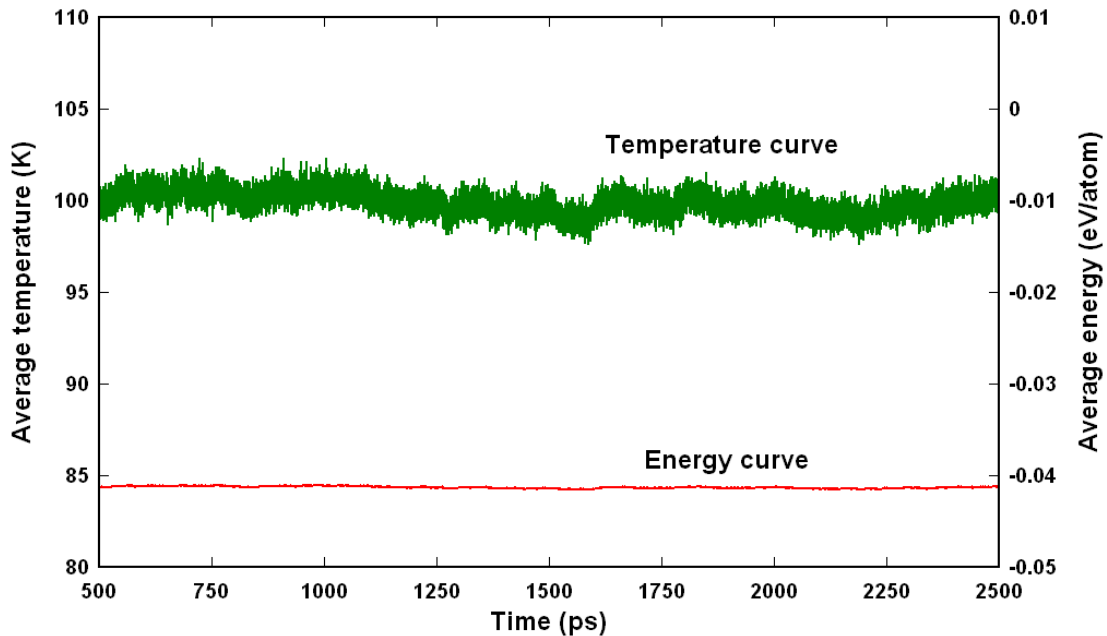


Figure 2-12. Average temperature and energy variation with time of liquid argon time for validation of proposed wall heat transfer model

In order to evaluate the temperature gradient, the domain was divided into 70 equal slices along the height of the channel (i.e. in z direction) and the average temperature of each slice was evaluated at every timestep. The temperature gradient was then averaged over 100 ps (20000 timesteps) to obtain good statistical averages. Hence, if the temperature gradient is averaged from time t ps to $t+100$ ps, the statistical average can be said to hold at $t+50$ ps and the analytical solution is calculated at that timestep. The simulation values are compared to the heat equation's analytical solution (equation 2.19) in figure 2-13. As it can be seen, the results match quite well thus validating the proposed 'fluid-wall thermal equilibrium model' on a temporal basis.

Liquid argon heating from both platinum walls

An additional case was simulated by heating liquid argon from both walls. The computational domain is similar to previous simulation: $5.939 \text{ nm} \times 5.939 \text{ nm} \times 23.657 \text{ nm}$, 16384 argon atoms, and 3224 Pt atoms constituting the walls. The initial system temperature is 100 K. The upper and lower wall temperatures are increased to 120 K at the end of equilibration period (i.e. $t=1000$ ps). The temperature gradient is averaged over 100 ps, and the simulation results are compared to analytical solution in figure 2-14. It can be seen that heat transfer occurs at a faster rate in the nanochannel than evaluated from heat equation's analytical result. This occurrence can be attributed to the length scale of the current case as the heat equation is usually applied at a continuum scale. Hence, faster heating/cooling rate at nano length scale is not unexpected. The results compared well in the previous case (with heating/cooling at the walls) since higher heating rate at the upper wall is matched with higher cooling rate at the lower wall. It is fairly easy to imagine that heat transfer across a nanochannel of an even smaller height (say about 5-10 molecular diameters) would happen at a much higher rate. Also from this conclusion it should be expected that with an increasing nanochannel height, the error between molecular dynamics

simulation result and analytical result would keep decreasing up to a particular channel height, beyond which the results would perfectly match. To verify this point of view, another simulation is conducted with increased nanochannel height as explained below.

The dimensions of computational domain are $5.939 \text{ nm} \times 5.939 \text{ nm} \times 44.357 \text{ nm}$. The height is about ~ 1.9 times the previous case. The domain now consists of 30720 argon atoms, and 3224 Pt atoms. The initial system temperature is 100 K. Similar to previous run, the upper and lower wall temperatures are increased to 120 K at the end of equilibration period (i.e. $t=1000$ ps). Figure 2-15 shows the comparison between simulation and analytical results. It can be seen that the results match better than previous simulation of shorter nanochannel (figure 2-13). In order to find the error, the average temperature of the domain is obtained from the temperature gradients of simulation and analytical results and plotted in figure 2-16 at intervals of 100 ps. The simulations were only run till 2500 ps due to computational limitations and final steady state is not obtained in either case. It can be noticed from the initial error (at 50 ps) that for a shorter channel height, liquid argon gets heated up faster as pointed out earlier. The maximum error for the shorter nanochannel occurs at 1350 ps (analytical temperature = 109.14 K) and the value is 5.01 K. For the larger nanochannel, the error remains nearly the same ~ 3.4 K during the final 1000 ps of simulation. This justifies that the error between MD simulation and heat equation's analytical result depends on length scale of the problem.

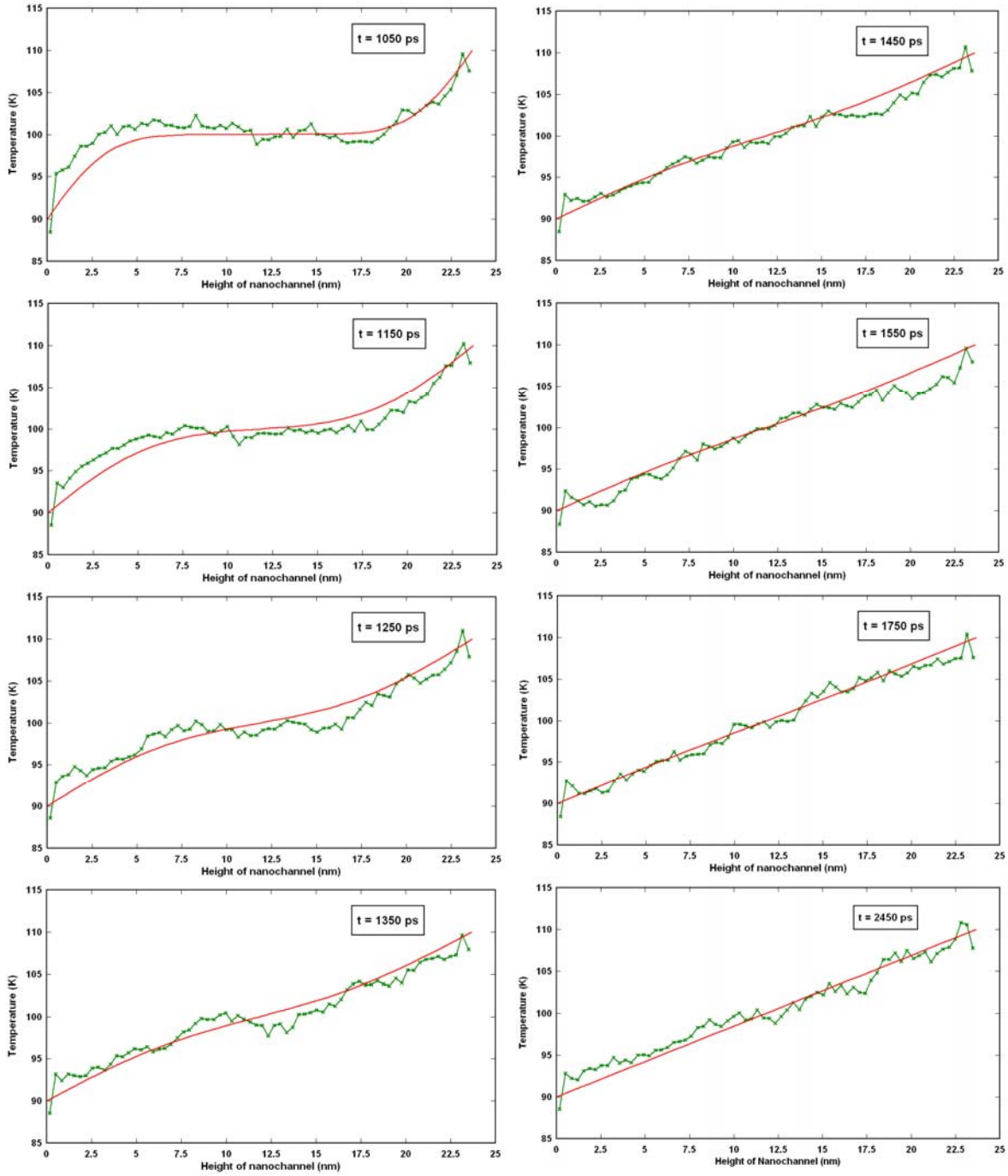


Figure 2-13. Temperature gradient along z-direction at different timesteps for $T_i=100$ K, $T_{up}=110$ K and $T_{low}=90$ K (smooth lines represent analytical solutions)

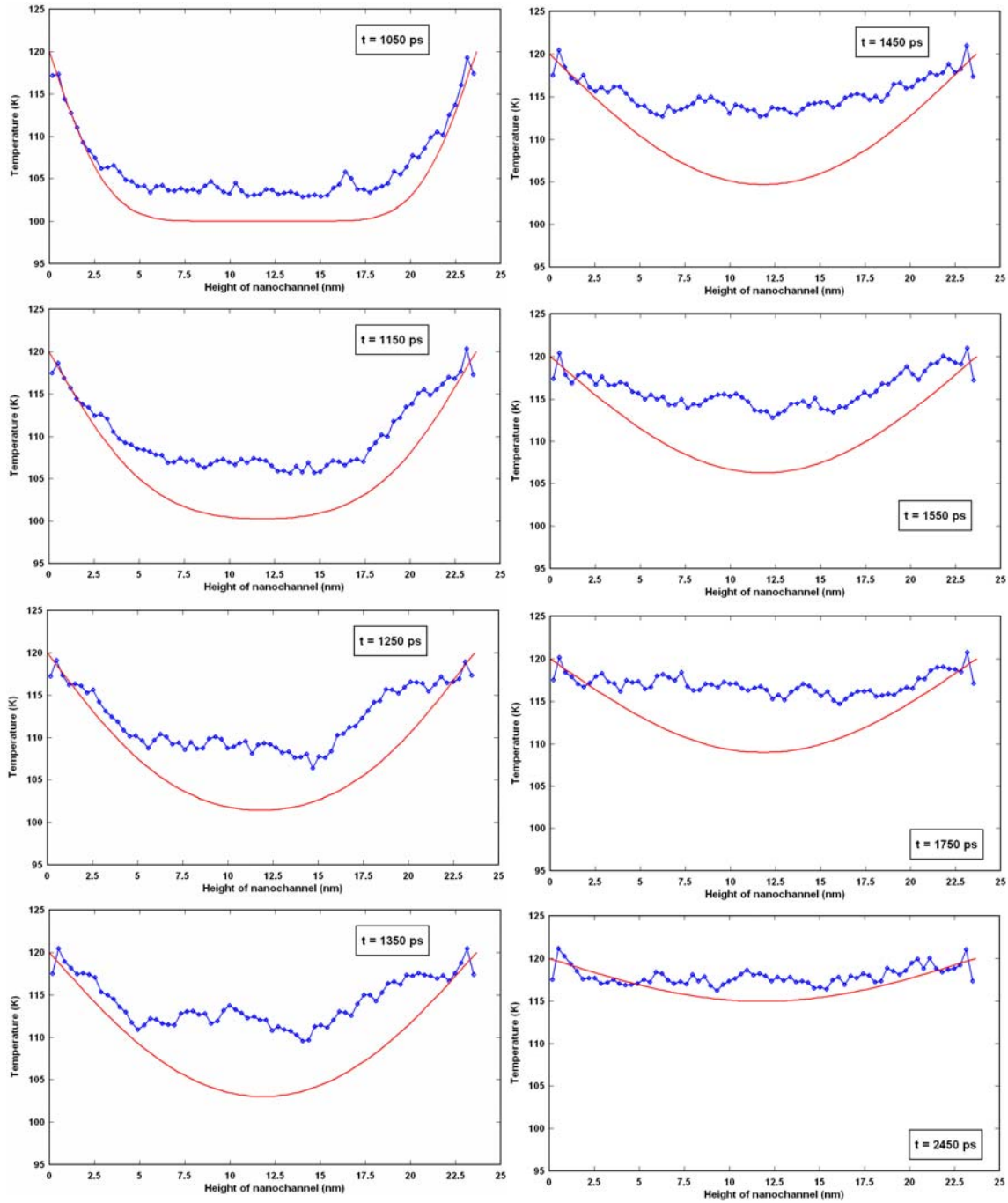


Figure 2-14. Temperature gradient along z-direction at different timesteps for $h=23.657$ nm, $T_i=100$ K, $T_{upp}=120$ K and $T_{low}=120$ K (smooth lines represent analytical solutions)

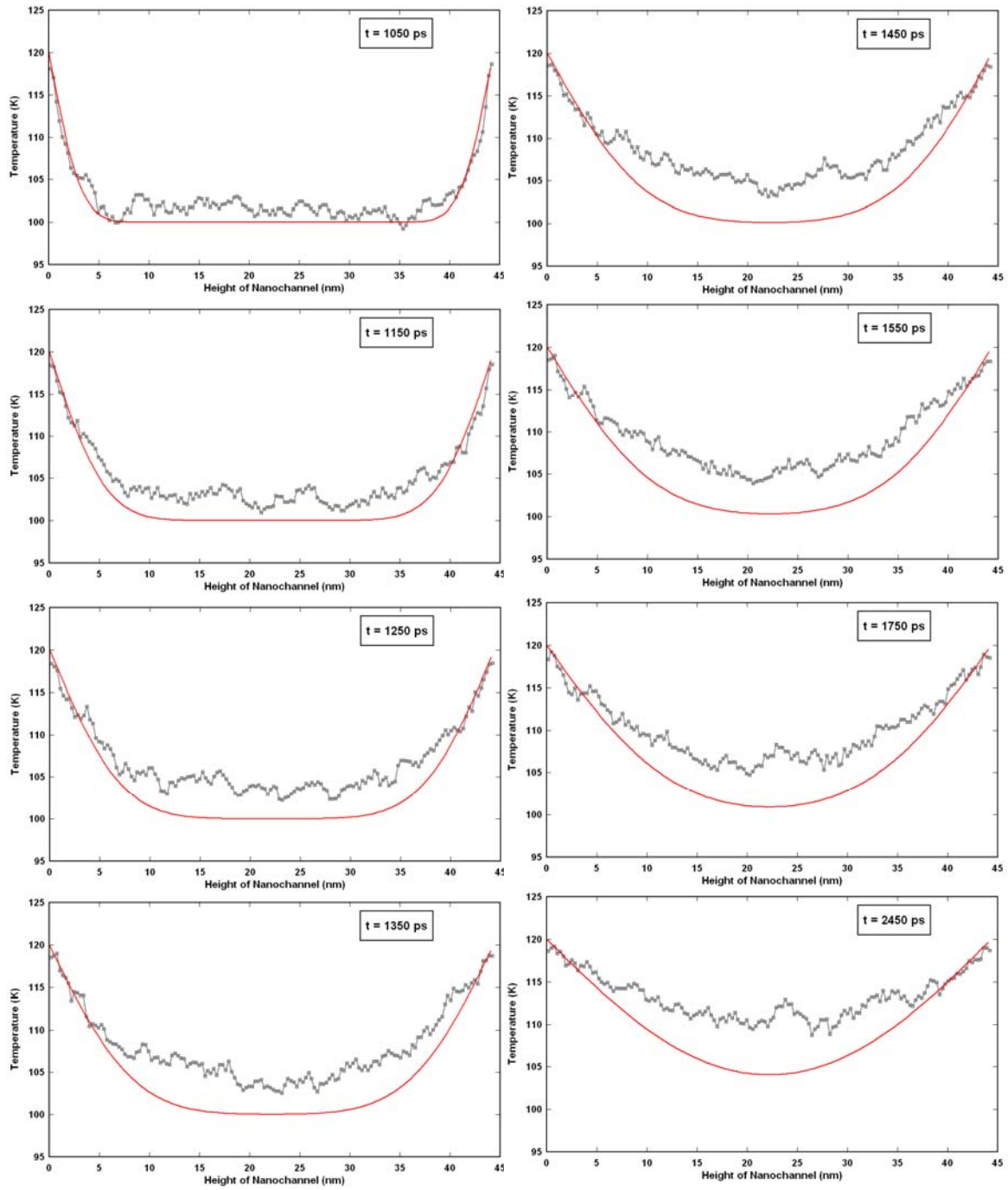


Figure 2-15. Temperature gradient along z-direction at different timesteps for $h=44.357$ nm, $T_i=100$ K, $T_{up}=120$ K and $T_{low}=120$ K (smooth lines represent analytical solutions)

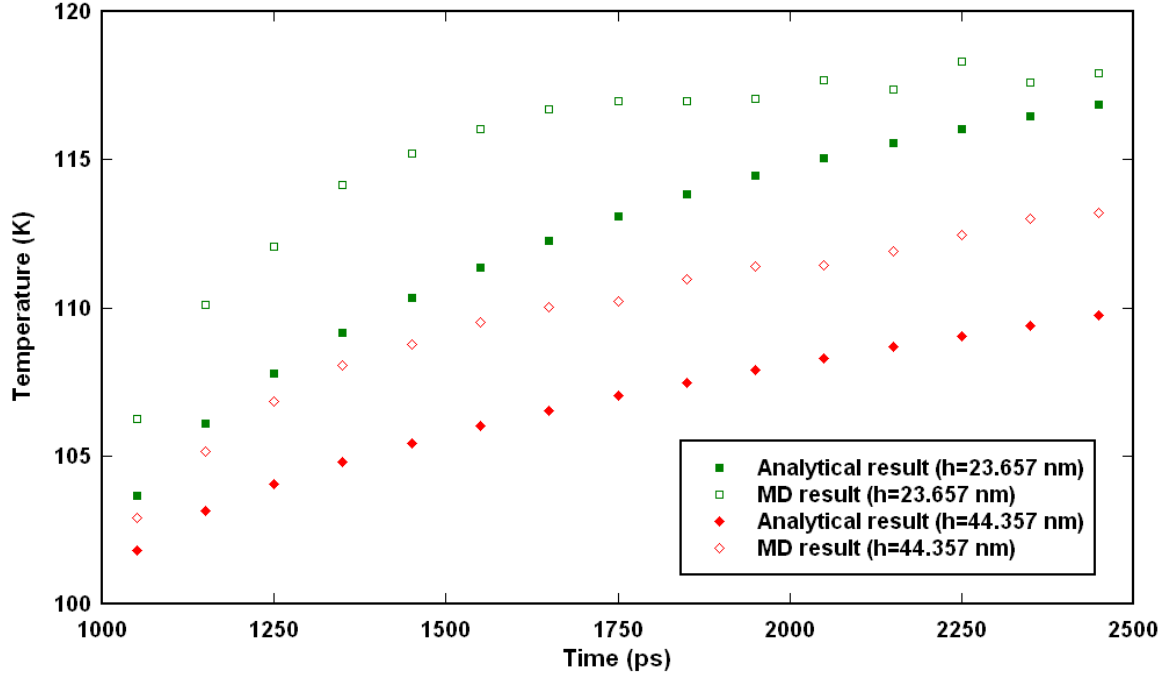


Figure 2-16. Average domain temperatures from MD simulation and analytical equation with heating from both platinum walls for different nanochannel heights

Maxwell speed distribution

The Maxwell speed distribution (MSD) is a probability distribution describing the spread of molecules which are moving around at a given speed. It is derived under the assumption of an ideal gas. Using elementary statistical mechanics, it is easy to find out that the MSD must be proportional to the probability that a particle is moving at a given speed. The MSD can be derived and shown to be equal to the following function:

$$D(v) = \left(\frac{m}{2\pi kT} \right)^{3/2} 4\pi v^2 e^{-mv^2/2kT} \quad (2.21)$$

where m is the mass of the molecule, k is Boltzmann's constant ($= 1.38 \times 10^{-23} \text{ J K}^{-1}$) and T is the temperature. As this formula is a normalised probability distribution, it gives the probability of a molecule having a speed between v and $v+dv$.

The MSD will be used to provide another verification of the proposed ‘fluid-wall thermal equilibrium’ model. At high temperatures, near the critical temperature, argon vapor would behave like an ideal gas. Since the proposed heat transfer model is responsible for imparting kinetic energy to the argon atoms and evaporation, the MSD will serve as a good check as to if the molecular speeds of the vaporized atoms follow the expected normalized probability distribution. In order to do so, a computational domain is set up in the form of a cuboid expressed in Cartesian coordinates with the z-direction denoting the height of the domain. The x, y and z dimension are 11.061 nm, 11.061 nm and 29.954 nm respectively. The four boundaries in x and y directions are periodic. A Pt wall constitutes the lower boundary in the z-direction. A mirror boundary condition is set up at the upper boundary in the z-direction; this implies that the upper boundary is elastic and adiabatic in nature. A thin liquid argon film of thickness 2 nm is placed on the Pt wall. The remaining volume is occupied by argon vapor. The simulation domain contains 5638 argon atoms and 5560 Pt atoms. The time step is 5 fs. Both liquid and vapor are initially at their respective saturation states at 100 K, and equilibrium is attained in the first 1000 ps. After this time period, the liquid atoms at the wall are heated up using the proposed ‘fluid-wall thermal equilibrium’ model with the wall temperature set to 150 K. The simulation is run till 3000 ps. Figure 2-17 shows the variation of number of liquid atoms with time. As it can be seen, evaporation occurs and a non-evaporating film forms on the lower wall similar to as obtained in the previous simulations. The number of liquid atoms forming the non-evaporating film is ~ 513 , and the final average temperature is ~ 135 K. Increasing the domain height (i.e. increasing the vapor volume) will result in complete evaporation. However, since the aim here was to compare the velocity distribution of the argon vapor atoms in the presence of the non-evaporating film, the domain height was taken accordingly. Figure 2-18 shows the velocity

distribution of the vapor atoms at $t=3000$ ps along with the MSD function at the final system temperature. In Fig. 2-18, ΔN is the number of argon vapor atoms whose velocity values lie between V and $V+dV$, N is the total number of vapor atoms and ΔV is the increment of velocity values. It can be seen that the simulation results match well with the MSD function; this verifies that the velocities imparted by the proposed fluid-wall heat transfer model follow expected physics and at high temperatures argon vapor behaves like an ideal gas.

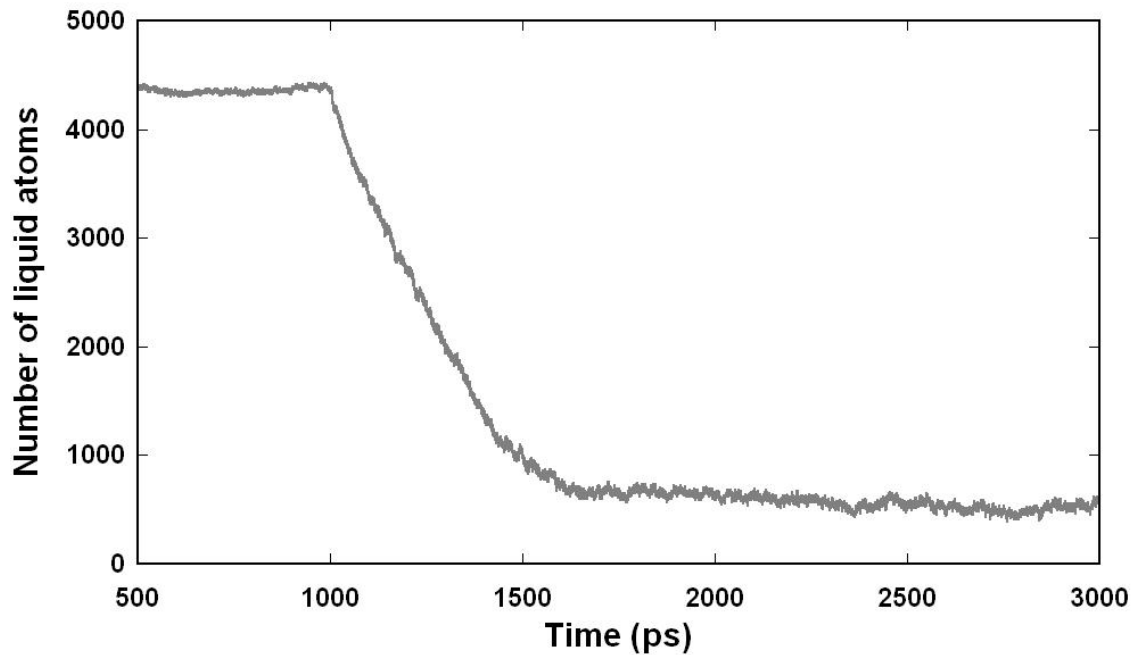


Figure 2-17. Variation of number of liquid atoms with time in the simulation for verification with Maxwell Speed Distribution function

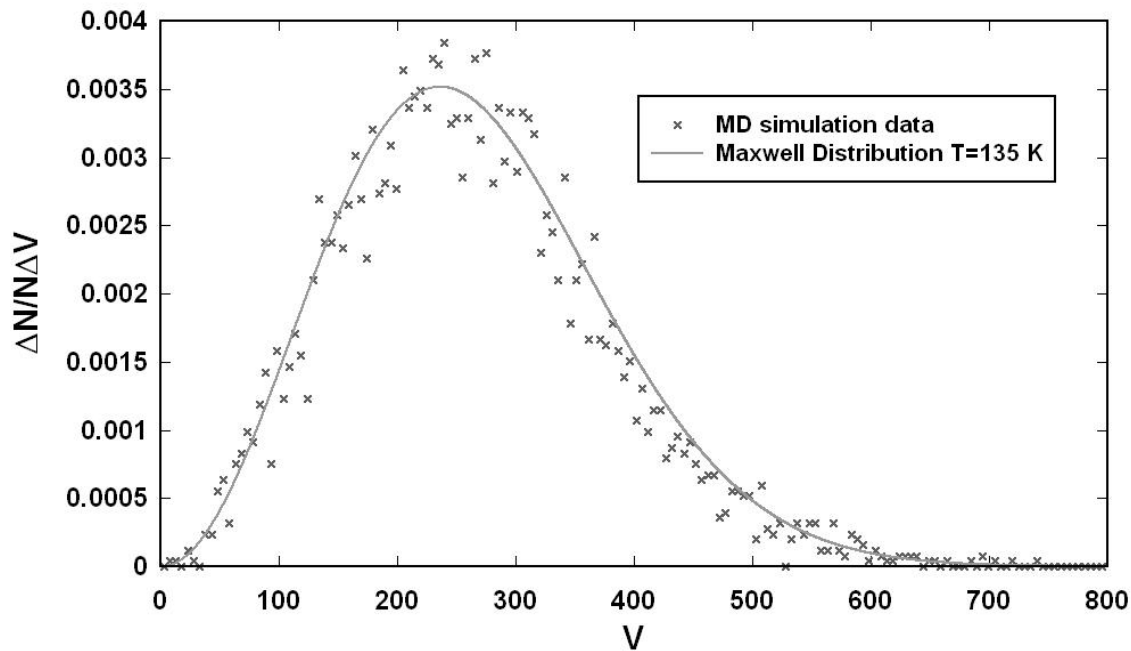


Figure 2-18. Velocity distribution of vapor argon atoms at final equilibrium with a non-evaporating film at the lower wall

Adiabatic Walls

Adiabatic boundaries are very common in heat transfer problems. Thus, the necessity of mimicking adiabatic walls in molecular dynamics simulations is important. As per definition, an adiabatic process is one where no heat transfer occurs across the system boundaries. We simulate a nanochannel formed of platinum walls with liquid argon in between. The platinum walls are present in the z-direction, while the four boundaries in x and y directions are periodic in nature. The dimensions of the argon space in x, y and z directions are 5.78 nm, 5.78 nm and 8.585 nm. The initial equilibrium temperature is 100 K, and the density of liquid argon corresponds to the liquid saturation density at 100 K. A total of 5632 argon atoms and 3066 platinum atoms are present. The wall-fluid interaction is governed only by the Lennard-Jones potential, and the ‘fluid-wall thermal equilibrium’ model is not applied in addition. This forms the basis of adiabatic wall in molecular dynamics simulations. After the velocity-scaling step for the initial

500 ps, the argon atoms are allowed to interact freely for an additional 900 ps. Figures 2-19 and 2-20 show the variation of average temperature and energy with time for two different wall wettability values. The wettability of a surface depends on the ϵ value in the Lennard-Jones equations. As it can be seen, the temperature and energy remain constant throughout the simulation thus showing that, by simulating the fluid-wall interaction only by the Lennard-Jones potential, an adiabatic wall can be simulated.

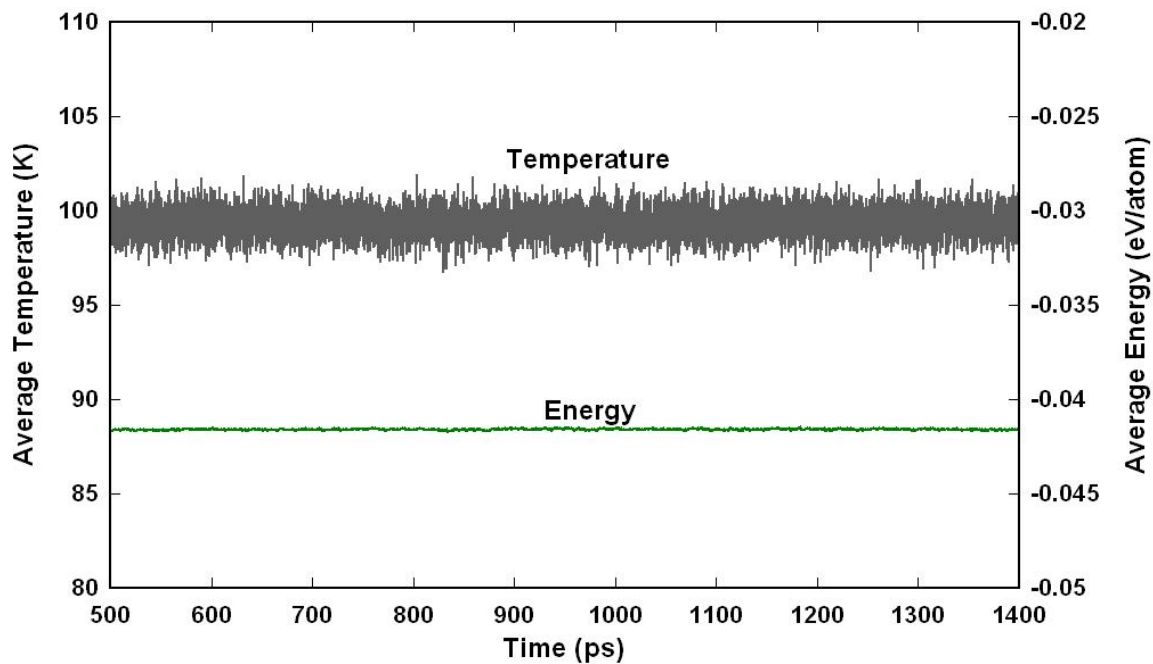


Figure 2-19. Variation of average temperature and energy with time for adiabatic wall with higher wettability $\epsilon = 0.894 \times 10^{-21}$ J

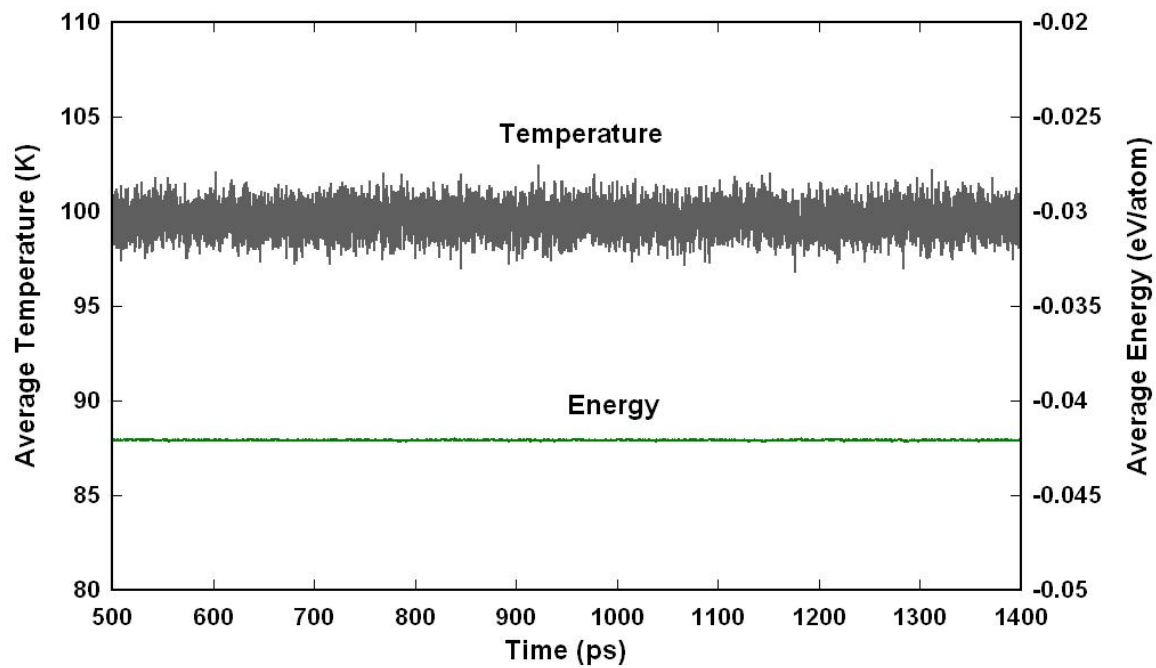


Figure 2-20. Variation of average temperature and energy with time for adiabatic wall with lower wettability $\varepsilon = 0.358 \times 10^{-21}$ J

CHAPTER 3 TRANSIENT FILM EVAPORATION

Transient Film Evaporation

Evaporation of a thin liquid argon film in argon vapor surrounding is simulated to study the phase change process at nanoscale. As theorized in the literature, non-evaporating thin films on the order of nanometers occur in the micro region during bubble nucleation, as well as during meniscus evaporation. This part of the work aims to study nanoscale film evaporation and observe the physics as the film evaporates. Various parameters, like temperature, density, etc are evaluated during the process which is not possible to do in experiments due to the length scale of the problem.

The simulation domain is a cuboid of dimensions $8.011 \text{ nm} \times 8.011 \text{ nm} \times 18.961 \text{ nm}$. An ultra-thin liquid argon film of 2 nm thickness is placed on the Pt wall. The boundaries in x and y directions are periodic in nature. The upper boundary in the z-direction is an imaginary adiabatic wall (mirror boundary condition), and the Pt wall forms the lower boundary. The remaining volume is occupied by argon vapor. Both liquid and vapor are initially at their respective saturation states at 90 K. The simulation domain initially comprises of 2645 liquid film argon atoms, 112 argon vapor atoms and 2929 Pt atoms. The initial structure of the domain is shown in figure 3-1 along with the domain at an intermediate timestep. The velocity-scaling, equilibration and the evaporation (heating) periods are from 0-1000 ps, 1000-2000 ps and 2000-6000 ps respectively. The time step is 5 fs. The Pt wall temperature is step-jumped from 90 K to 130 K at the starting of the evaporation period.

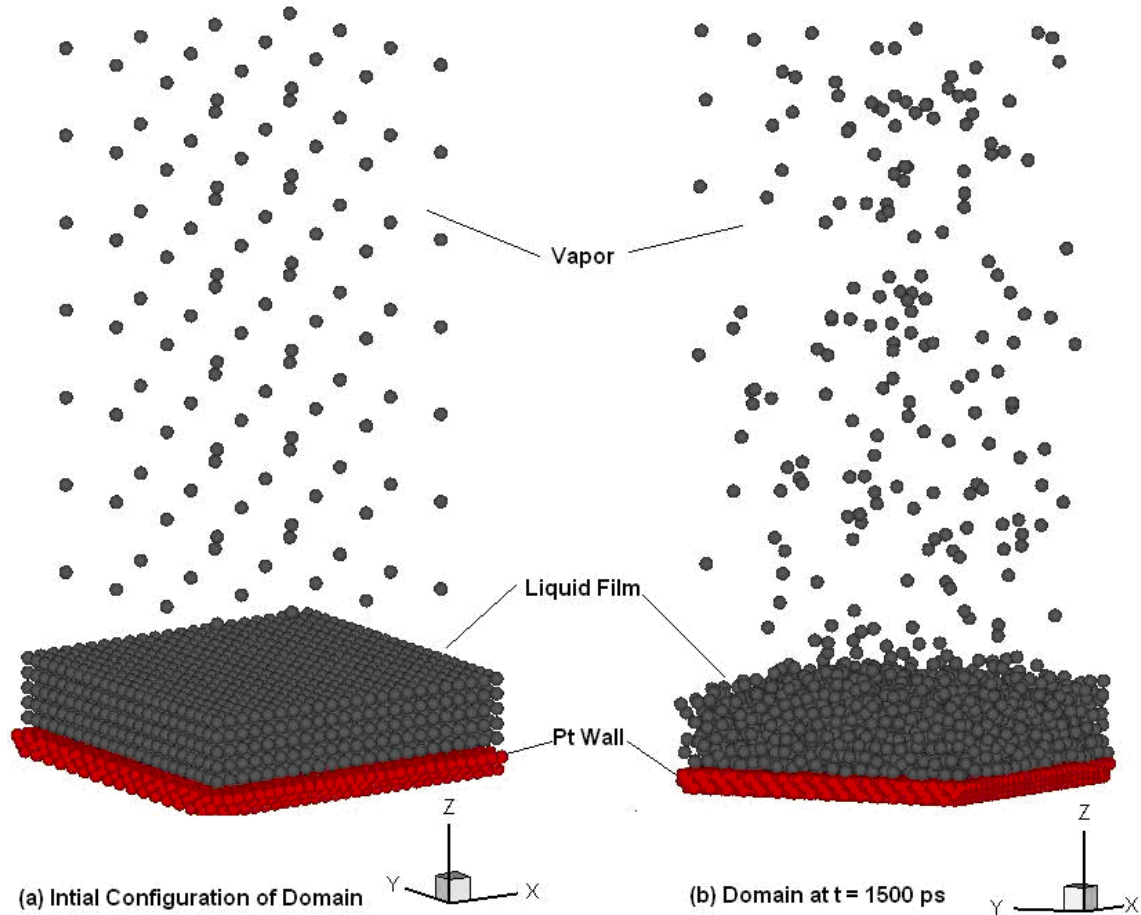


Figure 3-1. Snapshot of transient film evaporation domain

Figure 3-2 shows the variation of average system temperature and energy with time. The system temperature fluctuates about a mean value of 90.43 K and the system mean energy is -0.03145 eV/atom, during the equilibration period. When the Pt wall temperature is increased, the liquid film starts evaporating and the system temperature and energy increase. The average system temperature evaluated in the final 1000 ps is 120.62 K. The curve fit for energy shows that the final equilibrium energy is -0.001545 eV/atom.

The step-change in wall temperature incorporated in this work theoretically corresponds to an infinitely thermal conductive wall, and the heating time period of the wall is neglected. This was again taken as a reasonable assumption for highly conductive metallic materials since

the heating time period for three-molecular layers of platinum would be in the order of 1-10 pico seconds or less. The heating period for the thin-argon film is roughly 600 pico seconds (as seen in Figure 3-2). Due to this large difference, it is reasonable to neglect the wall heating time and not affect the physical conclusions of the current work. Maruyama and Kimura (1999) used Langevin thermostat to increase the temperature of Pt wall atoms by 10 K; they conclude that the solid wall temperatures “quickly respond” to the temperature change, which validates our assumption of neglecting the heating time period for platinum.

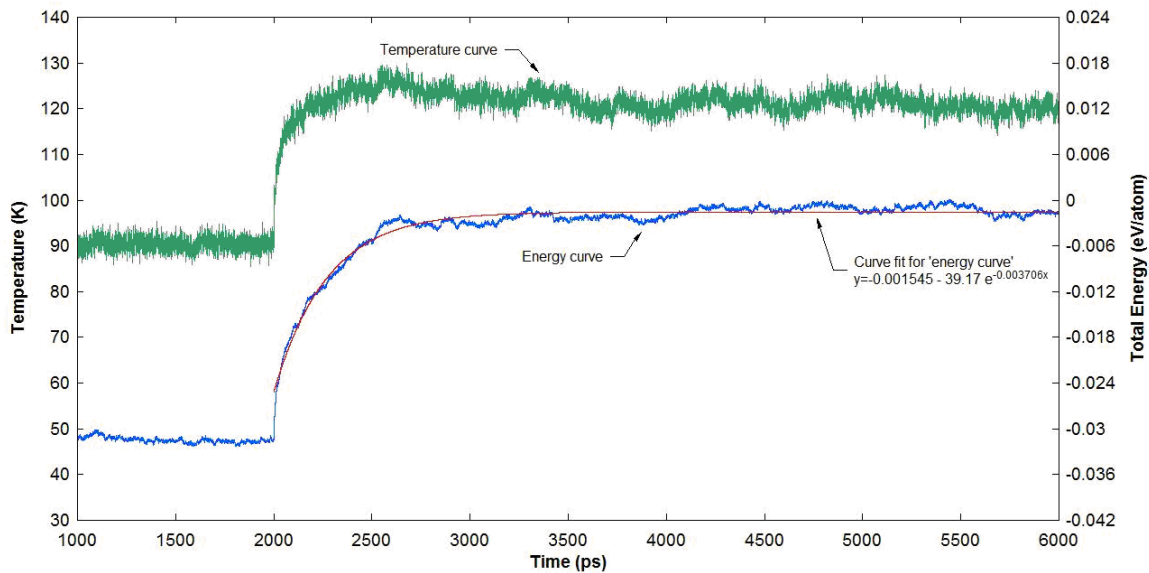


Figure 3-2. Variation of average system temperature and energy with time for transient film evaporation

The number of liquid film argon atoms and vapor argon atoms were determined at each time step and the plot is shown in figure 3-3. During the equilibration period, the number of liquid argon atoms varies to some extent due to the continuous transfer of atoms from the liquid phase to the vapor phase and vice versa at the interface. The lower film starts to evaporate at 2000 ps and the evaporation rate exponentially decreases with time until no further evaporation takes place. The film is said to be non-evaporating on the Pt surface. The curve fit shows this

non-evaporating liquid film to be made up of an average of 868 atoms. This behavior will be explained later on.

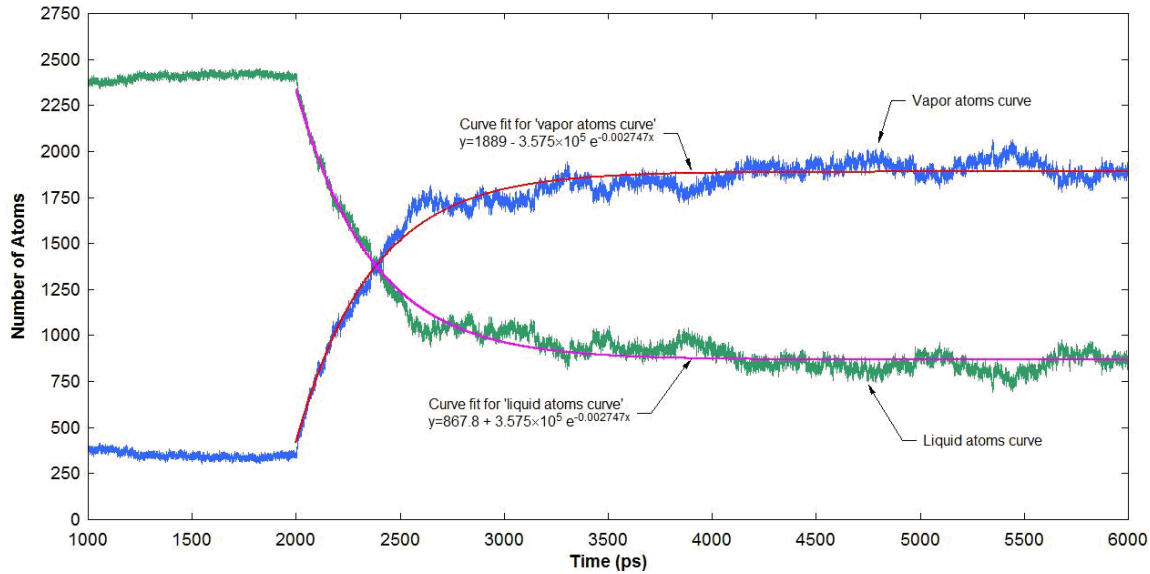


Figure 3-3. Variation of liquid film argon atoms in the domain with time for transient film evaporation

The snapshots of Y-Z plane of the computational domain are shown at different time steps in figure 3-4. After the end of equilibration period, the liquid film can be distinguishably seen clearly defining an interface (Fig. 3-4a). Surface tension assists in stabilizing the interface. The Pt wall atoms are denoted by the triangular symbols in red, the argon atoms forming the liquid film are shown in dark grey and the argon atoms in the vapor phase in light grey. Figures 3-4b through 3-4e demonstrate vaporization of the liquid film. The interface is distorted during the process, and the film become unstable as it evaporates. Figure 3-4f through 3-4h show the non-evaporating liquid film. A gap between the liquid film and the Pt wall can also be noticed which is due to the repulsive nature of Lennard-Jones potential.

The number density profile in the z-direction of the domain is shown in figure 3-5 at different time steps. It is determined by dividing the height of the domain into 55 equal slices,

and counting the number of argon atoms in each slice. The plot also shows the position and the thickness of the interface. The liquid film thickness can be seen to be decreasing initially and the system attains equilibrium towards the end of the simulation as there is negligible change in the number density profiles.

Figure 3-6 shows the averaged temperature distribution along the height of the domain for different time intervals. For the time interval $t=2000-3000$ ps, during which maximum net evaporation takes place, a positive temperature gradient is established along the height of the domain. When the evaporation process begins, atoms from the liquid film move to the vapor region; as the height of the domain is comparable to the mean free path of the atoms, the region near the upper imaginary adiabatic wall gets heated up more compared to the rest of the domain. This also explains the initial temperature jump which can be seen in figure 3-2. For the later times when no net evaporation occurs, the vapor atoms “mix” among themselves to obtain a nearly-constant temperature distribution. Thus it can be concluded that the dominating mode of phase change heat transfer in nanochannels is molecular evaporation accompanied with high evaporation rates.

Figure 3-6 also shows a large temperature gradient in the non-evaporating film. There is a temperature jump at the solid-liquid interface, similar to Maruyama and Kimura (1999) which was regarded as the thermal resistance over the interface. The temperature jump obtained in the present study is 2.8 K, and the temperature gradient in the non-evaporating film is -9.64 K/nm.

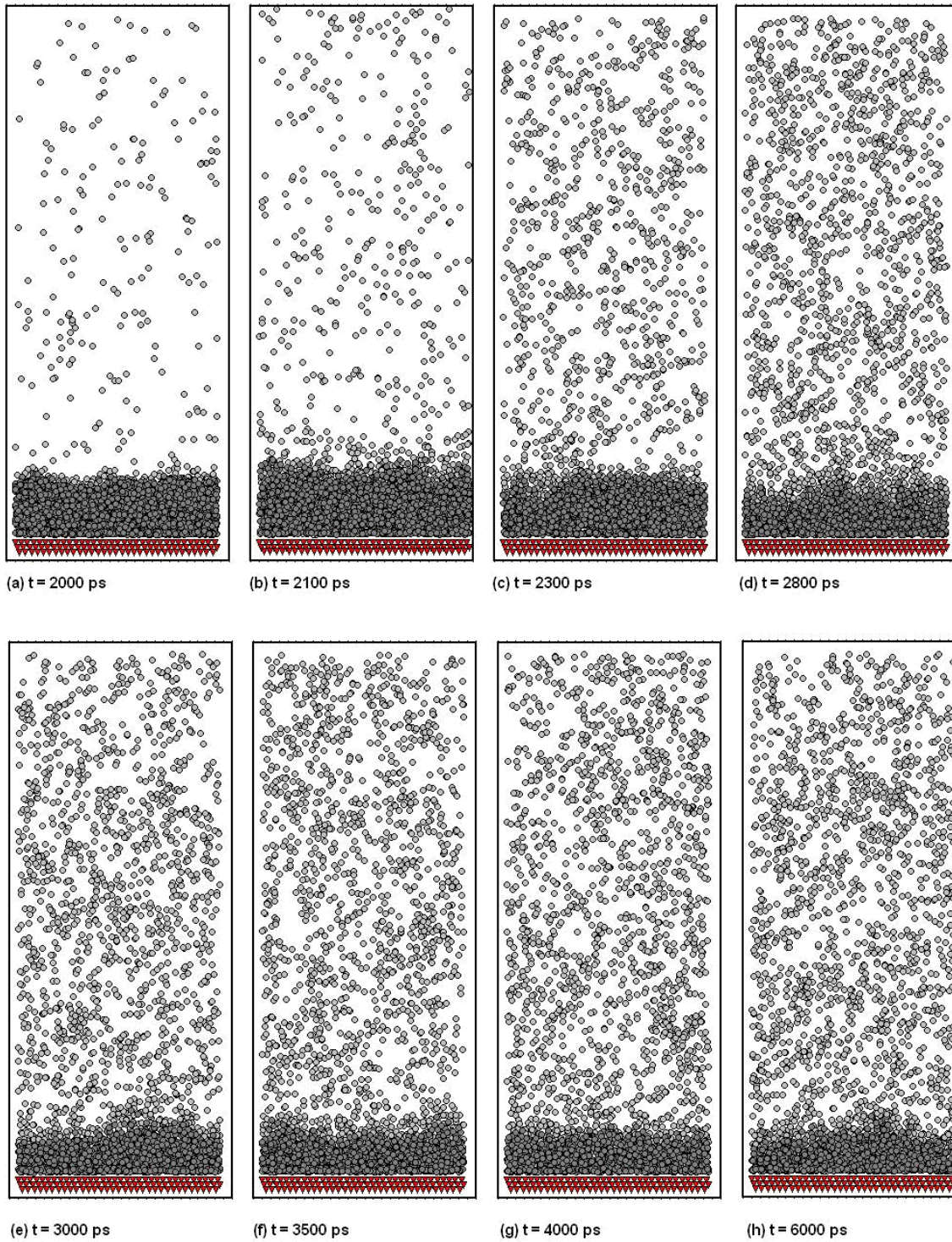


Figure 3-4. Projection of the Y-Z plane of the simulation domain at different time intervals for transient film evaporation

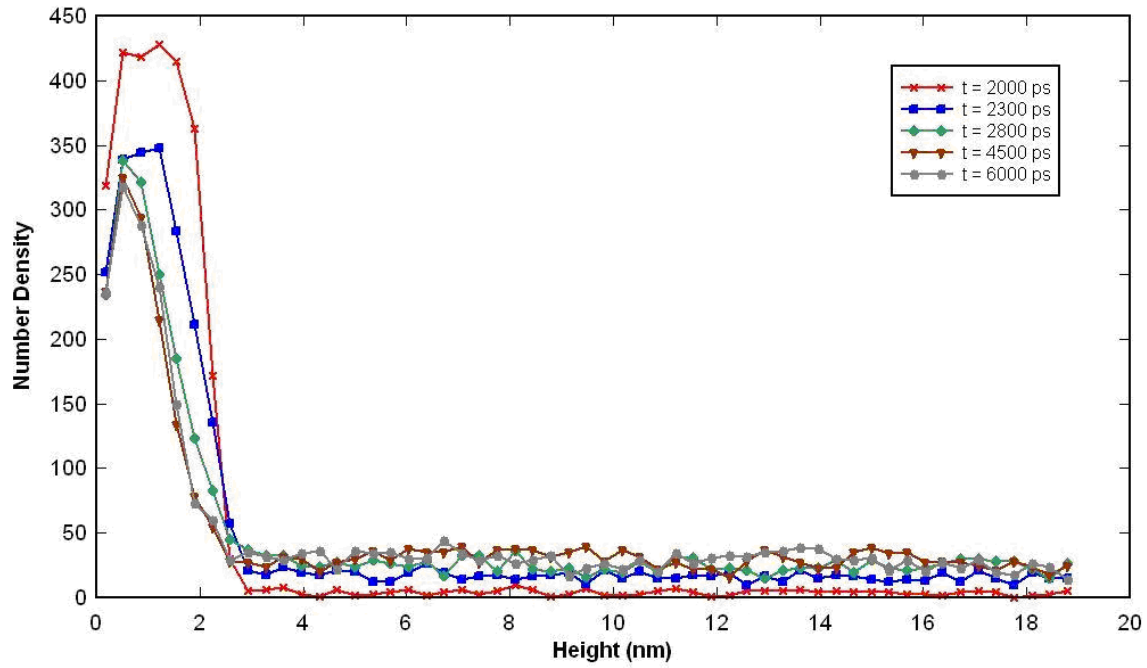


Figure 3-5. Number density profiles at different time steps for transient film evaporation

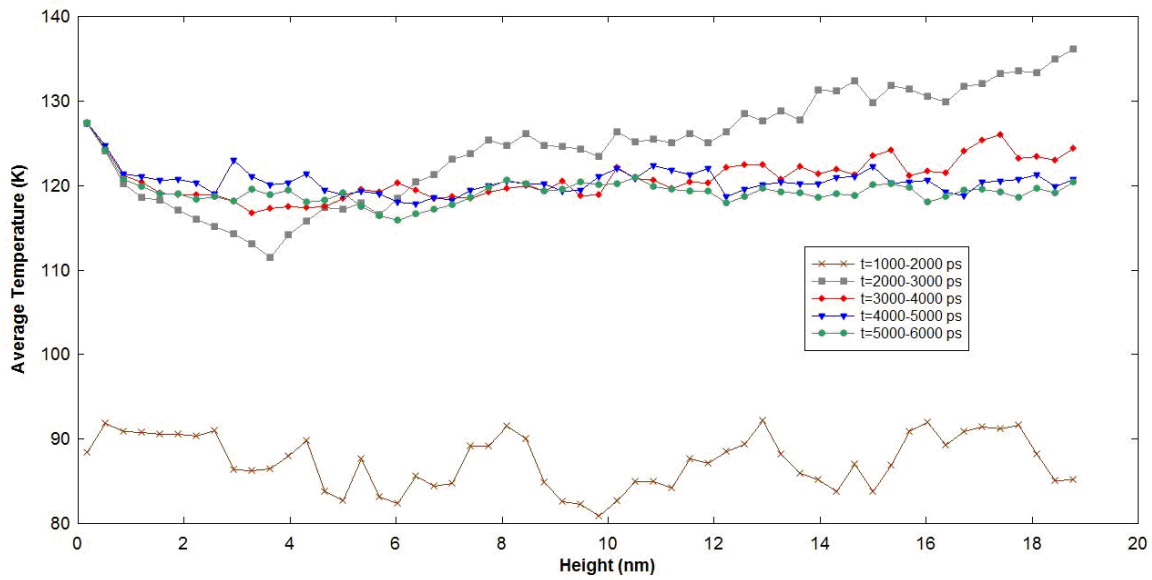


Figure 3-6. Averaged temperature distribution profile for transient film evaporation

Figure 3-7 shows the averaged number density profiles along the height of the domain for different time intervals. The average interface thickness is defined as the distance over which the largest gradient in density occurs. The interface position is taken to be midway over the interface thickness. The interface position and the thickness during the equilibration period are 2.241 nm and 0.689 nm respectively, whereas their values during $t=5000-6000$ ps are 1.362 nm and 1.0343 nm respectively.

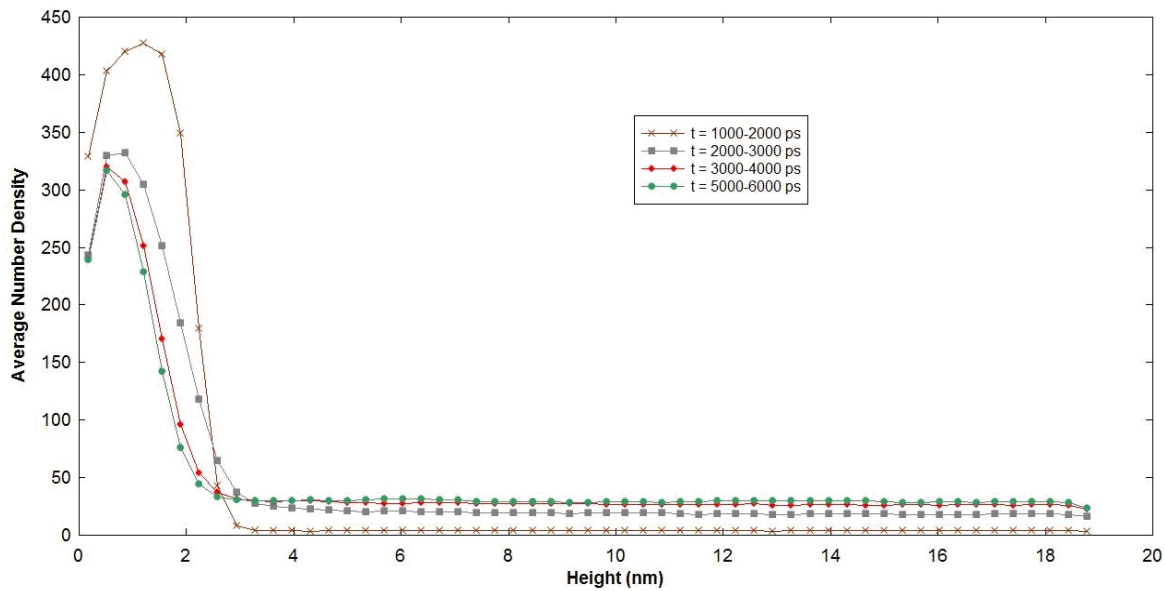


Figure 3-7. Averaged number density profile for transient film evaporation

The reason for the non-evaporating film can be attributed to the following factors: pressure in the vapor region, temperature of the wall and the wall-fluid interaction force. The pressure increase in the vapor region causes hindrance to evaporation, and thus increases the condensation rate. The Van der Waal's force of attraction (governed by the wall-fluid interaction model) also plays a role in determining the thickness of the non-evaporating film making the value of energy scale parameter in the LJ potential crucial. The temperature of the wall determines the kinetic energy provided to the liquid atoms. The non-evaporating film acts as an insulation due to which no further heat transfer occurs and the heat transfer coefficient value

become zero, similar to the results obtained before the interline region for a non-evaporating liquid film.

Heat Flux and Evaporation Rates

The heat transfer rate and the net evaporation rate per unit area are shown in figure 3-8. They are obtained by differentiating the curve fits of energy (Figure 3-2) and number of vapor atoms (Figure 3-3). Figure 3-8 also shows the time when 90% and 95% of total evaporation and heat transfer is completed. The maximum heat flux and evaporation rates are 603.39 MW/m^2 and 4208.5 kg/s.m^2 respectively. It should be noted that the net evaporation rate is the difference between the evaporation and condensation rates. Thus when the net evaporation rate becomes zero it means that the evaporation rate equals the condensation rate. As this is an ultra thin film, the majority of atoms in the film keep evaporating and are replaced by the condensing vapor atoms. The film can be considered to be adsorbed at a given instant in time between $\sim 4000\text{-}6000$ ps.

Evaluation of Hamaker Constant from Molecular Dynamics Simulation

A Hamaker-type analysis is done here to obtain the value of A for Pt-Ar interaction which is not available in the literature. To the best of our knowledge, this kind of analysis involving the calculation of Hamaker constant using molecular dynamics has not been attempted before. In addition, we would like to stress the point that this method outlined below is applicable to other solid-wall combination as long as their interaction potential is appropriate and depicts real situations. The Lennard-Jones potential has been widely used and accepted for Ar-Pt interaction in literature. The interaction between the Pt and Ar atoms is represented by the Lennard – Jones potential:

$$U_{LJ}(r) = 4\epsilon \left[\left\{ \left(\frac{\sigma}{r} \right)^{12} - \left(\frac{\sigma}{r} \right)^6 \right\} \right] \quad (3.1)$$

where $\varepsilon = \varepsilon_{Ar-Pt}$ and $\sigma = \sigma_{Ar-Pt}$. The interactive energy per unit area between an argon plate of thickness t at a distance d from a semi-infinite Pt wall is determined analogous to the way shown by Stokes (2001).

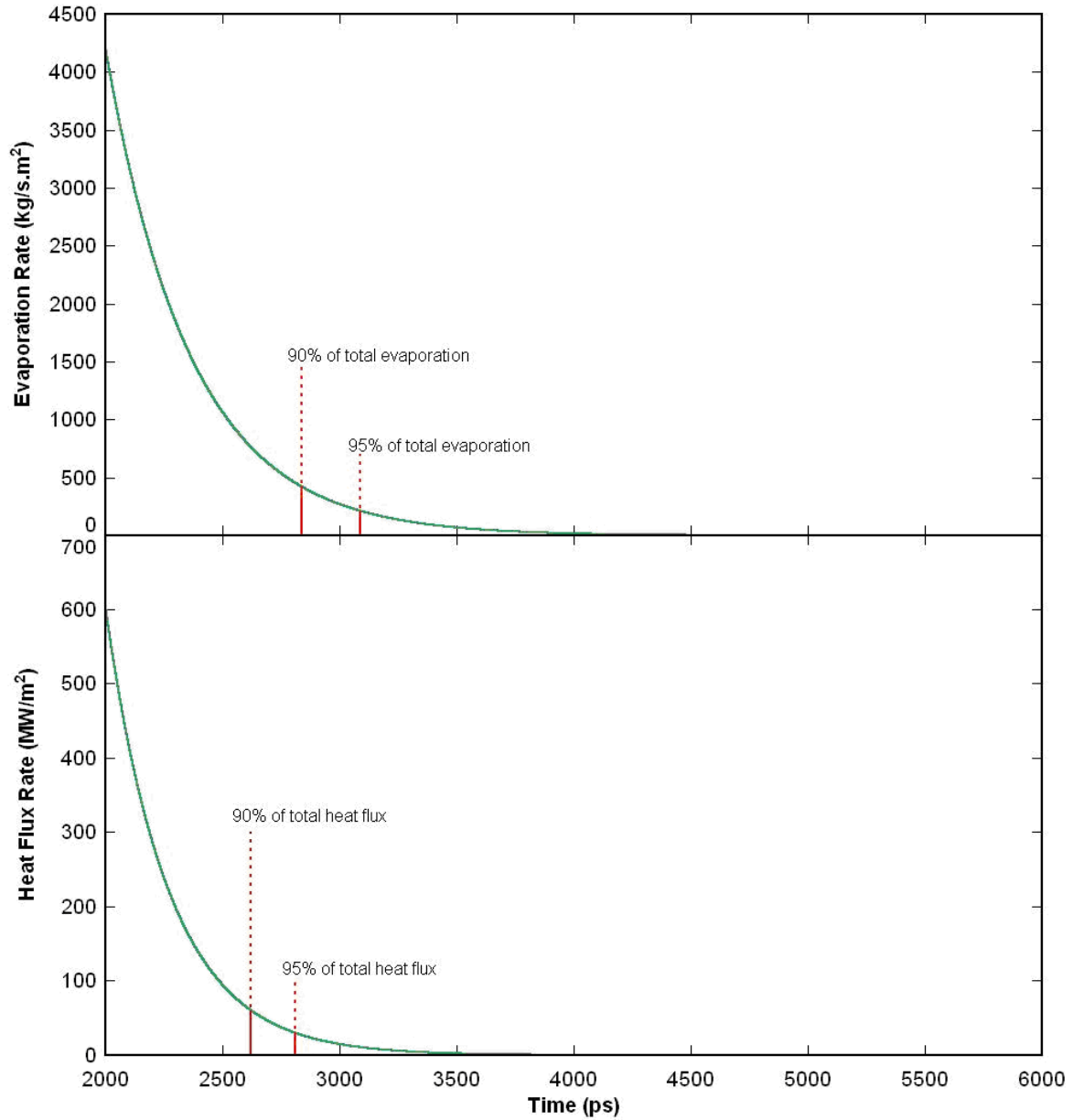


Figure 3-8. Evaporation flux and heat flux rates for transient film evaporation

The interaction between a Pt atom and an Ar block is first considered as shown in figure 3-9a.

The volume of the ring shaped element equals $2\pi y dy d\xi$.

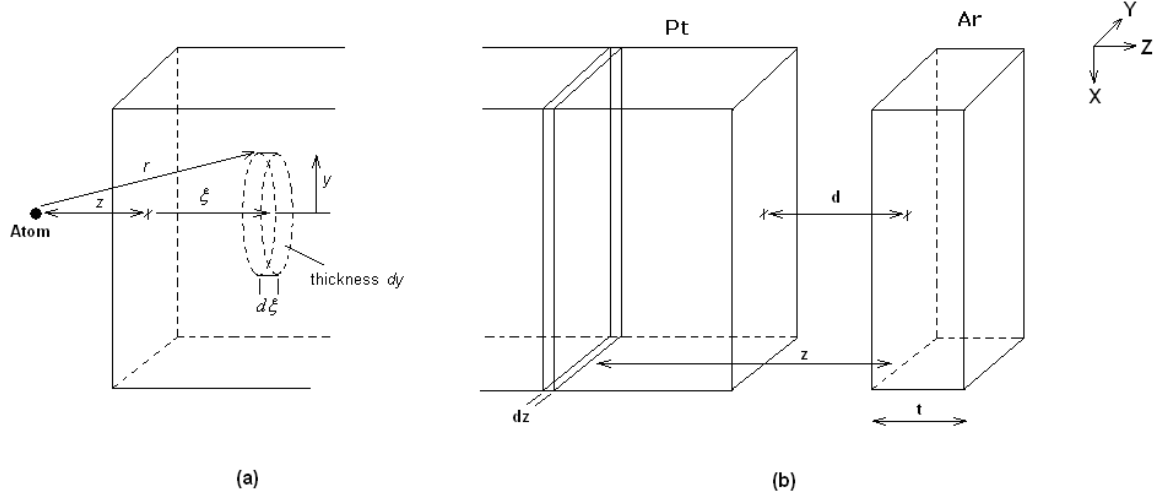


Figure 3-9. Sketch showing the coordinates for calculating the interaction energy between (a) a Pt atom and Ar block (b) semi-infinite Pt block and Ar block

The interaction potential between the single Pt atom and all the atoms in the small volume element becomes:

$$dU(r) = 4\varepsilon \left[\left\{ \left(\frac{\sigma}{r} \right)^{12} - \left(\frac{\sigma}{r} \right)^6 \right\} \right] \left(\frac{\rho N_{av}}{M} \right)_{Ar} 2\pi y dy d\xi \quad (3.2)$$

where $(\rho N_{av}/M)_{Ar}$ is the number of atoms per unit volume in the Ar block.

Representing r in terms of z and ξ and rewriting equation 3.2.

$$dU(z) = 4\varepsilon \left[\left\{ \left(\frac{\sigma}{\sqrt{(z+\xi)^2 + y^2}} \right)^{12} - \left(\frac{\sigma}{\sqrt{(z+\xi)^2 + y^2}} \right)^6 \right\} \right] \left(\frac{\rho N_{av}}{M} \right)_{Ar} 2\pi y dy d\xi \quad (3.3)$$

Integrating equation 3.3 for all values of y from zero to infinity and of ξ from zero to t :

$$dU(z) = 4\varepsilon \int_0^t \int_0^\infty \left[\left(\frac{\sigma}{\sqrt{(z+\xi)^2 + y^2}} \right)^{12} - \left(\frac{\sigma}{\sqrt{(z+\xi)^2 + y^2}} \right)^6 \right] \left(\frac{\rho N_{av}}{M} \right)_{Ar} 2\pi y dy d\xi \quad (3.4)$$

Carrying out this integration gives:

$$U(z) = -4\varepsilon \left(\frac{\rho N_{av}}{M} \right)_{Ar} \frac{\pi\sigma^6}{90} \left[\frac{15}{z^3} - \frac{15}{(z+t)^3} - \frac{2\sigma^6}{z^9} + \frac{2\sigma^6}{(z+t)^9} \right] \quad (3.5)$$

Now to determine the interaction energy between the semi-infinite Pt block and the Ar block, the atom shown in Figure 3-9b is considered to be one of many atoms in the Pt block. Thus all the atoms in the Pt block located at a distance x from the Ar block have an energy given by equation 3.5. A volume element dz in the Pt block will have $(\rho N_{av}/M)_{Pt} dz$ atoms per unit area, and

hence the interaction potential per unit area can be given by:

$$dU(z) = -4\varepsilon \left(\frac{\rho N_{av}}{M} \right)_{Ar} \left(\frac{\rho N_{av}}{M} \right)_{Pt} \frac{\pi\sigma^6}{90} \left[\frac{15}{z^3} - \frac{15}{(z+t)^3} - \frac{2\sigma^6}{z^9} + \frac{2\sigma^6}{(z+t)^9} \right] dz \quad (3.6)$$

Integrating equation 12 for $z = d$ to ∞ gives the interaction energy per unit surface area of a semi-infinite Pt block and an Ar block of thickness t as:

$$U(d) = -\frac{A}{12\pi} \left[\frac{1}{d^2} - \frac{1}{(t+d)^2} - \frac{\sigma^6}{30d^8} + \frac{\sigma^6}{30(t+d)^8} \right] \quad (3.7)$$

The last two terms in equation 3.7 appear due to the repulsive terms of the LJ potential.

Here A is a Hamaker-constant parameter which is derived to be:

$$A = 4\varepsilon \left(\frac{\rho N_{av}}{M} \right)_{Ar} \left(\frac{\rho N_{av}}{M} \right)_{Pt} \sigma^6 \pi^2 \quad (3.8)$$

This expression is similar to the general expression in literature as seen from equation 1.1. The modified LJ potential (equation 3.1), used in this simulation, is used to determine the energy of interaction per unit surface area between the liquid argon atoms and Pt wall atoms for the time

period 5000-6000 ps at time intervals of 50 ps. The non-evaporating liquid film is treated as the plate of thickness t and the thickness of the gap being d is the distance between the wall and the closest liquid film atom to it. The average value of A is obtained, from equation 13 as $5.2759 \times 10^{-20} J$ with a standard deviation of 7.68%. The typical value of Hamaker constants are of the order of 10^{-20} and $10^{-21} J$ (Butt et al., 2005). For further validation, the value of A is also obtained from equation 3.8 which does not use force evaluation. This value equals $8.5563 \times 10^{-20} J$ which shows good agreement with the one obtained above. This analysis attempts to outline a general procedure for evaluating the Hamaker constant by molecular dynamics simulation, thus providing a link for using molecular dynamics simulation results in continuum modeling.

Parameters Governing the Formation of Non-Evaporating Film

The previous section is extended further to gain better understanding on the occurrence of the non-evaporating film, and the parameters which govern its formation. The mirror boundary condition is replaced by an additional platinum wall with a thin film, thus making the problem symmetric in nature. Vapor pressure is also evaluated in the simulations. Seven cases are simulated to study the effect of nanochannel height, initial film thickness and temperature on heat flux rate, evaporation flux rate and Hamaker constant.

The simulation domain is a nanochannel in the form of a cuboid as shown in figure 3-10. The x and y dimensions are $6.117 \text{ nm} \times 6.117 \text{ nm}$ respectively; z-direction represents the channel height. The four boundaries in x and y directions are periodic; two Pt walls constitute the boundaries in the z-direction. A thin liquid argon film of thickness t_{film} is placed on each Pt wall. The remaining volume is occupied by argon vapor. Both liquid and vapor are initially at their respective saturation states at 90 K. The simulation domain contains 3465 Pt atoms. The time

step is 5 fs. The velocity-scaling period is 0-500 ps, the equilibration period is from 500-1000 ps and the heating period is from 1000-4000 ps. Nanochannel height h (case 1-3) and initial film thickness t_{film} (case 4-6) are varied, and simultaneous evaporation-condensation (case 7) is simulated. The details of seven cases studied are listed in Table 3-1.

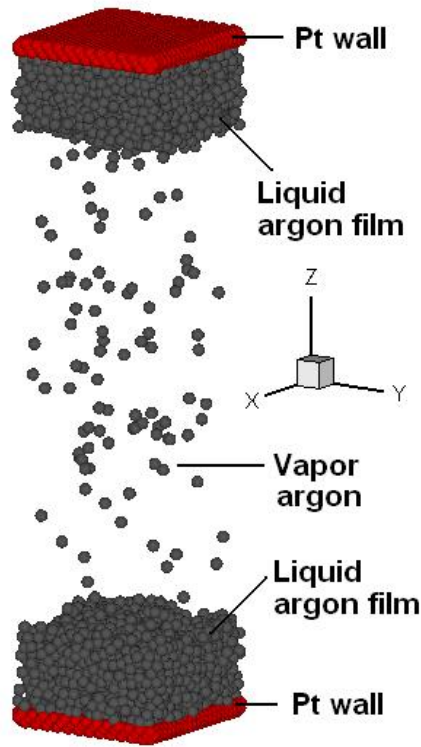


Figure 3-10. Snapshot of simulation domain of nanochannel

Table 3-1. Parameters for seven cases simulated in nanochannel

	h (nm)	t_{film} (nm)	$T_{up\ wall}$ (K)	$T_{low\ wall}$ (K)	No. of argon atoms
Case 1	16.32	3	130	130	4669
Case 2	25.5	3	130	130	4714
Case 3	35.7	3	130	130	4768
Case 4	25.5	2	130	130	2989
Case 5	25.5	4	130	130	6439
Case 6	25.5	5	130	130	8164
Case 7	25.5	3	130	90	4714

Figure 3-11 shows the variation of average system temperature and energy with time for case 4. The system temperature fluctuates about a mean value of 90.99 K and the system mean

energy is -0.0342397 eV/atom, during the equilibration period. When the Pt wall temperature is increased, the liquid film starts evaporating and the system temperature and energy increase. The average system temperature evaluated in the final 1000 ps is 123.99 K. The curve fit for energy shows that the final equilibrium energy is -0.0088331 eV/atom.

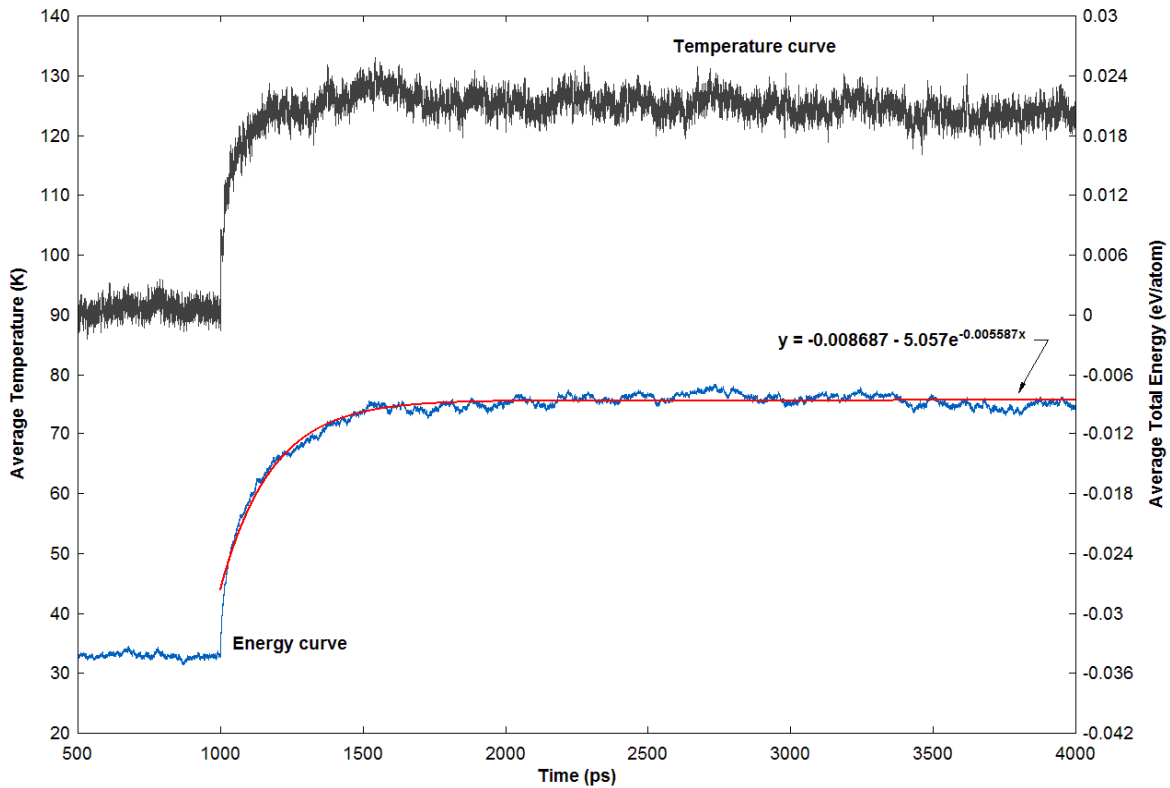


Figure 3-11. Variation of average system temperature and energy with time for case 4

The number of liquid film argon atoms and vapor argon atoms were determined at each time step and the plot for vapor atoms is shown in figure 3-12. The films start to evaporate at 1000 ps and the evaporation rate exponentially decreases with time until no further evaporation takes place. The snapshots of x-z plane of the computational domain are shown at different time steps in figure 3-13, similar to figure 3-4. After the end of equilibration period, the liquid film can be distinguishably seen clearly defining an interface (Fig. 3-13a). Surface tension assists in stabilizing the interface. The Pt wall atoms are denoted by the triangular symbols in red, the

argon atoms forming the liquid films are shown in dark grey and the argon atoms in the vapor phase in light grey. Figures 3-13d and 3-13e show the formation of non-evaporating liquid film.

Figure 3-14 shows the averaged number density profiles along the height of the domain for different time intervals. It is determined by dividing the height of the domain into 90 equal slices, counting the number of argon atoms in each slice and averaging it over time. The liquid film thickness can be seen to be decreasing initially. The system attains equilibrium towards the end of the simulation as there is negligible change in the number density profiles confirming the formation of a non-evaporating film.

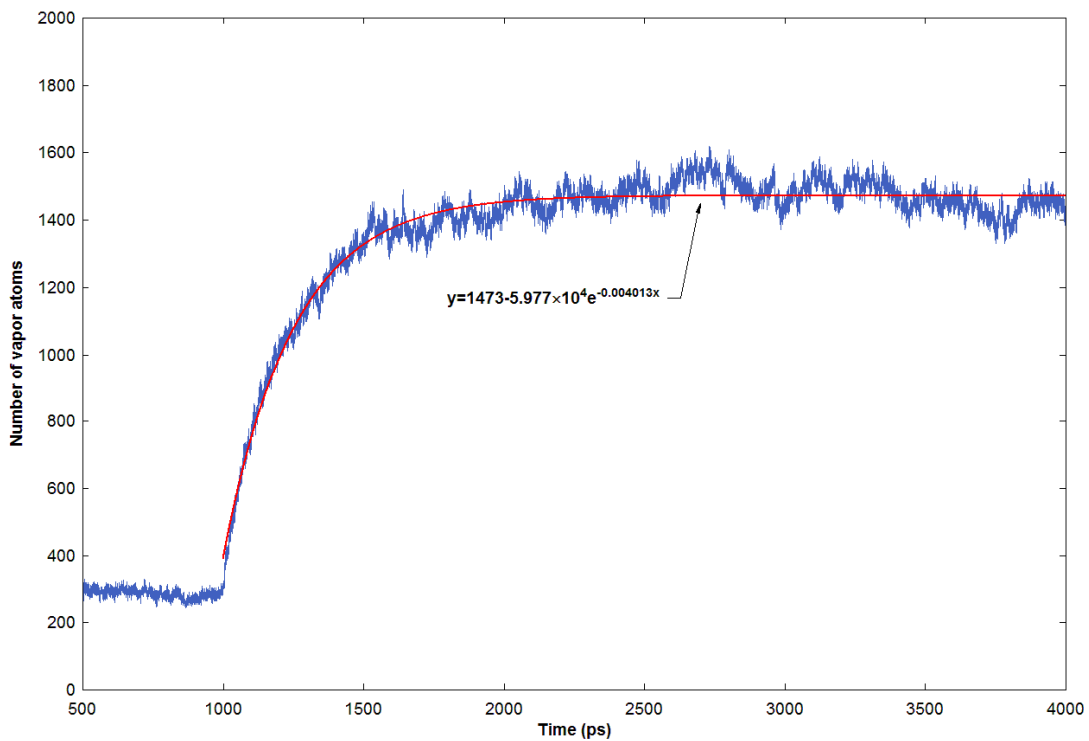


Figure 3-12. Variation of vapor argon atoms with time for case 4

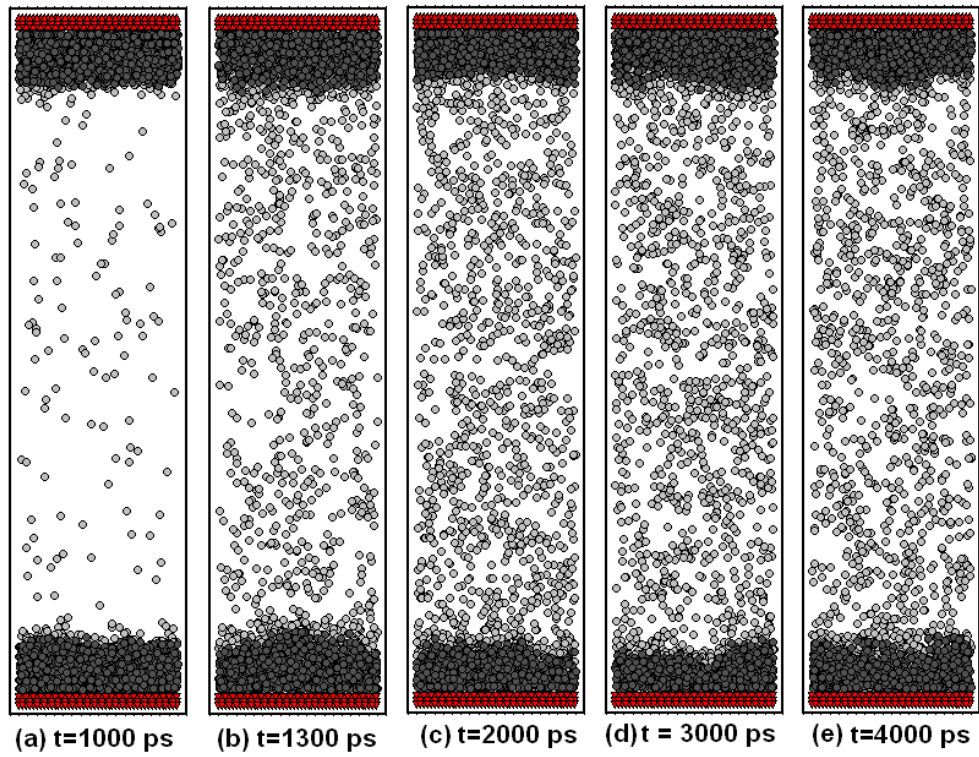


Figure 3-13. Snapshots of domain for case 4

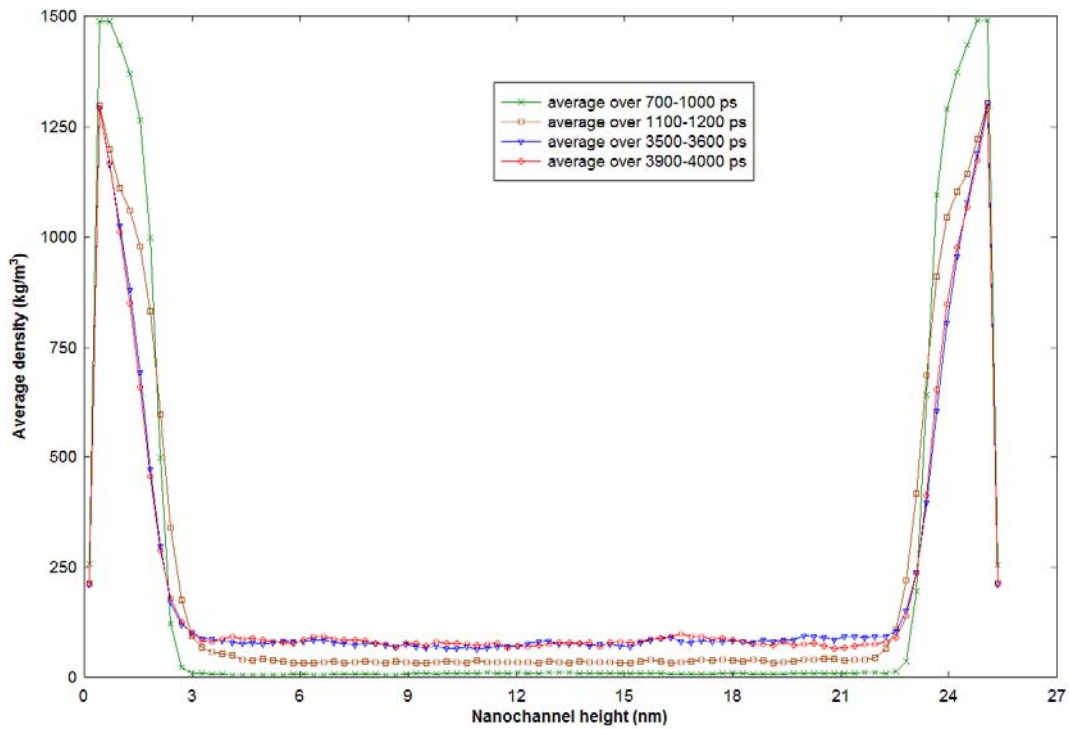


Figure 3-14. Average density of domain at different times for case 4

Heat Flux, Evaporation Flux, Hamaker Constant for Nanochannel

The heat transfer rate and the evaporation rate per unit area are obtained by differentiating the curve fits of energy (Figure 3-11) and number of vapor atoms (Figure 3-12) for each case. The net heat flux and evaporation flux are evaluated by calculating the area under the respective curve fits.

Pressure in vapor region is computed at time intervals of 50 ps using the method verified before. The initial and final vapor pressure is calculated by averaging values from 700-1000 ps and 3000-4000 ps respectively. The liquid film thickness is determined from the density profile at the position where the liquid density begins to decrease. The location of the equimolar surface, obtained from the derivative of density profile, coincides with the extremum of the gradient of the density profile (Mareschal et al., 1997), as is shown in figure 3-15 for case 6. Hamaker constant is evaluated as described in section 3.1.2.

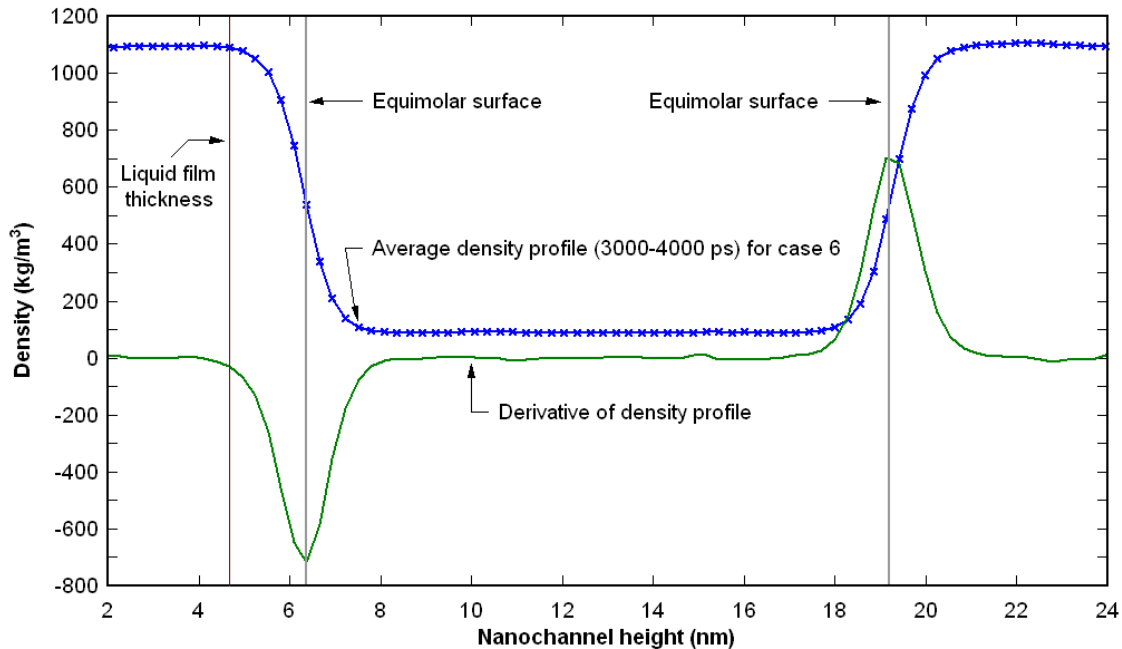


Figure 3-15. Density-height plot showing non-evaporating liquid film thickness and equimolar surface position for case 6

Varying Nanochannel Height h

Figures 3-16 and 3-17 show heat flux rate vs. time and evaporation rate vs. time respectively for varying nanochannel height with constant initial film thickness (cases 1-3). From the figures, it can be seen that nanochannels have the capacity to produce very high heat transfer rates compared to macroscale heat transfer. The highest starting heat transfer rate occurs in the shortest nanochannel (case 1) which is due to the occurrence of high initial evaporation rate – since the channel height is small, the high energy vapor atoms which evaporate from, say, the lower liquid film have greater chances of reaching and striking the upper liquid film in turn causing additional evaporation. Heat flux rate and evaporation rate decrease exponentially with time. The decrease is more prominent in shorter height nanochannels as the vapor space available for evaporation is less. Thus heat transfer and evaporation continues on for a longer time with increasing nanochannel height.

Table 3-2 shows final equilibrium properties, net heat flux and evaporation flux for cases 1-3. The thickness of obtained non-evaporating film decreases with increase in nanochannel height. The interface becomes less spread out with increasing nanochannel height. The final vapor pressures for the three cases are nearly the same, which justifies the calculated Hamaker constants to be similar as it depends on pressure, temperature and solid-fluid interaction. Net heat and evaporation fluxes (area under the curves) increase with increasing nanochannel height, which is as expected.

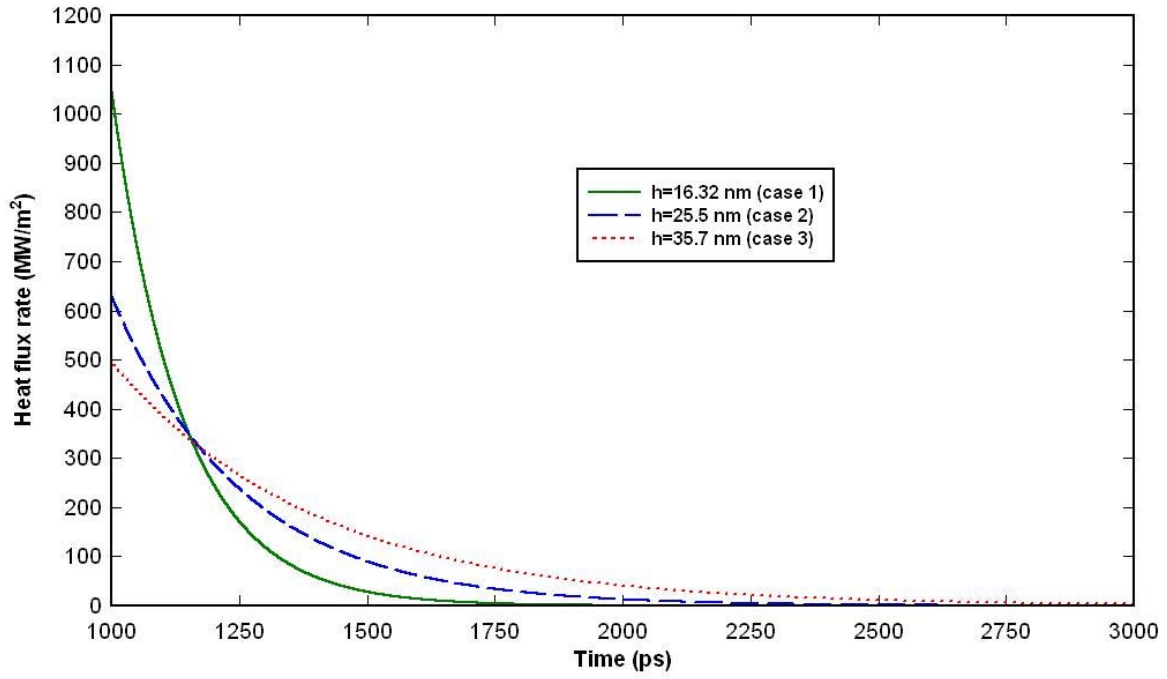


Figure 3-16. Heat flux rate with time for varying nanochannel height (cases 1-3)

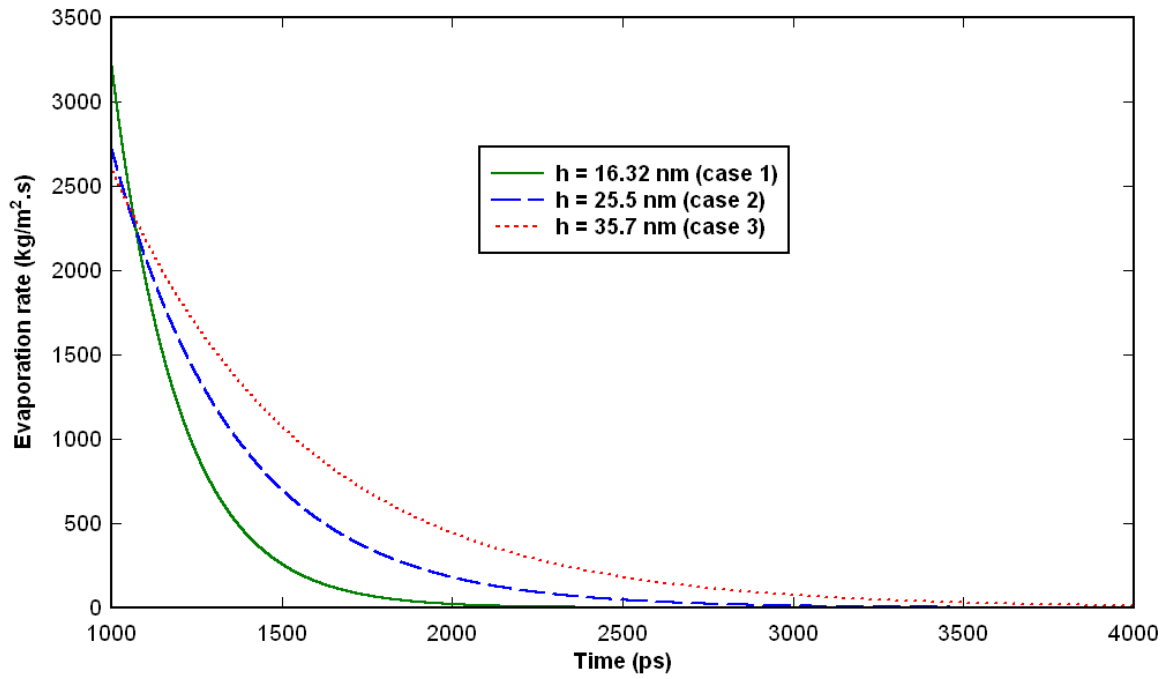


Figure 3-17. Evaporation rate with time for varying nanochannel height (cases 1-3)

Table 3-2. Case 1-3 results for film evaporation in nanochannel

	Non- evaporating film thickness (nm)	Equimolar liquid- vapor position (nm)	Final vapor pressure (MPa)	Net heat flux (J/m ²)	Net evaporation flux (kg/m ²) x 10 ⁻⁶	Hamaker constant A (J) x10 ⁻²⁰
Case 1	1.93	3.412	1.7065	0.1811	0.640086	6.756
Case 2	1.61	2.975	1.7031	0.2154	1.00314	6.614
Case 3	1.57	2.713	1.7574	0.2654	1.46444	6.623

Varying Film Thickness t_{film}

Figures 3-18 and 3-19, respectively, show the heat flux rate vs. time and evaporation rate vs. time for varying initial film thickness with a constant nanochannel height (cases 2, 4-6). The initial evaporation rate, from figure 3-19, is maximum for $t_{\text{film}} = 2$ nm and minimum for $t_{\text{film}} = 5$ nm. This shows that initial evaporation rate is inversely proportional to the thickness of the liquid film as heat has to be transferred across larger number of atoms. Also, compared to figure 3-17, it can be said that thickness of the liquid film plays a more dominant role to higher initial evaporation rate than the height of nanochannel.

The inset of figure 3-18 shows a somewhat odd trend for the initial heat transfer rates. For cases 1-3, discussed above, initial evaporation rate was directly proportional to initial heat transfer rate, but it should also be noted that the number of liquid film atoms were almost same. In the present discussion, the number of liquid atoms vary to a great extent. Thus the thickness of the liquid film also determines how much heat can be initially transferred from the wall to the liquid as more liquid atoms store more energy. This explains why the initial heat transfer rate for $t_{\text{film}}=5$ nm (case 6) > $t_{\text{film}}=4$ nm (case 5) > $t_{\text{film}}=3$ nm (case 2). For $t_{\text{film}}=2$ nm (case 4), the evaporation rate (i.e. heat used up in phase change) is dominant making it have the highest initial heat transfer rate. The evaporation rate and heat flux rate exponentially drop with time, being more prominent for thinner films as they have lesser number of atoms.

Table 3-3 shows final equilibrium properties, net heat flux and evaporation flux for cases 2, 4-6. The thickness of obtained non-evaporating film increases with increasing initial film thickness, and the interface becomes more spread out. The final vapor pressures increase accordingly for cases 2, 4 and 5, which justifies the calculated Hamaker constants to increase as well. It is interesting to note here that for a constant nanochannel height, increasing the thickness of liquid film beyond a certain point does not significantly increase the final vapor pressure as can be seen for cases 5 and 6. Net heat flux increases with increasing film thickness as there are more atoms in the nanochannel to evaporate and/or store energy. Net evaporation flux first increases with t_{film} and then decreases, due to the effect of two competing parameters: total number of liquid atoms and vapor volume in the nanochannel. Thus, to obtain net maximum evaporation flux there is an optimum initial liquid film thickness for any specific height of nanochannel.

Table 3-3. Case 2, 4-6 results for film evaporation in nanochannel

	Non- evaporating film thickness (nm)	Equimolar liquid- vapor position (nm)	Final vapor pressure (MPa)	Total heat flux (J/m ²)	Total evaporation flux (kg/m ²) x 10 ⁻⁶	Hamaker constant A (J) x10 ⁻²⁰
Case 4	0.99	2.125	1.6122	0.163	0.966156	5.229
Case 2	1.61	3.258	1.6798	0.215	1.00314	6.613
Case 5	2.97	4.392	1.7490	0.266	0.956312	7.023
Case 6	4.67	5.525	1.7525	0.321	0.846324	7.026

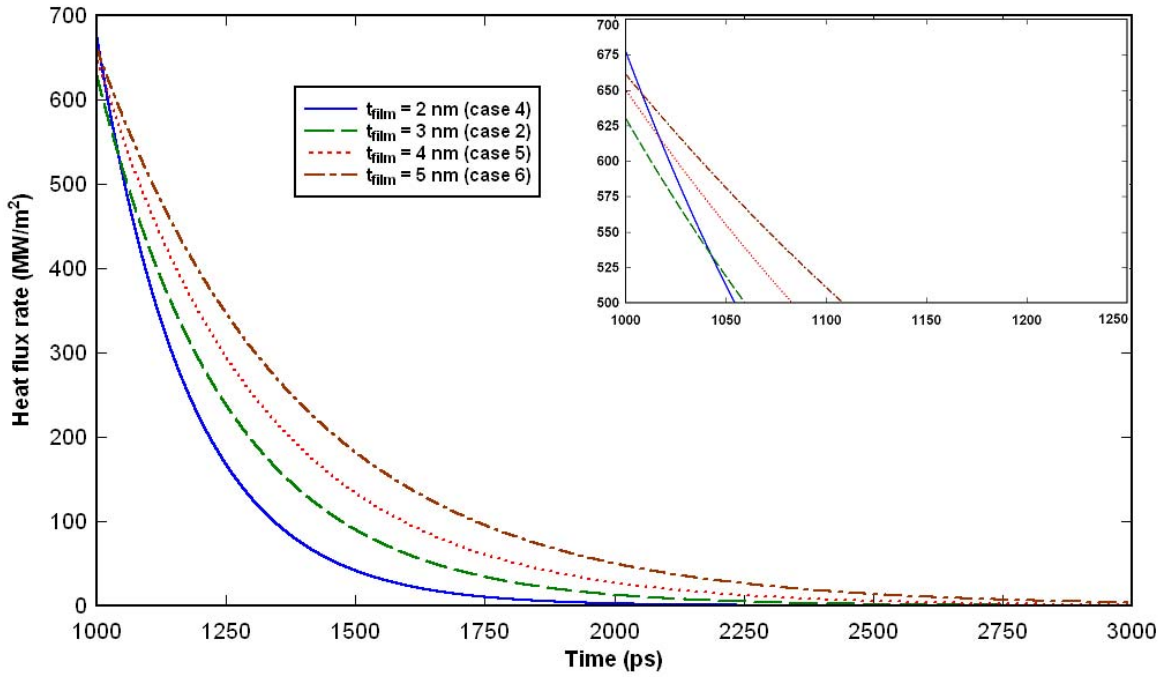


Figure 3-18. Heat flux rate with time for varying film thickness (cases 2, 4-6)

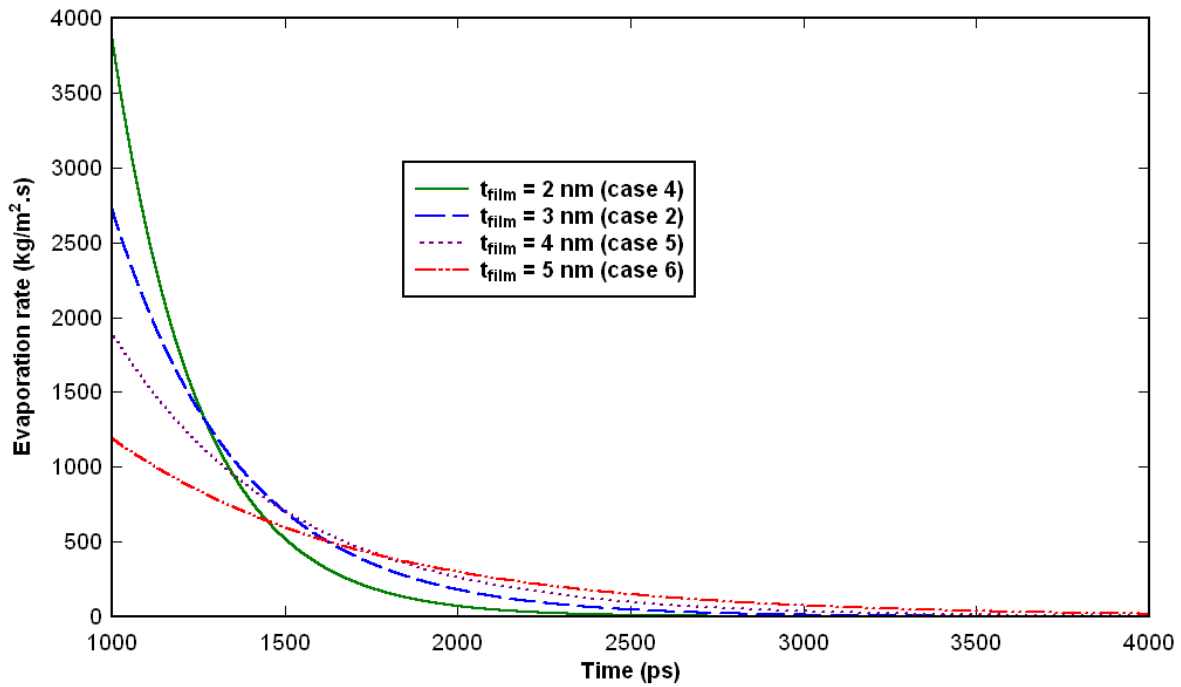


Figure 3-19. Evaporation rate with time for varying film thickness (cases 2, 4-6)

Vapor Pressure-Density Plots

The average initial and final vapor pressures and vapor densities were evaluated for the simulation runs for all six cases (1-6). Vapor pressure vs. vapor density for initial and final state is plotted for varying nanochannel height (cases 1-3) in figure 3-20, and for varying film thickness t_{film} (cases 2, 4-6) in figure 3-21. The plots show that the states lie on the saturation curve, which is obtained from thermodynamics table of argon, implying that the vapor is saturated. This further validates the existence of the non-evaporating thin film in all six cases (1-6) as the final vapor condition is saturated and thus no additional evaporation from the film can occur. The vapor cannot increase beyond saturation values in this work since the only mode of evaporation is from the thin film which becomes non-evaporating after a certain time period. Since there is no other physical process occurring in the system to add more vapor atoms, the vapor pressure remains saturated. This defines the limiting condition for the formation of the non-evaporating thin film at the three-phase contact line for a particular combination of vapor pressure, substrate temperature and solid-liquid interaction. It should be noted that the evaporating thin film region of the three-phase contact line has a curved interface, unlike the non-evaporating film which has a flat interface. The Young-Laplace equation states

$$P_v - P_l = 2\sigma/r \quad (P_v\text{-vapor pressure, } P_l\text{-liquid pressure, } \sigma\text{-surface tension, } r\text{-radius of curvature}).$$

For the evaporating thin film region which has a curvature $P_v > P_l$. If the pressure and temperature in the liquid and vapor are (P_l, T_l) and (P_v, T_l) respectively (liquid and vapor are in thermal equilibrium) and the vapor phase is in a saturated state, the vapor pressure on a curved interface at equilibrium is given by⁵ $P_v = P_{sat}(T_l) \exp(-2\nu_l\sigma/rRT_l)$, where P_{sat} is the saturation pressure corresponding to T_l on a flat surface. Thus, $P_v < P_{sat}$, which implies that curvature of the interface lowers the vapor pressure compared with that above a planar interface for the same

liquid temperature²⁵. It follows from above that $P_l < P_{sat}$. This implies that for a curved interface, the liquid is superheated relative to the normal saturation state for a flat interface which explains the evaporation in the curved liquid meniscus region. In addition, evaporation also continues to occur from the evaporating thin film region as liquid is continuously supplied to this region from the intrinsic meniscus region to replace the evaporated liquid. This increases the vapor pressure further restricting the possibility of any kind of evaporation from the non-evaporating region.

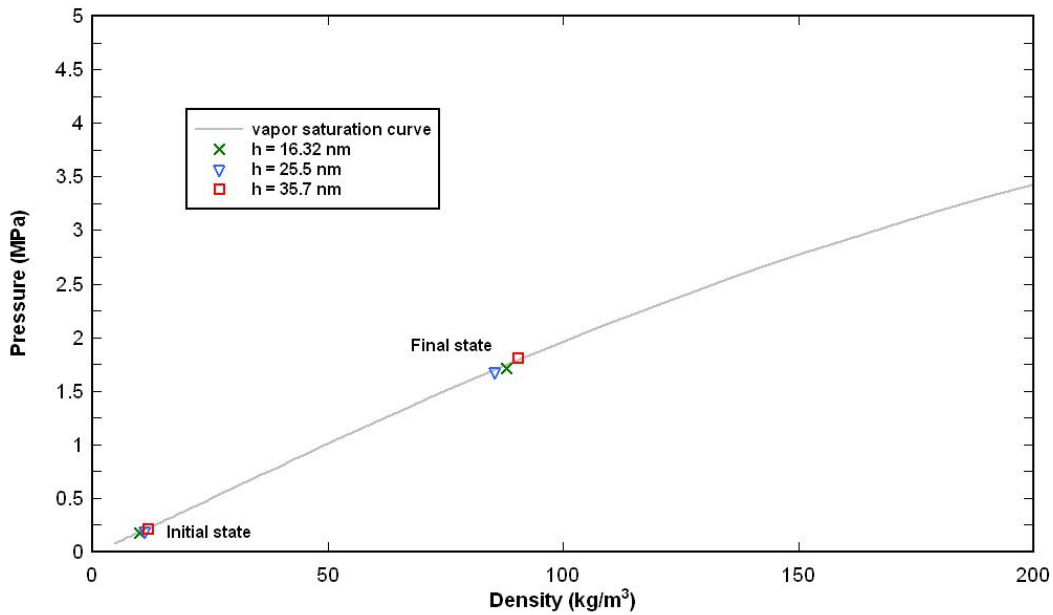


Figure 3-20. Pressure-density plot of initial and final states for varying nanochannel height (cases 1-3)

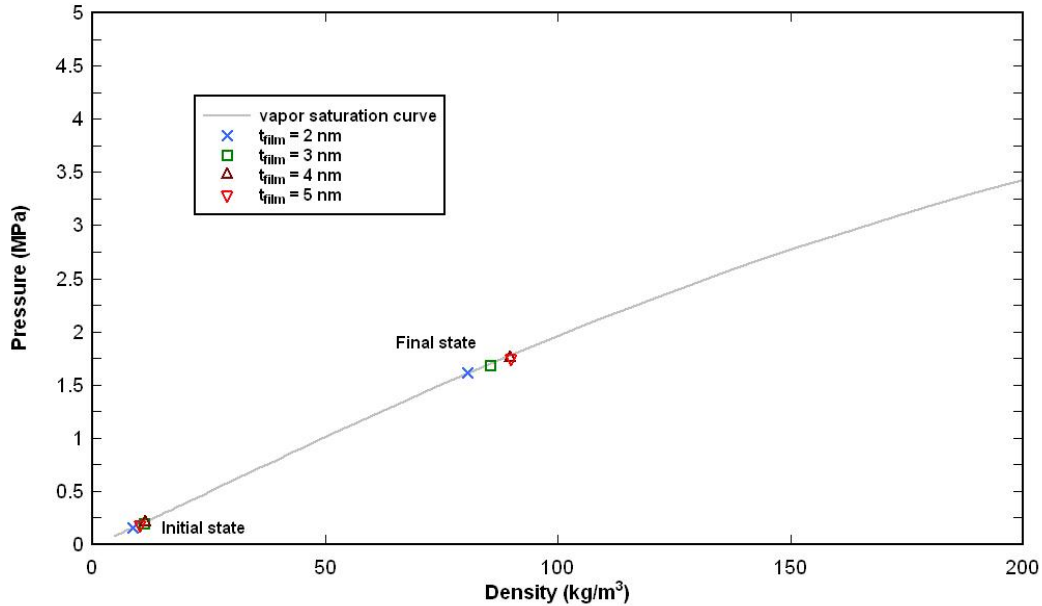


Figure 3-21. Pressure-density plot of initial and final states for varying film thickness (cases 2, 4-6)

Case 7 – Simultaneous Evaporation and Condensation

It has been widely speculated in literature that wall-fluid molecular interaction is the dominant factor for the formation of a non-evaporating film, the other parameters being pressure and temperature. In each of the cases (1-6) studied so far, a non-evaporating film was obtained. Wall-fluid interaction and wall temperatures were the same, with evaporation occurring from both walls. The dependence of Hamaker constant of the non-evaporating film on vapor pressure was shown. It is easy to visualize the effect of nominal increase in temperature of the wall which will lead to more energy imparted to atoms, more evaporation and hence thinner non-evaporating films, if at all they have to form. Thus, case 7 studies as to how important wall-fluid molecular interaction is to the formation of non-evaporating film. Similar to case 2, two thin films each of thickness 3 nm is placed on upper and lower walls in a nanochannel of dimensions $6.117 \text{ nm} \times 6.117 \text{ nm} \times 25.5 \text{ nm}$. In this case, only the upper wall temperature is increased to 130 K

while the lower wall temperature is kept the same as the initial domain temperature of 90 K. Figure 3-22 shows the variation of vapor pressure with time. The vapor pressure increases when evaporation is dominant and then decreases as more condensation occurs. Figure 3-23 shows the snapshots of the domain during the evaporation-condensation process. Non-evaporating film is not obtained on the upper wall even though the wall is at the same temperature of cases 1-6. Wall-liquid molecular interaction is important to the extent that it determines the strength with which the solid molecules attract liquid molecules i.e. governs wettability. But this case shows that pressure is the dominant factor for the formation of non-evaporating films. In other words, for a certain wall-liquid pair, non-evaporating film will form or not form depending on the vapor pressure of the domain and the temperature of the wall.

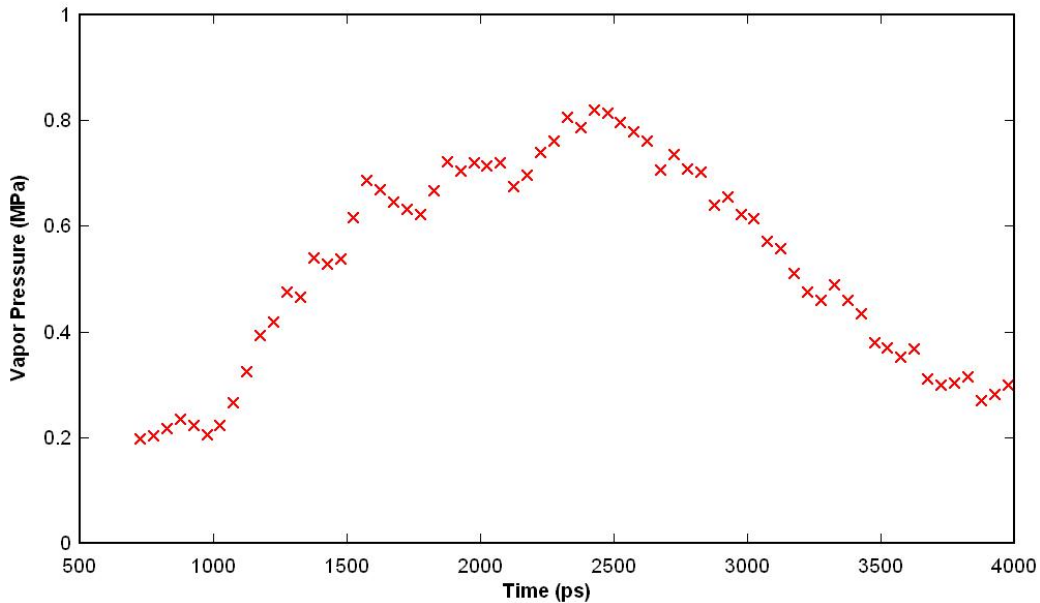


Figure 3-22. Vapor pressure variation with time for case 7

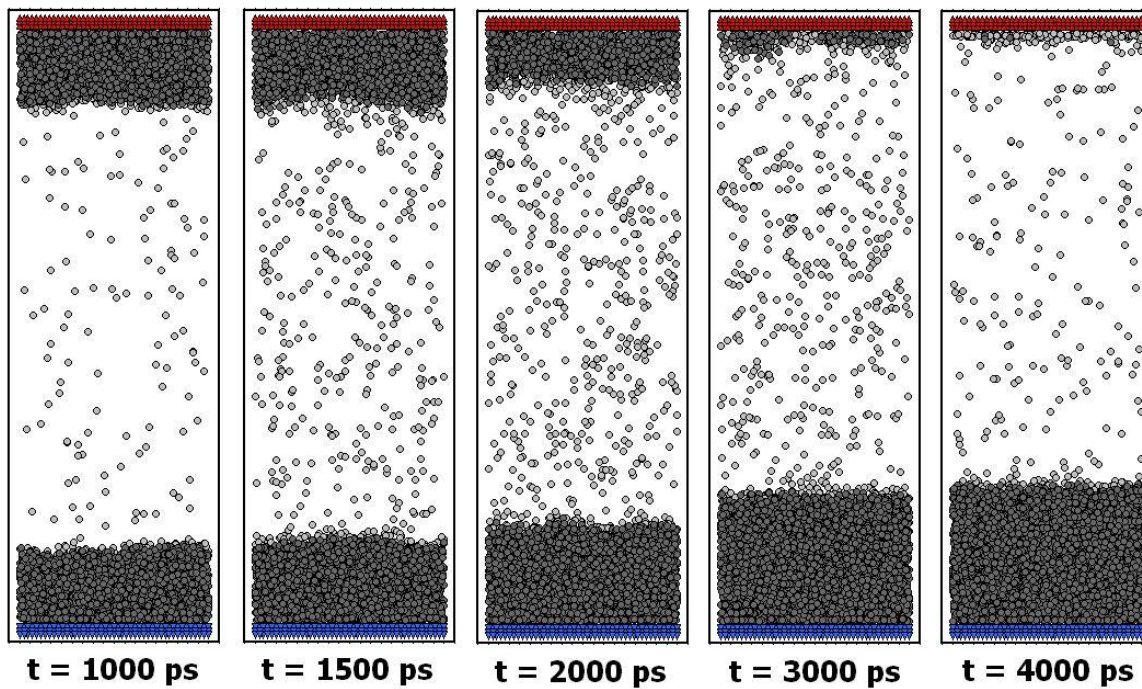


Figure 3-23. Snapshots of domain at different time intervals for case 7

CHAPTER 4 NANO-DROPLET IMPACT ON A HOMOGENEOUS SURFACE

Impact of argon nano-droplet on homogeneous platinum wall is simulated using molecular dynamics. Wall temperature (90 K, 300 K) and surface wettability (high, low based on ϵ_{Ar-Pt} parameter) are varied to study four cases. An external force is applied on the drop for a short time period to achieve velocities in the range of 13 m/s – 15 m/s.

The simulation domain is a cuboid of dimensions 15.721 nm×15.721 nm×13.936 nm. A liquid droplet, initially in the form of a cube of side 6.2 nm, is placed in the domain with the drop center at $z=8.455$ nm. The remaining volume is occupied by argon vapor. Both liquid and vapor are initially at their respective saturation states at 90 K. The simulation domain initially comprises of 4913 liquid droplet argon atoms, 315 argon vapor atoms and 11229 Pt atoms. The time step is 5 fs.

The argon atoms are subjected to six boundaries, two in each of the x, y and z directions. The boundaries in the x and y directions are periodic throughout the simulation. The simulation starts off with a velocity-scaling period (0-500 ps) followed by the equilibration period (500-1000 ps). The force-application period follows the equilibration period where a constant external force of magnitude 3.5083×10^{-15} N is applied to each liquid drop atom in the negative z direction during the time period of 1000-1301.275 ps in order to attain a final drop velocity in the range of 13 m/s to 15 m/s. The boundaries in the z-direction were also periodic in nature so far.

At the end of the force-application period, the periodic boundary conditions in the z-direction are removed and the Pt wall is inserted into the simulation at the desired temperature. Now, the mirror boundary condition is applied at the upper boundary, while the lower boundary in the z-direction becomes the Pt wall. The simulation is continued to run till 3000 ps.

Maruyama and Kimura (2000) concluded from their work that the wettability of the surface can be change by varying the ε_{Ar-Pt} parameter in the L-J potenatial. Making use of this fact, droplet impact is studied for high and low wettable surfaces with variation in wall temperature. Four cases which are looked upon in this work are:

Case 1: Wall temperature at 90 K and $\varepsilon_{Ar-Pt} = 0.894 \times 10^{-21} J$

Case 2: Wall temperature at 90 K and $\varepsilon_{Ar-Pt} = 0.3576 \times 10^{-21} J$

Case 3: Wall temperature at 300 K and $\varepsilon_{Ar-Pt} = 0.894 \times 10^{-21} J$

Case 4: Wall temperature at 300 K and $\varepsilon_{Ar-Pt} = 0.3576 \times 10^{-21} J$

Evaluation of Drop Temperature

At each time step, the total number of liquid atoms, N , constituting the drop can be found out. The drop temperature is determined using the following equations, also used by Hanasaki et al. (2004):

$$T_x^* = \sum_{i=1}^N v_{x,i}^2 \quad (4.1)$$

$$T_y^* = \sum_{i=1}^N v_{y,i}^2 \quad (4.2)$$

$$T_z^* = \left[\sum_{i=1}^N v_{z,i}^2 \right] - \langle v_{z,i} \rangle^2 \quad (4.3)$$

$$T^* = \frac{1}{3N} (T_x^* + T_y^* + T_z^*) \quad (4.4)$$

Evaluation of Interface Markers, Interfacial Fit and Contact Angle

The contact angle which the drop makes with the Pt wall is determined in 2D in the x-z plane. The drop is divided into squares of dimension $1 \sigma_{Ar-Ar} \times 1 \sigma_{Ar-Ar}$ and the number of atoms in each square are determined. Once all the atoms are allotted to their squares, the average

number density is found out. The square with the maximum number of atoms is determined and a check is performed from this square in the outward direction such that if the number of atoms in a square falls below 0.5 times the average number density, an interface marker is placed at the center of that square. Thus, interface markers are placed around the drop using this procedure. After all interface markers are determined, an elliptical fit of nature $\alpha(x-x_c)^2 + \beta(z-z_c)^2 = 1$ is used to fit all the markers such that $R^2 \geq 0.999$, where x_c and z_c are the x,z co-ordinates of center of mass of the drop. The contact angle is the angle made by the tangent to the elliptical fit at the point where it intersects with the wall i.e. $z=0$. The contact angle is evaluated in time intervals of 5 ps.

Droplet Impingement – Case 1

Figure 4-1 shows the variation of average drop temperature and energy with time. The drop temperature fluctuates about a mean value of 89.13 K and the drop mean energy is -0.03035 eV/atom, during the equilibration period. The average drop temperature and energy evaluated in the final 1000 ps is 89.95 K and -0.02498 eV/atom respectively. Figure 4-2 shows the drop z-velocity curve and the center of drop position with time. The drop attains a velocity of -13.69 m/s at the end of the force-application period and travels at that velocity for a short time period. When the drop reaches within a distance r_c from the wall, the long range attractive force from the wall atoms act of the drop atoms and thus increase the velocity of the drop. The average velocity of the drop on impact is - 26.63 m/s. The increase in the velocity depends on the size of the drop since in larger-sized drops; only the atoms at the lower end of the drop are influenced by the wall atoms and the majority of the atoms forming the drop do not interact with the wall during impact. Thus the wettability of the wall is found to be significant in determining the actual impact velocity of nano-sized drops.

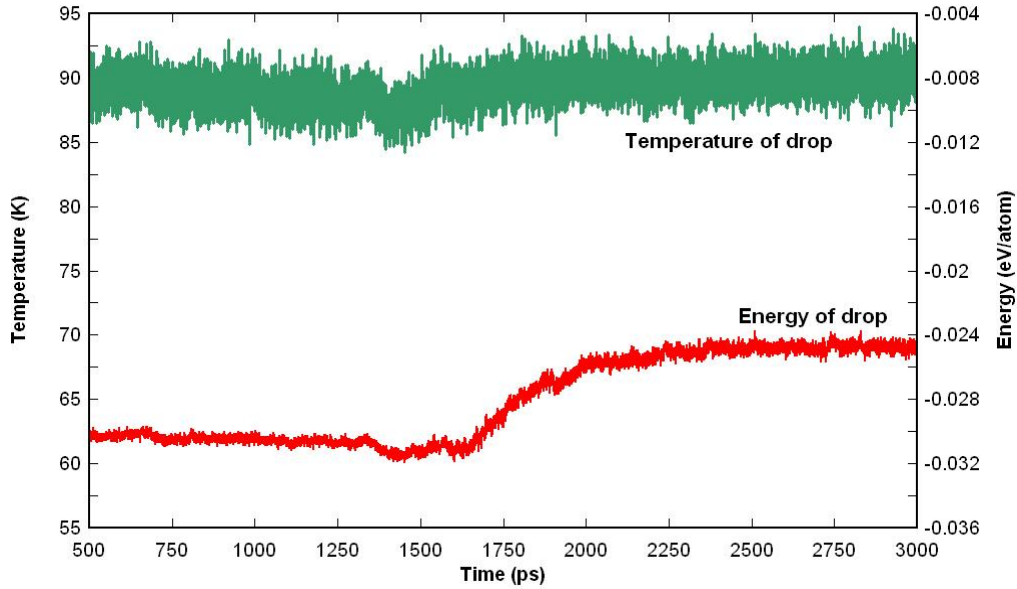


Figure 4-1. Variation of drop temperature and energy with time for drop impact (case 1)

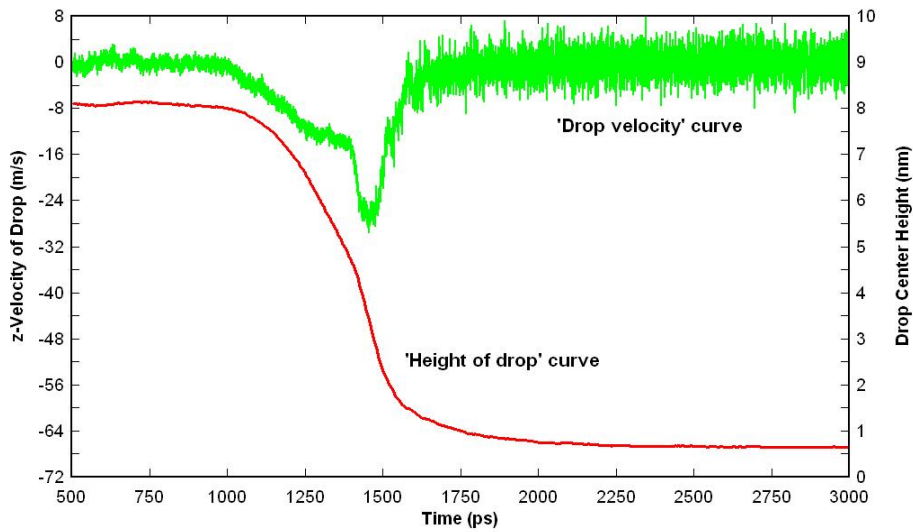


Figure 4-2. Variation of drop-center height and drop velocity with time for drop impact (case 1)

Figure 4-3 shows the snapshots of the x-z plane of the simulation at different timesteps. The interface markers, interfacial fit and the contact angle values are shown in the snapshots. It can be seen that due to the high wettability of the wall, the drop spreads completely on impact.

Please note that the wall is not actually present in Figure 4-3a (wall has not been inserted yet) and is just shown for convenience.

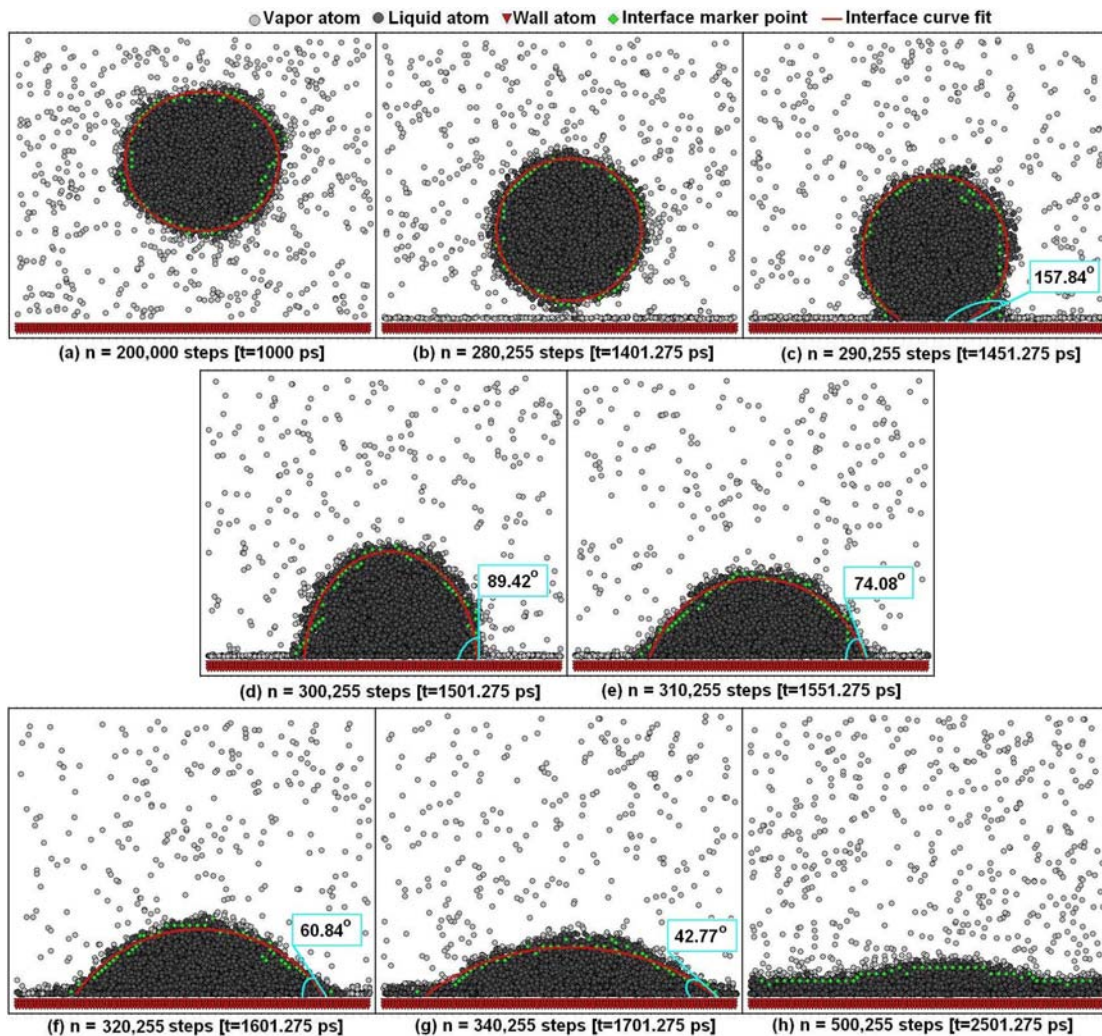


Figure 4-3. Snapshots of x-z plane for drop impact (case 1)

Figure 4-4 shows the variation of contact angle with time during impact and spreading. The drop impacts on the wall at about 1445 ps and the contact angle decreases as the drop spreads. As the spreading edge of the drop reaches x and y boundaries, the edges interact with each other due to the periodic nature of the boundaries thus causing rapid spreading and formation of a thin film. This physically signifies the drop merging with four other identical drops. The contact angle becomes zero once the film forms. A larger computational domain

needs to be used to notice complete individual droplet spreading (it was not used in this current work due to computational restrictions).

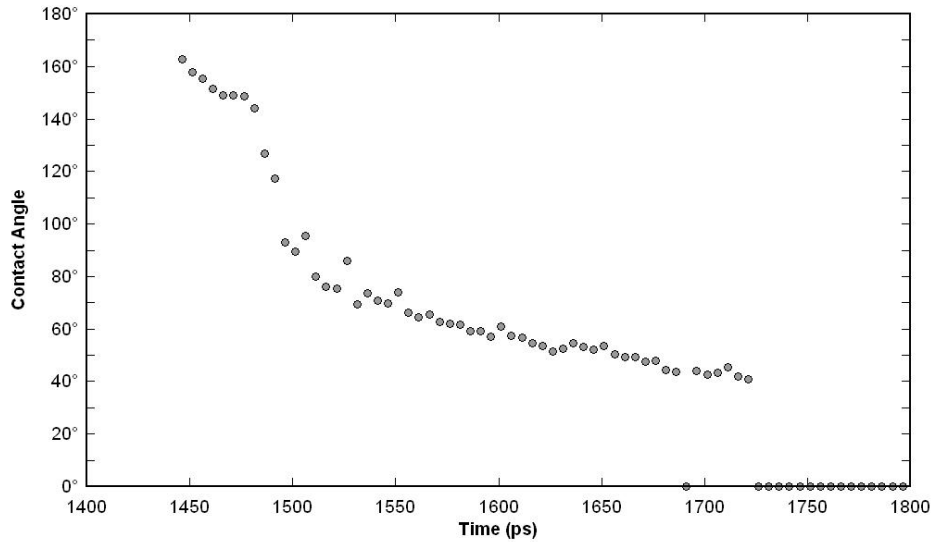


Figure 4-4. Variation of contact angle with time for drop impact (case 1)

Droplet Impingement – Case 2

Figure 4-5 shows the snapshots of x-z plane at different timesteps. Figure 4-6 shows the variation of drop velocity and drop center height with time for the less wettable surface. The drop achieves a z-velocity of -13.64 m/s at the end of force-application period. Similar to case 1, the average drop velocity increases lower end of the drop comes in the long attractive force of wall atoms and the actual velocity during impact is -19.49 m/s, which is less than that obtained in case 1 as the wettability is lower in this case. The drop impacts on the wall at about 1465 ps.

It can be seen that the drop does not spread on this less-wettable surface. The drop center height in figure 4-6 is seen to oscillate thus showing that the drop oscillates on a non-spreading surface after impact, and the contact angle varies. The plot of contact angle with time (Figure 4-7) confirms the fact. The mean value of the contact angle during the final 500 ps is 126.7° . The curve fit for drop oscillation is shown from 2500-3000 ps.

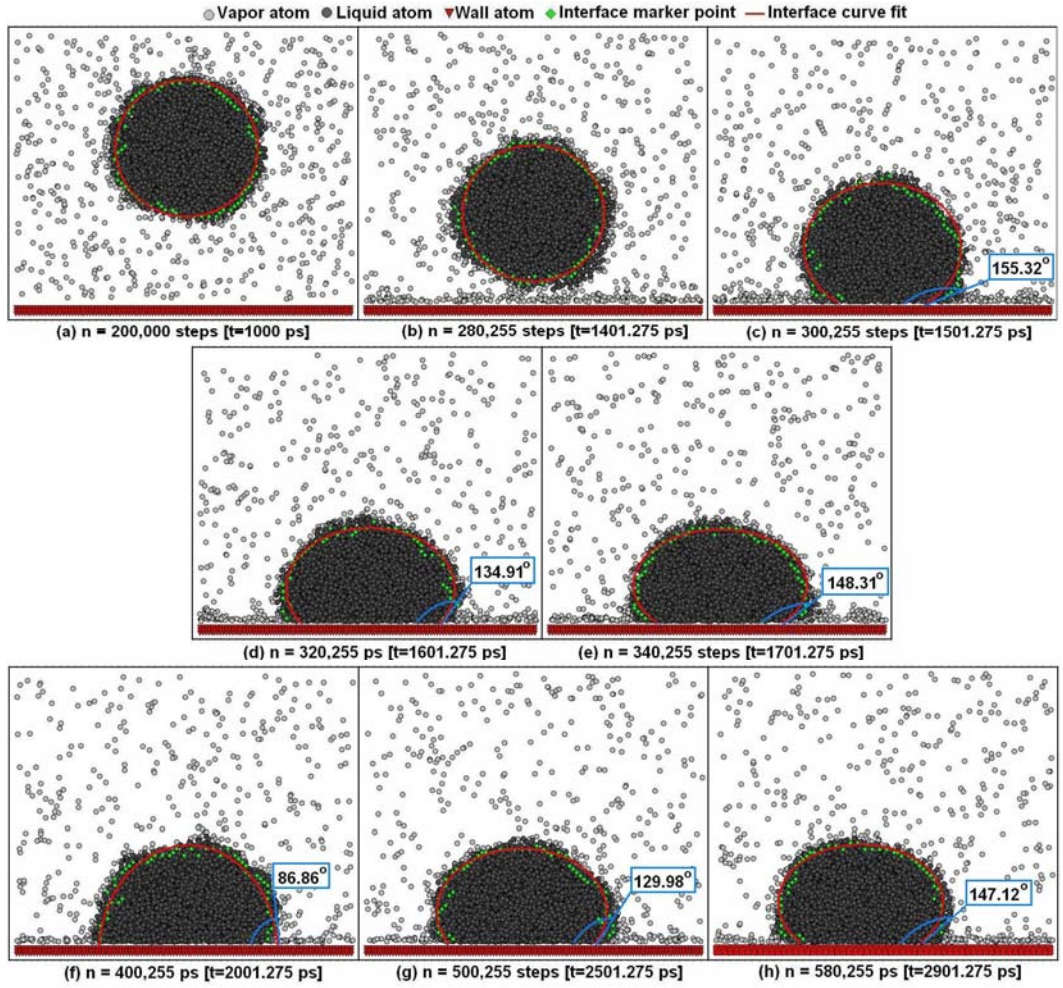


Figure 4-5. Snapshots of x-z plane for drop impact (case 2)

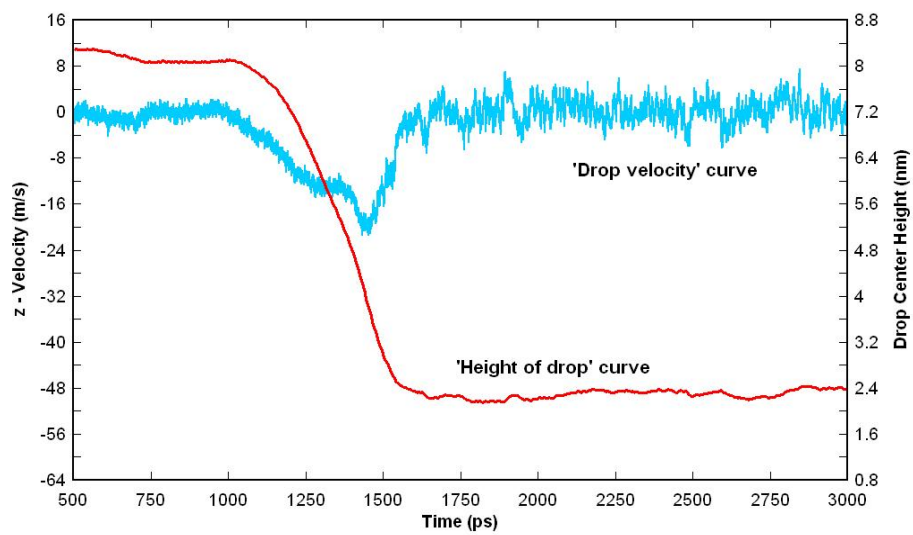


Figure 4-6. Variation of drop center height and drop velocity with time for drop impact (case 2)

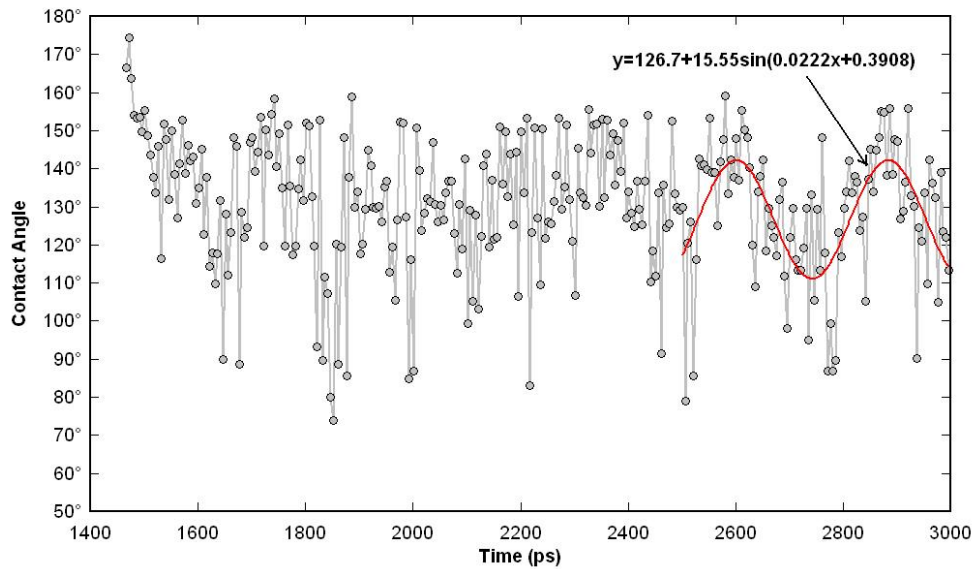


Figure 4-7. Variation of contact angle with time for drop impact (case 2)

Droplet Impingement – Case 3 and Case 4

Figures 4-8 and 4-9 show the snapshots of the y-z plane for case 3 and case 4 respectively. For the high-wettability surface (Figure 4-8), leidenfrost effect is observed and a layer of vapor is formed as soon as the drop impacts on the wall which is at 300 K. It can be seen that the drop does not actually touch the wall (unlike case 1 and case 2) but rests on the vapor layer throughout the evaporation process. Complete drop evaporation is obtained. For the low-wettability surface (Figure 4-9), the leidenfrost effect is again observed but to a greater extent as the vapor layer which forms during impact pushes the drop away from the wall. Due to the low attraction from the wall atoms, the drop does not hold to the surface as was seen in case 3. The temperature of the drop increases only for the time period it is in contact with the wall. Thus, the evaporation rate significantly reduces for low wettable surfaces. The interface markers are not evaluated for these cases since evaluation of contact angle becomes irrelevant. The light colored circles represent vapor atoms and the dark colored circles represent liquid atoms.

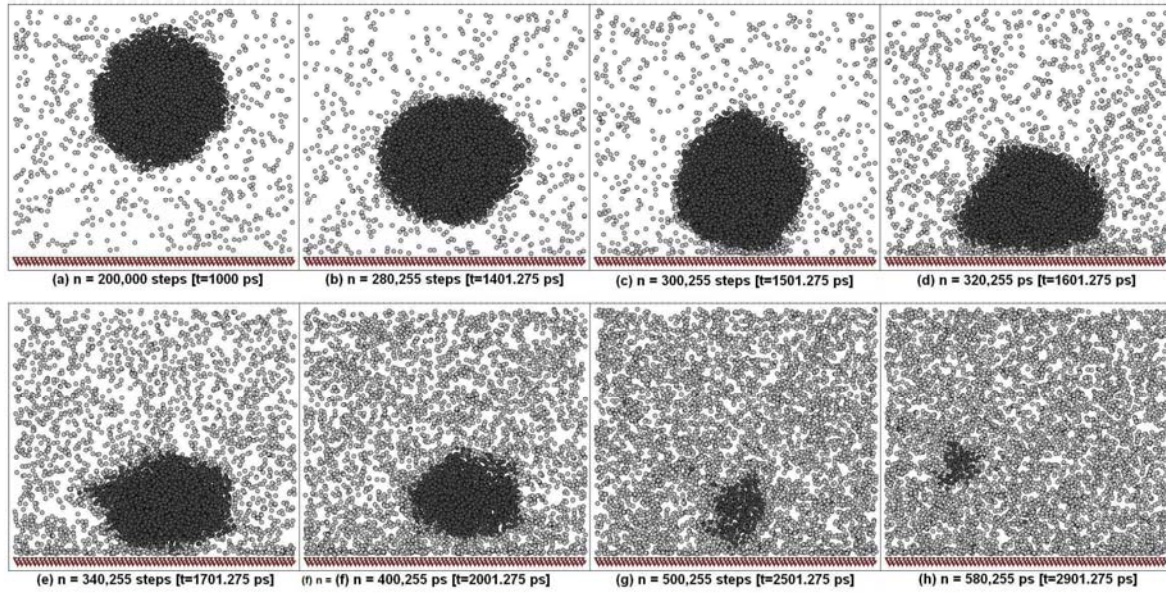


Figure 4-8. Snapshots of y-z plane for drop impact (case 3)

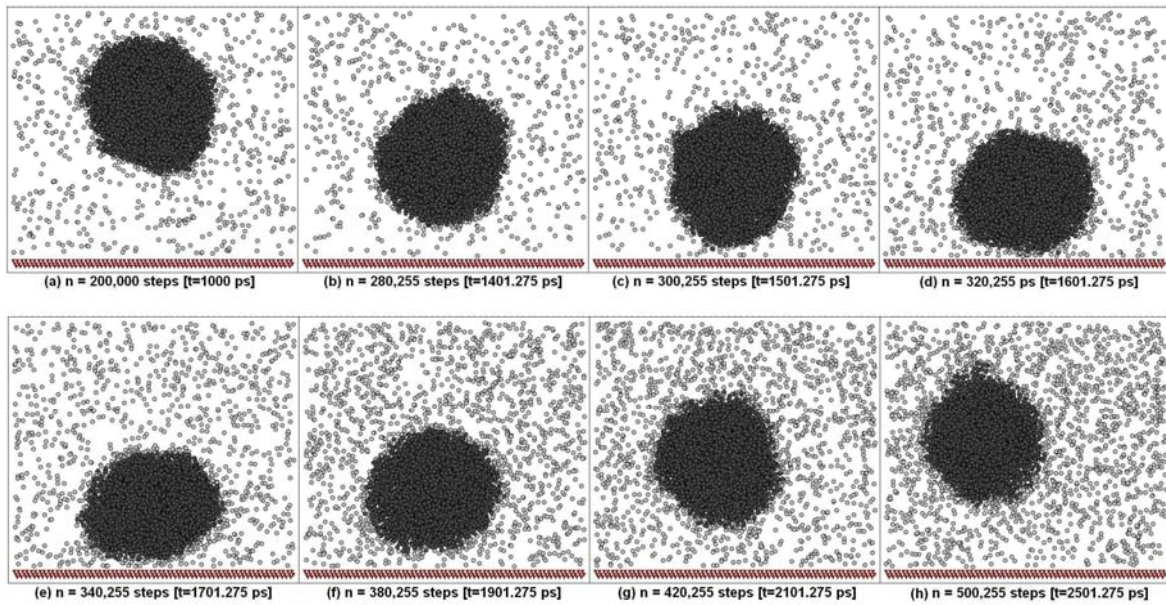


Figure 4-9. Snapshots of y-z plane for drop impact (case 4)

CHAPTER 5 MENISCUS EVAPORATION AT NANOSCALE

The moving contact line is a three-phase phenomenon where vapor-liquid interface meets the solid surface. It has been widely accepted in literature that the contact line at the base of a bubble in nucleate boiling can be divided into three regions: non-evaporating thin-film region, evaporating thin-film region and intrinsic meniscus region. Thus nucleate boiling is a multi-scale problem. The non-evaporating region is of the order of nanometers, and no mass/heat transfer from it. Maximum evaporation and heat transfer occurs from the evaporating thin-film region and the liquid is fed from the bulk liquid through the intrinsic meniscus region. There is a region, called the interline region, between the non-evaporating thin film region and the evaporation thin film region over which the film varies in thickness and curvature to accommodate the transition between the two regions. This is the thinnest portion of the meniscus over which vaporization can occur, and since it is the thinnest, it is also the location where the evaporation rate is the highest (Carey 1992). The thin-film regions are also characterized by capillary and disjoining pressures. Researchers have studied the heat transfer characteristics in the thin-film region analytically and experimentally. However, measuring properties at nanoscale is still a challenge and experiments conducted were on micro- to milli-meter scale. Since the thin-film region starts off at nanoscale, it would be more befitting to use molecular dynamics to study the non-evaporating and interline region in a nanoscale meniscus.

Simulation Model

A concave meniscus was formed by placing liquid argon between a lower wall and an upper wall, with an opening in the upper wall as shown in Figs. 5-1 and 5-2. The walls are made of three layers of platinum (Pt) atoms arranged in fcc (111) structure. The space above the meniscus is occupied by argon vapor. The domain consists of a total of 14172 argon atoms and

7776 platinum atoms. The total width, height and depth are 34 nm, 59.5 nm and 4.3 nm respectively. The length of the opening in the upper wall is 28.22 nm. The separation between the lower wall and the upper wall is 6.2 nm. The initial equilibrium temperature is 90 K. The time step is 5 fs. The atomic interaction is governed by the modified Lennard-Jones potential. The cutoff radius is set as $r_{cut} = 4\sigma_{Ar-Ar}$.

All the boundaries in x and y directions are periodic. The length of the boundary above the upper wall in the x-direction is restricted to the width of the opening. Any argon atom which goes above the upper wall does not interact with the wall atoms anymore. The top boundary in the z-direction is the mirror boundary condition where the argon atom is reflected back in the domain without any loss of energy or momentum i.e. the boundary is adiabatic and elastic in nature. The ‘fluid-wall thermal equilibrium model’ is used to numerically simulate heat transfer between wall and fluid atoms. Equations and parameters implemented are non-dimensional (Rapaport 1995). The algorithm used to calculate the atomic force interactions is the linked-cell algorithm which is a cell-based method and involves data organization (Allen and Tildesley 1987). The integrator method used here is the Velocity-Verlet method (Sadus 1999). Two cases are simulated in this work:

Case I: After the equilibrium period, the temperature of platinum wall underneath the opening (shown in red color in Fig. 2) is changed to 130 K while the rest of the wall (shown in blue color in Fig. 2) is kept at same initial temperature of 90 K.

Case II: After the equilibrium period, the temperatures of all walls are changed to 130 K.

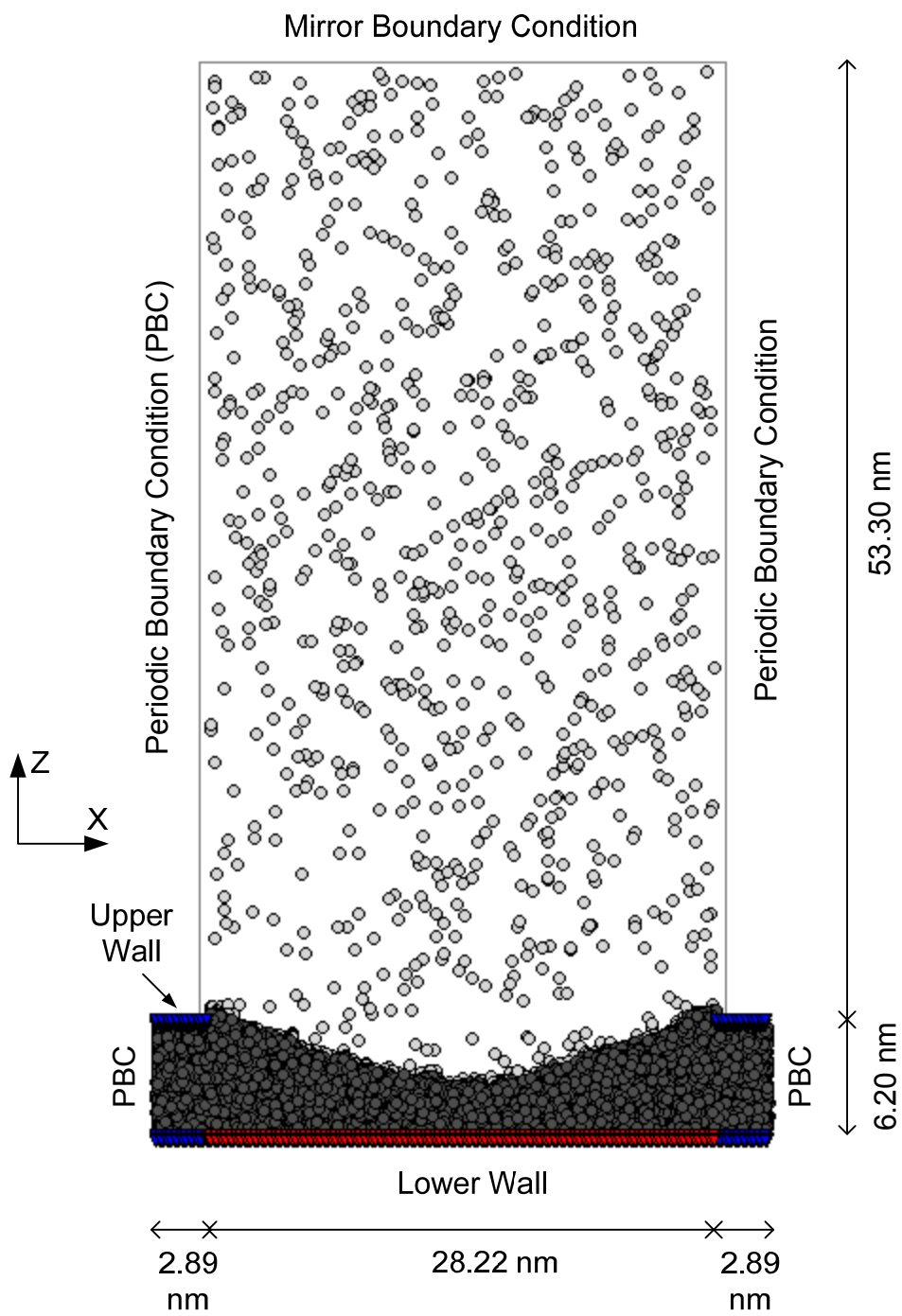


Figure 5-1. Schematic showing configuration of the computational domain

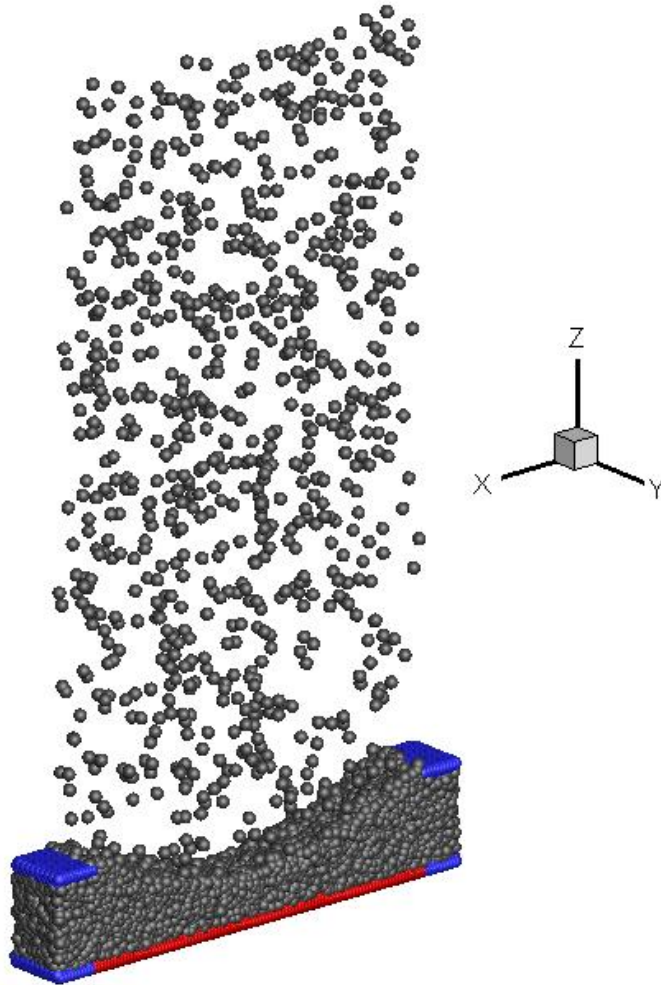


Figure 5-2. 3D schematic of the computational domain

Liquid atoms are distinguished from vapor atoms based on the minimum number of neighboring atoms within a certain radius, as discussed earlier. For argon at 90 K, the threshold number density was obtained as 7 and threshold radius as 0.53 nm i.e. if an argon atom has 7 or more neighboring atoms within a radius of 0.53 nm it is said to be a “liquid” atom or else a “vapor” atom.

As discussed earlier, the Hamaker constant for non-evaporating films is obtained from molecular dynamics simulations. Starting from the Lennard-Jones potential, which is the model of interaction between Ar-Pt, the following equation is derived:

$$U_{LJ}(z) = -\frac{A}{12\pi} \left[\frac{1}{d^2} - \frac{1}{(z)^2} - \frac{\sigma_{Ar-Pt}^6}{30d^8} + \frac{\sigma_{Ar-Pt}^6}{30(z)^8} \right] \quad (5.1)$$

where, A is a Hamaker-constant parameter, d is the gap between Ar and Pt slabs, z is the total thickness of Ar slab (including the gap thickness) and U_{LJ} is the total interaction energy between Ar-Pt slabs from molecular dynamics using LJ potential. This equation was used to calculate the Hamaker constant for non-evaporating film with varying pressure and temperature earlier, and an average value of $A = 6.13 \times 10^{-20}$ J is used in this work. The disjoining pressure is calculated as:

$$P_d = -\frac{dU_{LJ}(z)}{dz} = \frac{A}{12\pi} \left[\frac{2}{(z)^3} - \frac{8\sigma_{Ar-Pt}^6}{30(z)^9} \right] \quad (5.2)$$

The capillary pressure is the product of interfacial curvature K and surface tension coefficient σ as follows:

$$P_c = \sigma K, \quad K = \delta'' (1 + \delta'^2)^{-1.5} \quad (5.3)$$

where δ' and δ'' are, respectively, the first and second derivatives of thickness with respect to length x . The variation of meniscus thickness is determined in 2D in the x - z plane. The meniscus, formed from liquid argon atoms, is divided into square bins of dimension $1 \sigma_{Ar-Ar} \times 1 \sigma_{Ar-Ar}$ and the number of atoms in each square are determined. Once all the atoms are allotted to their squares, the average number density is found out. A check is performed from the Pt wall in the positive z -direction such that if the number of atoms in a bin falls below 0.5 times the average number density, an interface marker is placed at the center of that bin. Thus, interface markers are placed at the meniscus interface using this procedure. A fourth-order polynomial fit of the interface markers is used to obtain the function $\delta(x)$.

The evaporating meniscus, formed of liquid atoms, is divided into 10 equal 'regions' as shown in Fig. 5-3 along the x -direction. Regions 0 and 11 are denoted for nanochannel region.

The length of each region is 2.822 nm. The number of liquid atoms, along with the average temperature and energy of each region is tracked over time.

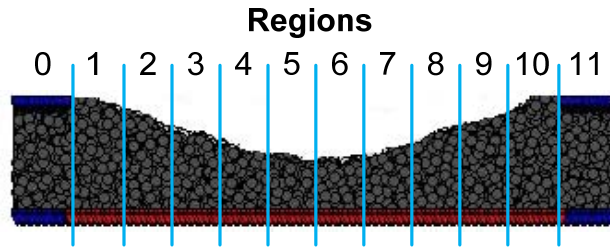


Figure 5-3. Schematic depicting division of nanochannels and liquid meniscus into 11 regions

Consider a liquid nano-meniscus on a surface surrounded by vapor, similar to this work, as shown in Fig. 5-4. The meniscus is divided into two regions, A and B, with equal surface area. At time t_1 , as shown in Fig. 5-4a, region A of the liquid meniscus has a total of N_{1a} atoms with an average energy of E_{1a} . Similarly, region B of the liquid meniscus has a total of N_{1b} atoms with an average energy of E_{1b} . The vapor region above the meniscus has N_{1v} atoms with an average energy of E_{1v} . Evaporation takes place from the meniscus and at some later time t_2 , the number of atoms and average energy in region A, region B and vapor changes to (N_{2a}, E_{2a}) , (N_{2b}, E_{2b}) and (N_{2v}, E_{2v}) respectively, as depicted in Fig. 5-4b. The goal here is to find the average heat and evaporation flux rates from regions A and B. Please note that the number of atoms in the domain is constant. Also, as there is no flow in the directions parallel to the surface, the net amount of atoms transferred between regions A and B is assumed to be zero.

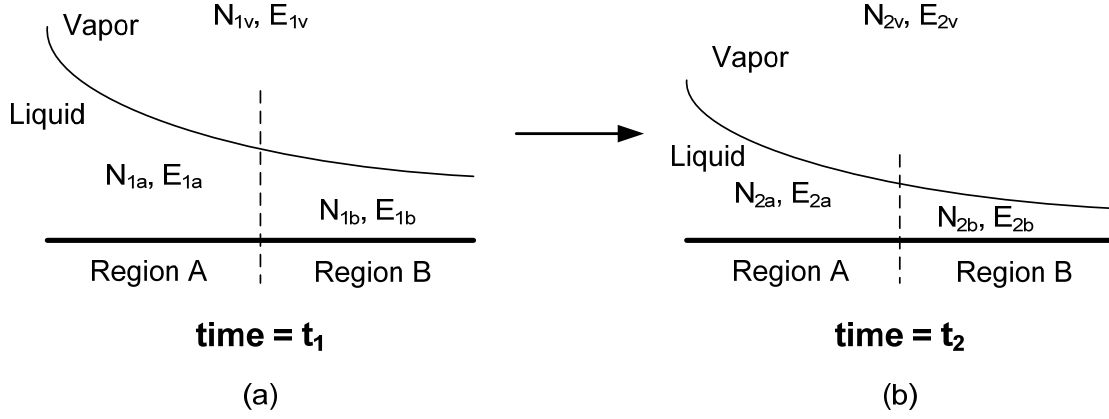


Figure 5-4. Schematic showing two regions of an evaporating meniscus at times t_1 and t_2

Let the total number of atoms evaporated in the entire domain be N_{ev} , and the atoms evaporated from regions A and B are N_{ev-a} and N_{ev-b} respectively. Thus,

$$N_{ev-a} = N_{1a} - N_{2a} \quad (5.4)$$

$$N_{ev-b} = N_{1b} - N_{2b} \quad (5.5)$$

$$N_{ev} = N_{2v} - N_{1v} = N_{ev-a} + N_{ev-b} = (N_{1a} + N_{1b}) - (N_{2a} + N_{2b}) \quad (5.6)$$

Total energy of domain at time t_1 $E_{1total} = N_{1a}E_{1a} + N_{1b}E_{1b} + N_{1v}E_{1v}$

Total energy of domain at time t_2 $E_{2total} = N_{2a}E_{2a} + N_{2b}E_{2b} + N_{2v}E_{2v}$

Thus, net energy transferred to the fluid from the heated surface:

$$\Delta E_{net} = E_{2total} - E_{1total} \quad (5.7)$$

$$= (N_{2a}E_{2a} - N_{1a}E_{1a}) + (N_{2b}E_{2b} - N_{1b}E_{1b}) + (N_{2v}E_{2v} - N_{1v}E_{1v})$$

$$= [N_{2a}E_{2a} - (N_{2a} + N_{ev-a})E_{1a}] + [N_{2b}E_{2b} - (N_{2b} + N_{ev-b})E_{1b}] + [(N_{1v} + N_{ev-a} + N_{ev-b})E_{2v} - N_{1v}E_{1v}]$$

Re-arranging:

$$\Delta E_{net} = N_{2a} (E_{2a} - E_{1a}) + N_{ev-a} (E_{2v} - E_{1a}) + N_{2b} (E_{2b} - E_{1b}) + N_{ev-b} (E_{2v} - E_{1b}) + N_{1v} (E_{2v} - E_{1v}) \quad (5.8)$$

The last term $N_{1v} (E_{2v} - E_{1v})$ accounts for the part of energy transfer used to heat up the initial vapor atoms from E_{1v} to E_{2v} . This is done indirectly by the higher energy atoms which are evaporated from the meniscus interface and heat up the vapor atoms already present in the vapor space. In order to divide this term for regions A and B, we must know how many initial vapor atoms have been heated up by evaporating atoms from region A and from region B, which is very complex to evaluate accurately. Thus, as an approximation, the last term is divided for regions A and B by introducing a weighting factor based on the fraction of atoms evaporated from each region as follows:

$$N_{1v} (E_{2v} - E_{1v}) = \frac{N_{ev-a}}{N_{ev}} N_{1v} (E_{2v} - E_{1v}) + \frac{N_{ev-b}}{N_{ev}} N_{1v} (E_{2v} - E_{1v}) \quad (5.9)$$

Thus, the net heat transfer term can now be written as the summation of heat transfer from region A and heat transfer from region B:

$$\Delta E_{net} = \Delta E_A + \Delta E_B \quad (5.10)$$

where,

$$\Delta E_A = N_{2a} (E_{2a} - E_{1a}) + N_{ev-a} (E_{2v} - E_{1a}) + \frac{N_{ev-a}}{N_{ev}} N_{1v} (E_{2v} - E_{1v})$$

$$\Delta E_B = N_{2b} (E_{2b} - E_{1b}) + N_{ev-b} (E_{2v} - E_{1b}) + \frac{N_{ev-b}}{N_{ev}} N_{1v} (E_{2v} - E_{1v})$$

This can be generalized to obtain the heat transfer from a meniscus divided into N regions. The heat and evaporation flux rates, between time t_1 and t_2 , from a region R can be evaluated using the following equations:

$$\text{Heat flux rate} = \frac{N_{2R}(E_{2R} - E_{1R}) + N_{ev-R}(E_{2v} - E_{1R}) + \frac{N_{ev-R}}{N_{ev-total}} N_{1v}(E_{2v} - E_{1v})}{(Area)(t_2 - t_1)} \quad (5.11)$$

$$\text{Evaporation flux rate} = \frac{(N_{1a} - N_{2a})m_{atom}}{(Area)(t_2 - t_1)} \quad (5.12)$$

Results and Discussion – Case I

Figure 5-5 shows the snapshots of the computational domain at different time intervals. In Fig. 5-5a, the meniscus has a smooth curvature as evaporation has not yet started and surface tension assists in the formation of the interface. Vigorous evaporation is seen in Fig. 4b which results in an uneven meniscus interface. As evaporation rate slows down comparatively, a uniform but increased curvature is obtained in Fig. 5-5c. The decrease in evaporation rate is due to the increase in vapor pressure. With continuous evaporation taking place, the thinnest part of the meniscus at the center continues to decrease in thickness (Figs. 5-5d, 5-5e) until a uniform non-evaporating film forms. The curvature of remaining part of the meniscus is sharper than before evaporation began.

The formation of the non-evaporating film is again confirmed from Fig. 5-6. This figure shows the variation of liquid atoms with time for regions 5 to 10. Regions 5 and 6, which are at the center of the meniscus, show no further evaporation after 2000 ps thus resulting in a non-evaporating film. Liquid atoms in regions 7 and 8 continue to evaporate, similar to the results obtained from analytical solutions of a macroscopic evaporating meniscus. However, this work shows a clearer picture of the physics occurring at and in the vicinity of the nanoscale non-evaporating film which cannot be accurately simulated using macroscopic theories. Regions 7 and 8 can be labeled as the interline region. Region 10, which is adjacent to the nanochannel, shows an increase in the number of liquid atoms. The reason is that the average temperature of

this region is lower than the vapor and thus condensation in this region causes the increase in liquid atoms (as also seen in Fig. 5-5).

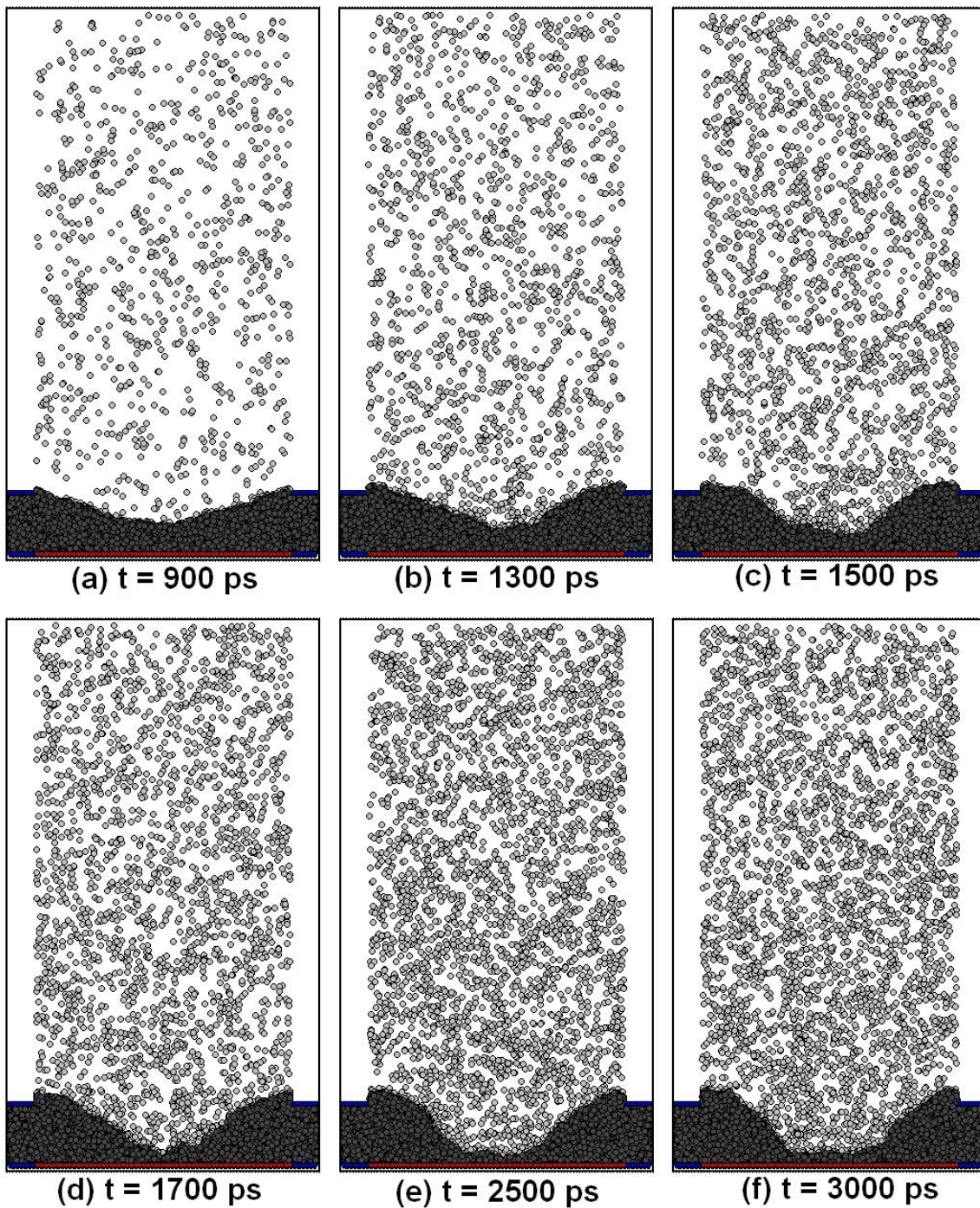


Figure 5-5. Snapshots of x-z plane at different time steps for Case I

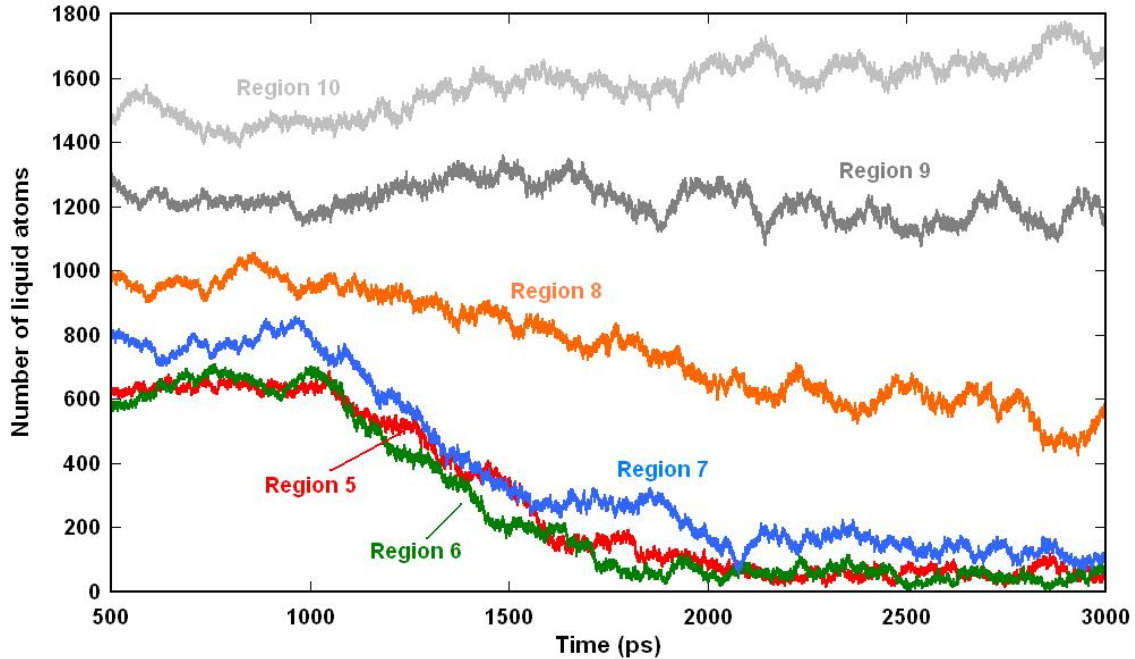


Figure 5-6. Variation of liquid atoms with time for regions 5-10 for Case I

The pressure in the vapor space is calculated at every time step, and is averaged over a time period of 50 ps (10,000 time steps). The pressure variation with time is shown in Fig. 5-7. As the computational domain is closed, the pressure increases from an initial value, averaged from 800-1000 ps, of 0.154 MPa to a value of 0.630 MPa in the final 200 ps. The saturation temperature corresponding to this final pressure is $T_{\text{sat-pres}} = 109.17$ K. Figure 5-8 shows the average temperature of each region from 800-1000 ps and 2800-3000 ps. For regions 5 and 6, although the temperatures are high, there is no evaporation after 2000 ps. A non-evaporating thin film can exist in equilibrium on a solid surface even when the vapor pressure in the surrounding gas is below the normal saturation pressure for the film temperature (Carey 1992). This reiterates that the film in regions 5 and 6 is non-evaporating.

The net heat flux and evaporation flux rates are shown in Fig. 5-9 for regions 1 through 10. The heat flux values are averaged over $t_1 = 800-1000$ ps, $t_2 = 1500-1700$ ps and $t_3 = 2700-2900$ ps. The overall average heat flux rates are maximum for regions 4 and 7 since evaporation

continues to take place. The initial heat flux rates from regions 5 and 6 are higher until the non-evaporating film is formed, after which no further evaporation occurs. Regions 1 and 10 show negative heat and mass flux rates as the average temperature of these regions are lower than vapor and condensation occurs in these regions. As it can be seen from the values, high heat flux rate of the order of 100 MW/m^2 and high evaporation rates of the order of $1000 \text{ kg/m}^2\text{s}$ are achievable from nanoscale evaporating meniscus. Based on these values, very high heat/mass transfer rates exist during the early stages of bubble growth during the formation of the non-evaporating film at the bubble base; however as the time required for its formation is only on the order of nanoseconds, the high flux rates are only sustained for a very short period of time. Engineered manipulation of extending the time period of formation of non-evaporating film, or its breakage after formation can result in significantly higher heat flux rates and delaying the critical heat flux limit at macroscale.

Chen et al. (2004) performed experiments, on a heating surface consisting of microheaters of individual heater area of $270 \mu\text{m} \times 270 \mu\text{m}$, to measure the power consumed throughout the cycle of bubble growth, detachment and departure. Our aim here is to substantiate the heat flux values obtained from molecular dynamics simulation, and gain better understanding of the heat transfer characteristics. Although FC-72 was chosen as the boiling fluid by Chen et al. (2004) and argon is chosen in this work, the Jakob number is one of the key parameters that can affect the contribution of heat transfer mechanisms in nucleate boiling. Jakob number, defined as $Ja = \rho_l c_{pl} (T_w - T_{sat}) / \rho_v h_{fg}$, evaluated for both the cases based on their respective fluid conditions and wall superheat of 40 K result in the following values: $Ja_{FC-72} = 56.25$ and $Ja_{Ar} = 52.29$. For a wall superheat of 44 K, Chen et al. (2004) obtained a heat flux of $\sim 0.5 \text{ MW/m}^2$ during the bubble nucleation and growth process. The average heat flux in regions 4

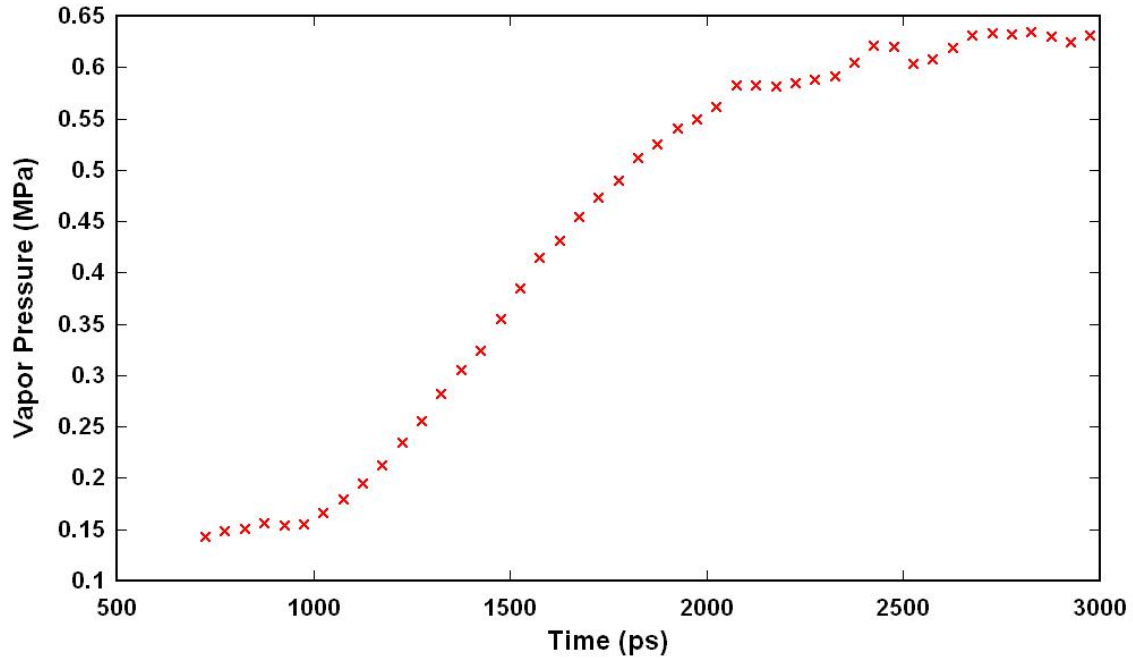


Figure 5-7. Variation of vapor pressure with time for Case I

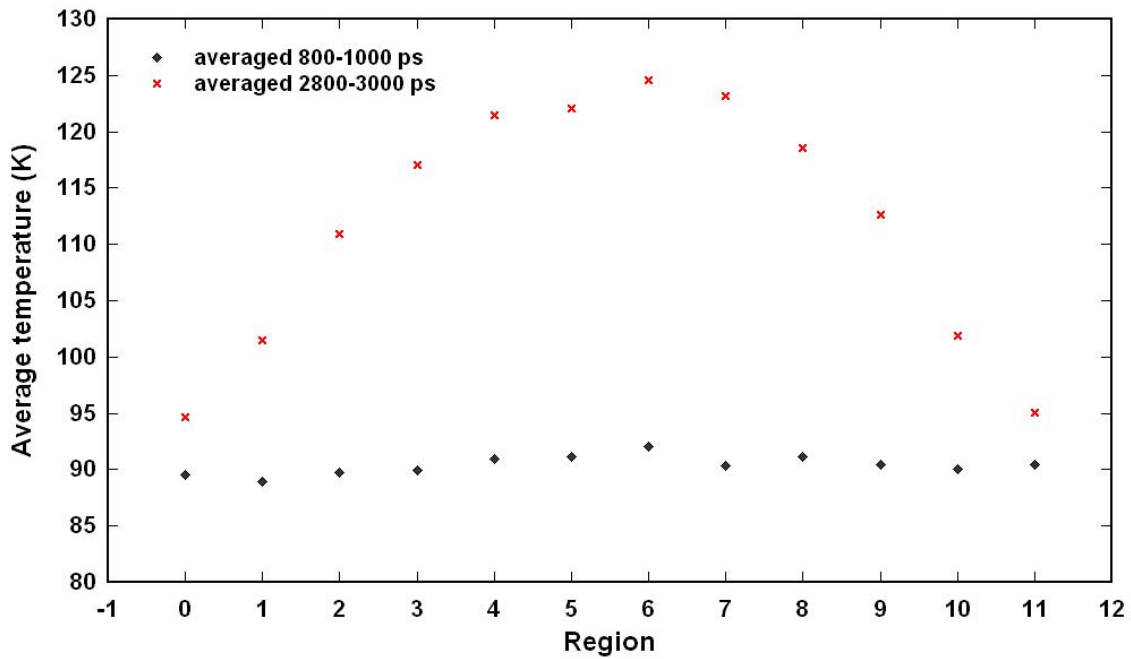


Figure 5-8. Average temperature of regions at initial and final time periods for Case I

through 7 in this work is 258 MW/m^2 . Thus, this provides a missing link to the heat flux values obtained during the formation of the non-evaporating film and interline region in bubble growth

process, which cannot be measured via experiments yet. Figure 5-10 shows a schematic suggesting the heat flux distribution along the nano- and micro-layers at the base of the bubble during the nucleation and early growth process. The formation of the non-evaporating film and the interline region result in very high heat flux rates of 100-1000 MW/m². The heat flux rate drops down significantly as we move away from the interline region into the evaporating film region, although heat transfer occurs for a much longer time in this region. The heat flux rate drops down further into the intrinsic meniscus region. The overall average heat transfer rate is the range of 0.1-1 MW/m² for a wall superheat of 40 K.

Moore and Mesler (1961) studied during nucleate boiling by measuring the surface temperature of a microscale area beneath the nucleating bubble. The thermocouple measured the average temperature around a circle of diameter 0.005 inch (area = $1.267 \times 10^{-8} \text{ m}^2$). The fluid boiled in the experiments was water at atmospheric pressure, and it was maintained at its saturation temperature by auxiliary heaters. The authors found that the surface temperature occasionally dropped 20°F to 30°F. They calculated the heat flowing out of the heater (from the thermocouple region) during these temperature drops, and obtained heat flux rates as high as 200,000 Btu/hr.ft² ($\sim 6.31 \text{ MW/m}^2$). The authors conclude that the high heat flux rates are due to the vaporization of the microlayer at the base of the bubble when it is growing on the surface. For comparison purposes, the critical heat flux of water at atmospheric pressure is $\sim 1 \text{ MW/m}^2$. Thus, high heat fluxes for a short interval of time are possible from the base of the bubble, similar to what we have obtained from MD simulations.

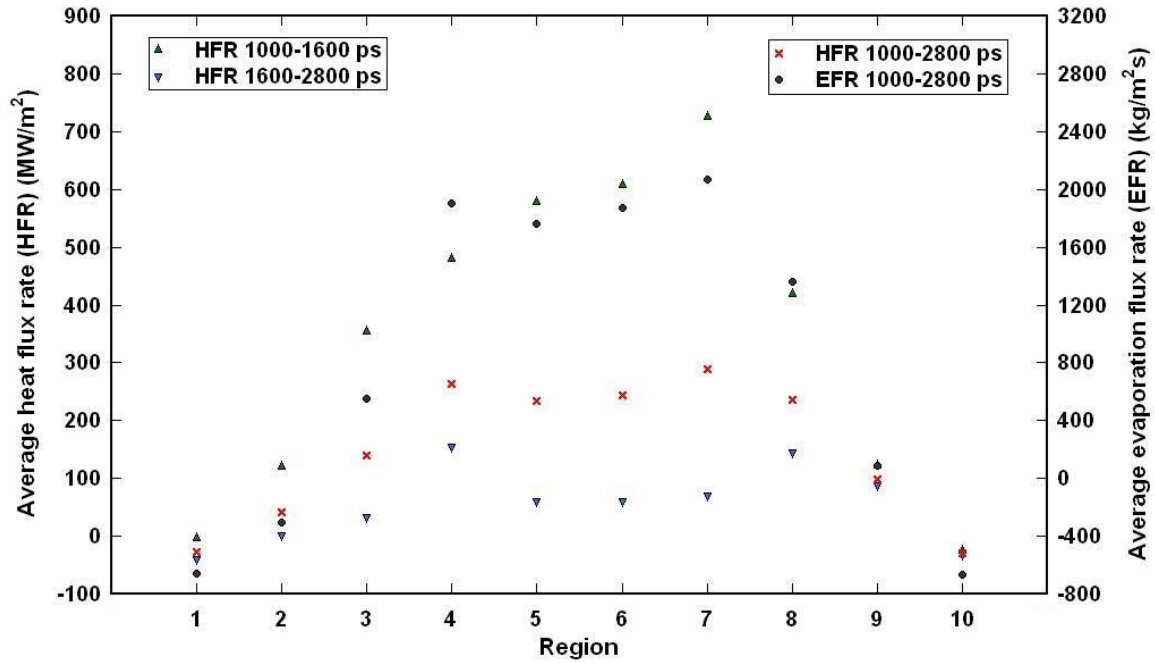


Figure 5-9. Average heat and evaporation flux rates for regions 1-10 during the total heating period for Case I

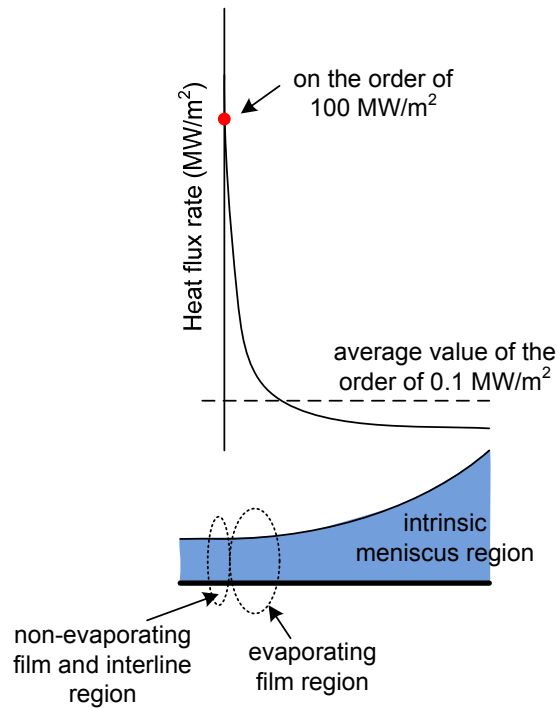


Figure 5-10. Heat flux distribution along nano- and micro-layers at the base of the bubble

Figure 5-11 shows the disjoining pressure variation along the length of the meniscus at three different time steps. During the initial equilibrium period, the disjoining pressure is small owing to the thicker meniscus height. As evaporation occurs, the thickness at center of the meniscus begins to decrease resulting in increase of disjoining pressure. It increases significantly upon the formation of non-evaporating film, and at the end of the simulation period ($t=2500$ ps) its value in the non-evaporating film region is 4.34 MPa. The disjoining pressure quickly goes down to near-zero values as the meniscus thickness increases away from the non-evaporating film region.

The capillary pressure shows an interesting trend for nanoscale meniscus in Fig. 5-12. At $t=1500$ ps, the capillary pressure is higher than the disjoining pressure at the center of the meniscus since the meniscus has increased curvature and non-evaporating film has not formed. At the end of the simulation, the capillary pressure is zero in the non-evaporating region as expected. However, negative capillary pressure values are seen at the ends of the meniscus, and the absolute values are significantly higher towards the end of the simulation than compared to during initial equilibrium. The reason for the negative pressure is that the liquid film at the ends of the meniscus is being pulled by the liquid in the nanochannel, and also towards the center of the meniscus due to high disjoining pressure. Since there is no additional feed-in of atoms to negate the pulling effects in this simulation setup, pressure at the ends of the meniscus reaches negative values. Usually a negative capillary pressure would result in cavitation in the liquid. A sample calculation in region 10, where the negative pressure is greatest, shows that for $\gamma_{LV} = 0.009$ N/m and $P = -1.87$ MPa (averaged over the region), the value of $R_c \sim 9.63$ nm which is greater than the possible capillary height of 7.96 nm (average height of interface in the region). Thus, the meniscus can exist in metastable state in this case.

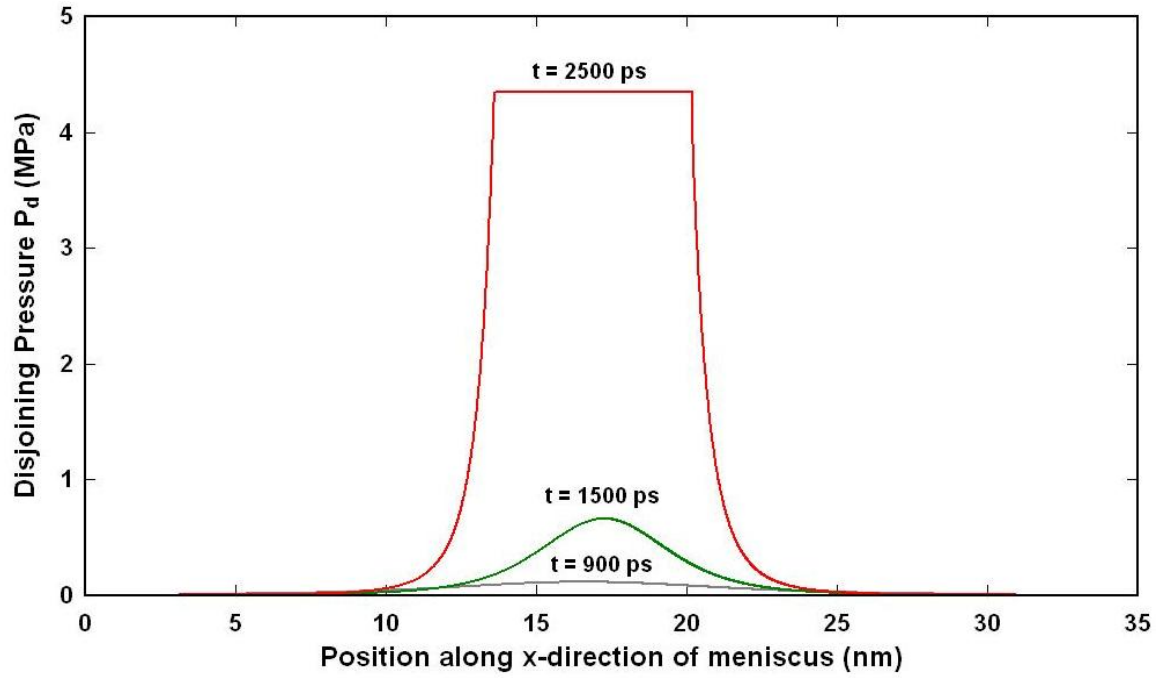


Figure 5-11. Variation of disjoining pressure along meniscus length for Case I

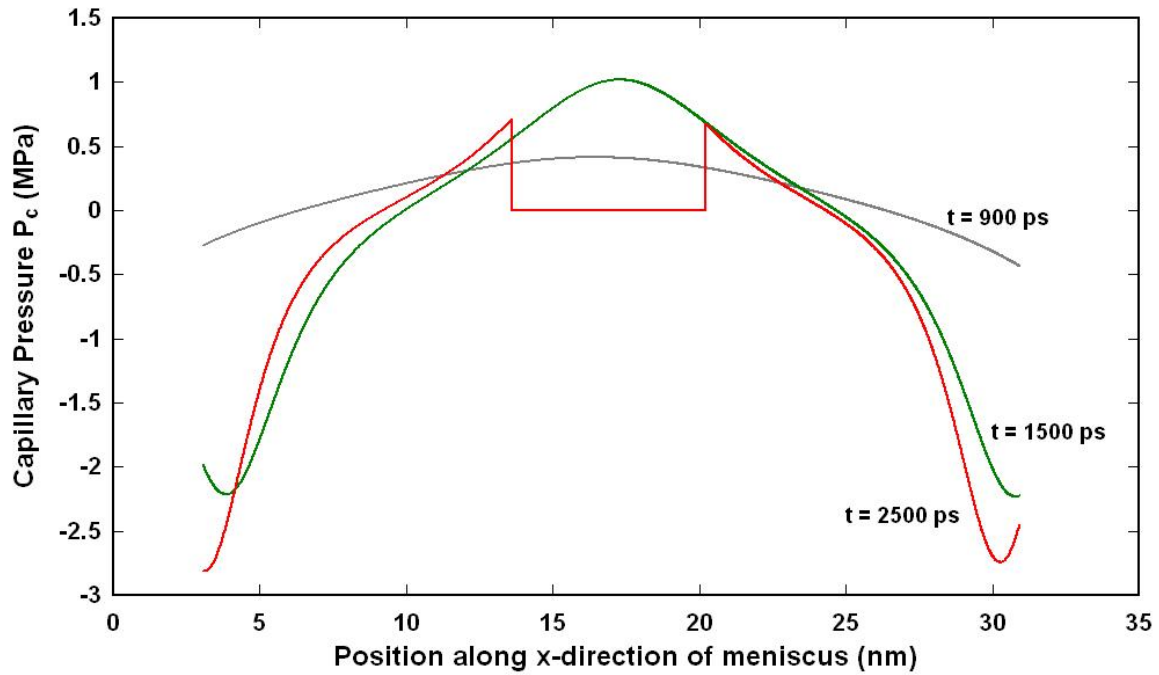


Figure 5-12. Variation of capillary pressure along meniscus length for Case I

Results and Discussion – Case II

Figure 5-13 depicts the computational domain for Case II at different time intervals. Unlike Case I, all walls are at a higher temperature and liquid argon in the nanochannels is also heated up. The liquid in the nanochannel expands decreasing its density due to which some atoms (~ 300 atoms from each nanochannel) are pushed towards the meniscus and in turn get evaporated. Evaporation flux is higher in Case II as the meniscus is at a greater temperature than Case I. As can be seen from Figs. 5-13d-f, meniscus curvature is less steep and more concave in shape compared to Case I.

Figure 5-14 shows the variation of liquid atoms for regions 5 to 10. Similar to Case I, non-evaporating film forms at the center of the meniscus in regions 5 and 6. However, the non-evaporating film is formed at a much later stage, at around 2500 ps, and is also greater in thickness compared to Case I. Evaporation also occurs from regions 9 and 10 since those regions are at a higher temperature than in Case I. The pressure in the vapor space is calculated at every time step, and is averaged over a time period of 50 ps (10,000 time steps). The pressure increases from an initial value, averaged from 800-1000 ps, of 0.153 MPa to a value of 1.168 MPa in the final 200 ps. The saturation temperature corresponding to this final vapor pressure is $T_{\text{sat-pres}} = 119.32$ K. Figure 5-15 shows the average temperature of each region from 800-1000 ps and 2800-3000 ps. Temperatures of all regions of the meniscus are greater than $T_{\text{sat-pres}}$ and thus evaporation occurs from all meniscus regions, except the non-evaporating regions. As mentioned earlier, a non-evaporating thin film can exist in equilibrium on a solid surface even when the vapor pressure in the surrounding gas is below the normal saturation pressure for the film temperature (Carey 1992).

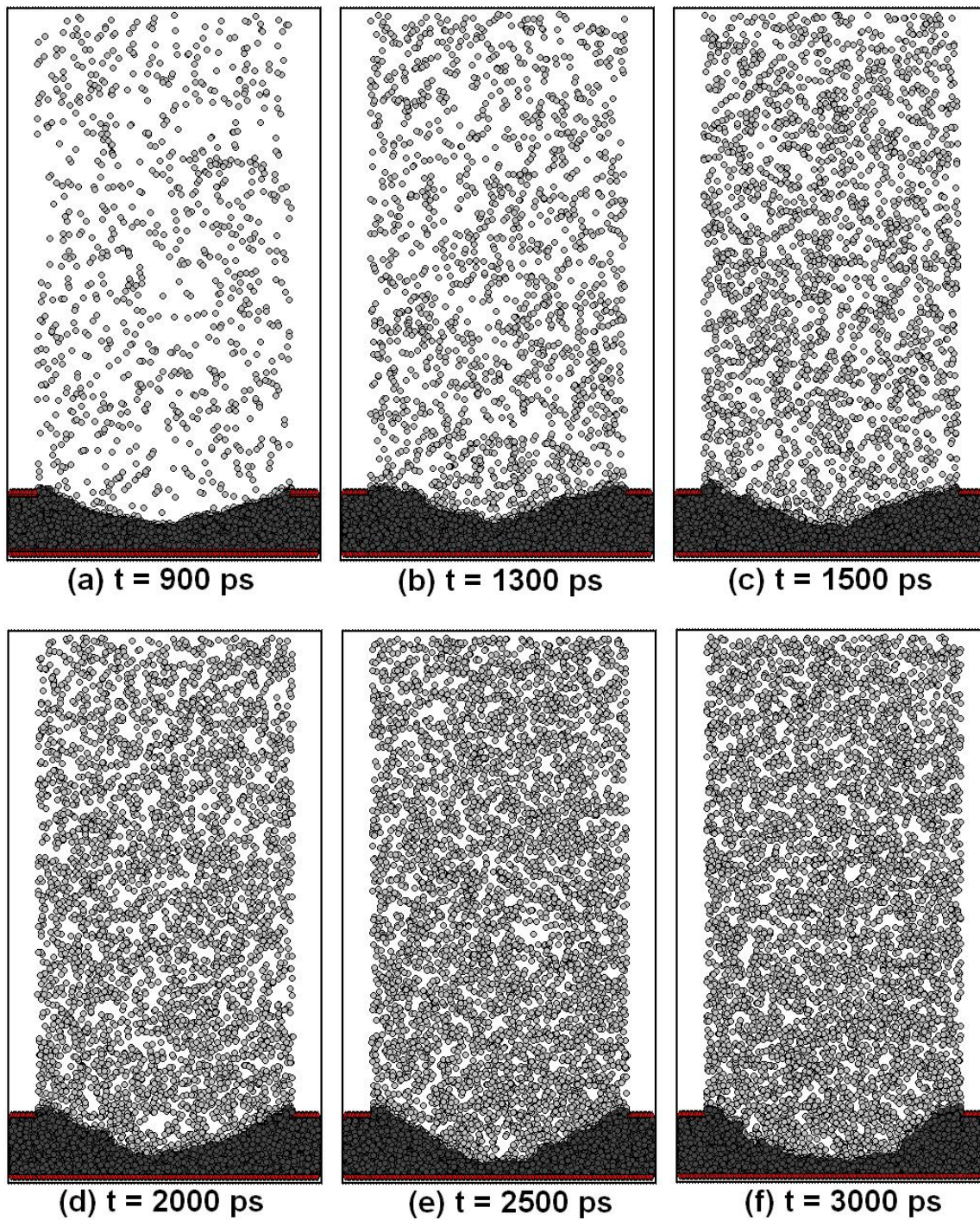


Figure 5-13. Snapshots of x-z plane at different time steps for Case II

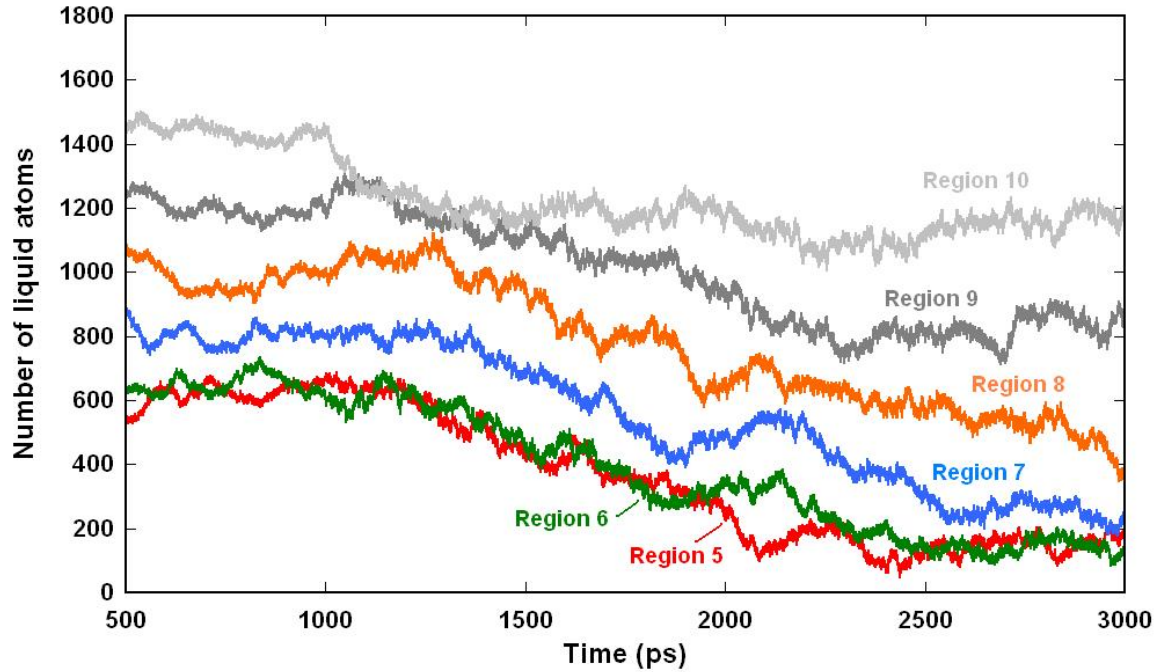


Figure 5-14. Variation of liquid atoms with time for regions 5-10 for Case II

The net heat flux and evaporation flux rates are shown in Fig. 5-16 for regions 1 through 10. The heat flux values are averaged over $t_1 = 800-1000$ ps, $t_2 = 1500-1700$ ps and $t_3 = 2700-2900$ ps. The overall average heat flux rates are minimum for regions 5 and 6, unlike Case I, since non-evaporating film forms in these regions whereas evaporation continues to take place in other meniscus regions due to higher temperature. High heat flux values are seen in the first 600 ps of evaporation period from regions near the nanochannels due to higher temperature, and addition of atoms from the nanochannel to these regions. During the later part of the evaporation period (1600-2800 ps), evaporation from those regions significantly reduce as the remaining atoms have greater resistance to evaporation due to the attractive forces by the atoms in the nanochannels. In this period, maximum heat flux occurs from regions 3, 4, 7 and 8; formation of non-evaporating film in region 5 and 6 reduce their heat flux rates. Overall, as expected, maximum evaporation occurs from region 4 and 7 i.e. regions surrounding the non-evaporating film (interline regions).

Figure 5-17 shows the disjoining pressure variation along the width of the meniscus at three different time steps for Case II. The disjoining pressure is greater for Case I ($P_d = 4.34$ MPa) than Case II ($P_d = 1.31$ MPa) as expected. For Case I, the meniscus is pulled towards the nanochannel walls as the temperature is lower there compared to at the center of the meniscus. This causes the non-evaporating film to be thinner at the center. However, in Case II the nanochannel walls are also heated causing more atoms to flow to the meniscus, and since the meniscus is not pulled with the same intensity towards the nanochannels like in Case I, and also due to the higher temperature, the atoms in the meniscus have more freedom to rearrange resulting in a more uniform curvature. This increases the thickness of the non-evaporating film at the center of the meniscus for Case II, and hence the disjoining pressure is lower.

The capillary pressure variation along the length of the meniscus is shown in Fig. 5-18 for Case II. At $t=1500$ ps, the capillary pressure is higher than the disjoining pressure at the center of the meniscus since non-evaporating film has not formed. At $t=2500$ ps, the capillary pressure is zero in the non-evaporating region as the non-evaporating film has a flat curvature. However, negative capillary pressure values are seen, similar to Case I, at the ends of the meniscus near the nanochannels. Since the meniscus is at a higher temperature in Case II along with lower disjoining pressure at center, pressure at the ends of the meniscus reach higher negative values for Case I ($P_c \sim -2.5$ MPa) compared to Case II ($P_c \sim -1$ MPa). To verify that cavitation cannot occur, the critical cavitation radius is calculated in region 10. $\gamma_{LV} = 0.0044685$ N/m and $P = -0.79$ MPa (averaged over the region), the value of $R_c \sim 11.31$ nm which is greater than the possible capillary height of 6.61 nm (average height of interface in the region).

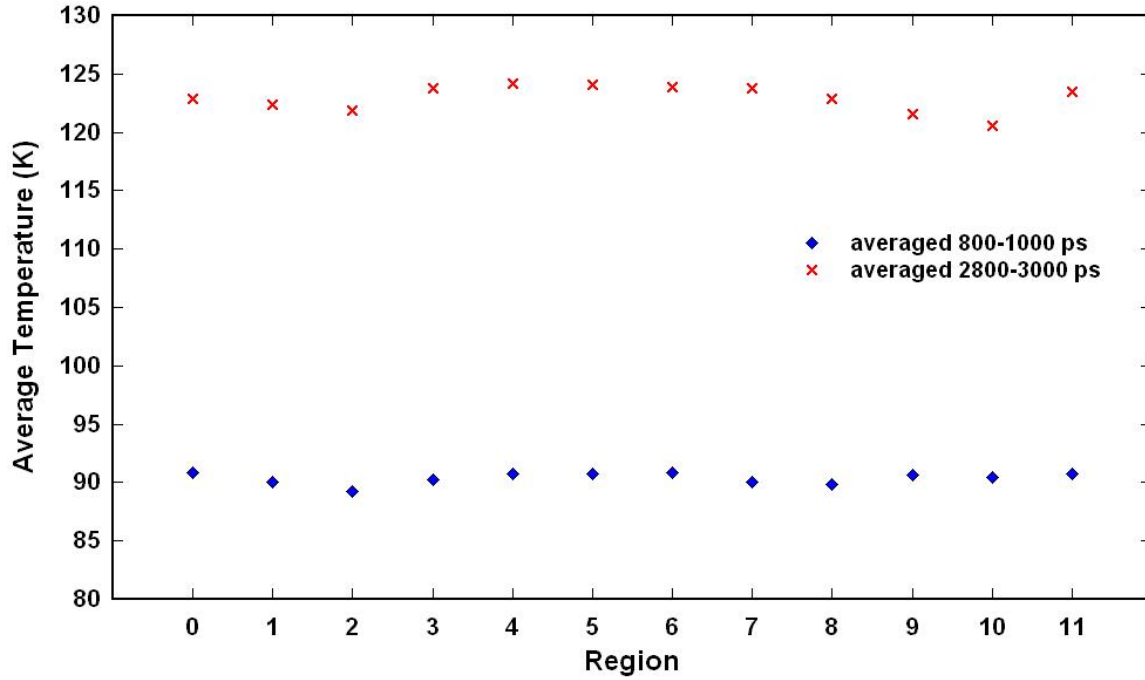


Figure 5-15. Average temperature of regions at initial and final time periods for Case II

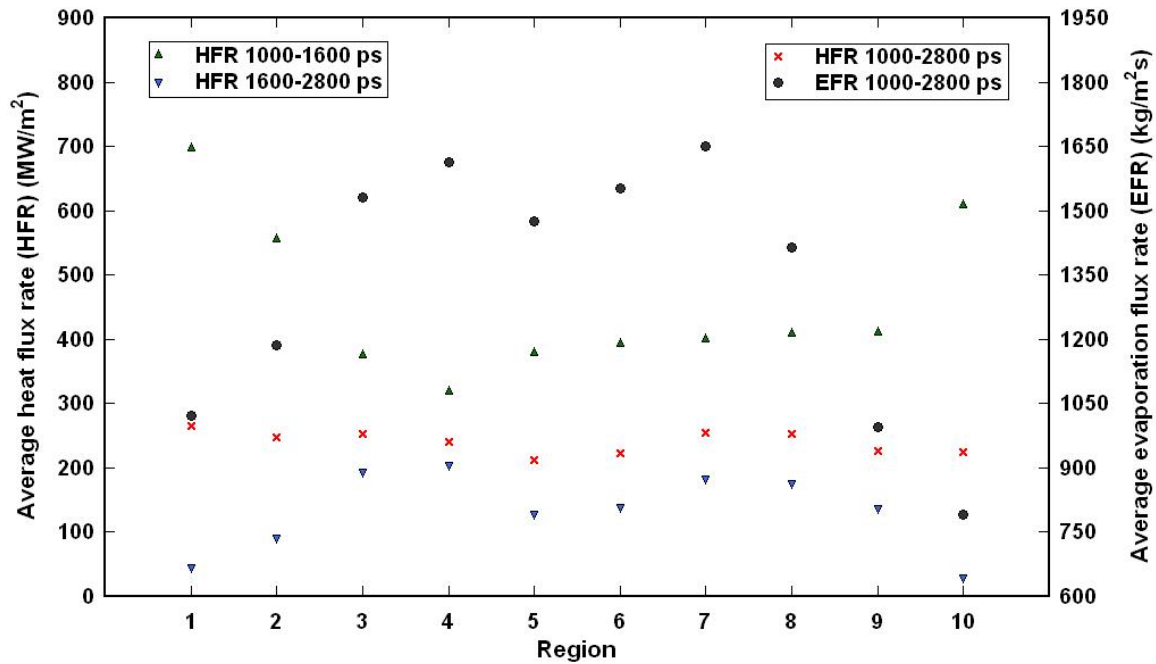


Figure 5-16. Average heat and evaporation flux rates for regions 1-10 during the total heating period for Case II

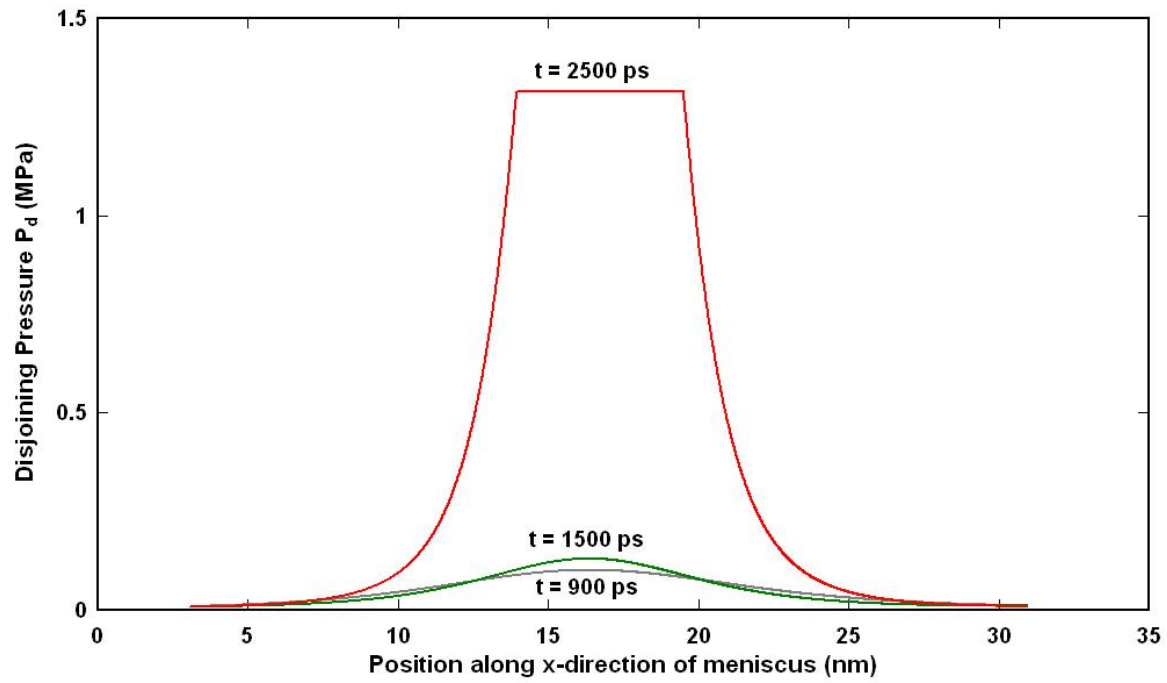


Figure 5-17. Variation of disjoining pressure along meniscus length for Case II

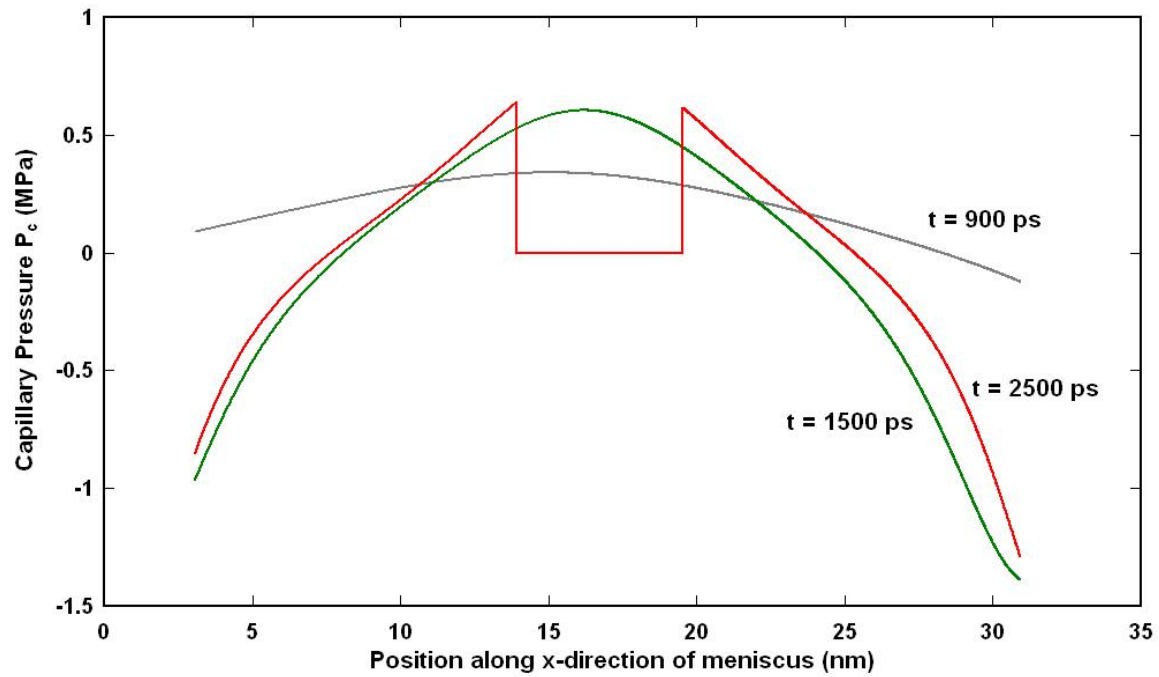


Figure 5-18. Variation of capillary pressure along meniscus length for Case II

Meniscus Boundary Condition

As mentioned earlier, the curved meniscus was formed in this simulation by using nanochannels on either side of the meniscus. The liquid atoms inside the nanochannels provide the necessary attractive force for meniscus formation. If the nanochannels were to be removed, the meniscus would change shape to minimize its free energy and result in a flat thin film. However, using nanochannels to form the meniscus is computationally demanding and also provides physical interference in pure-meniscus analysis. Hence, a meniscus boundary condition is required. The boundary condition should provide external force, which should be a function of distance, to the meniscus atoms so as to form a curvature. Two methods are proposed in this section, the first one being an analytical solution and the second derived using curve-fitting from this present work.

Analytical Meniscus Boundary Condition

Figure 5-19a shows the schematic of a meniscus. The meniscus is made up of liquid atoms surrounded by vapor. Since molecular dynamics computations are very exhaustive, taking into account the complete meniscus would be impractical. Hence, the domain is restricted between two boundaries (named 1 and 2) as shown. In order to maintain the meniscus curvature, the liquid atoms within the boundaries should still experience force from the extended meniscus regions as shown. An analytical function is derived here to serve this purpose. The extended meniscus region is approximated by rectangular regions as shown. The force exerted by a rectangular region on an atom, say atom P, is evaluated as shown in Fig. 5-19b. Atom P has coordinates x_0, y_0, z_0 . The rectangular region is of height t , thickness Δx , infinite in y -direction, and its center is at coordinates x_1, y_1 and z_1 .

Consider a infinitesimal element in the rectangular region as shown of constant thickness Δx , width dw and height dh . Let $x = x_1 - x_0, y = y_1 - y_0$ and $z = z_1 - z_0$. Using Lennard-Jones potential for

argon-argon interaction, the energy of interaction, dU , between P and the infinitesimal element is:

$$dU = 4\varepsilon \left[\left(\frac{\sigma}{r} \right)^{12} - \left(\frac{\sigma}{r} \right)^6 \right] \left(\frac{\rho N_{av}}{M} \right) (\Delta x) dw dh \quad (5.13)$$

where $(\rho N_{av}/M)$ is the number of atoms per unit volume in the rectangular region, and r is the defined as:

$$\begin{aligned} r^2 &= (x_1 - x_0)^2 + (y_1 + w - y_0)^2 + (z_1 + h - z_0)^2 \\ &= x^2 + (y + w)^2 + (z + h)^2 \end{aligned} \quad (5.14)$$

Substituting in equation 5.13 and integrating as follows:

$$\begin{aligned} U &= \int_0^t \int_{-\infty}^{\infty} 4\varepsilon \left(\frac{\rho N_{av}}{M} \right) (\Delta x) \left[\left(\frac{\sigma}{\sqrt{x^2 + (y+w)^2 + (z+h)^2}} \right)^{12} - \left(\frac{\sigma}{\sqrt{x^2 + (y+w)^2 + (z+h)^2}} \right)^6 \right] dw dh \\ \Rightarrow U &= \int_0^t 4\varepsilon \left(\frac{\rho N_{av}}{M} \right) (\Delta x) \left[\frac{63\pi\sigma^{12}}{256} \left(\frac{1}{\sqrt{x^2 + (z+h)^2}} \right)^{11} - \frac{3\pi\sigma^6}{8} \left(\frac{1}{\sqrt{x^2 + (z+h)^2}} \right)^5 \right] dh \\ \Rightarrow U &= 4\varepsilon \left(\frac{\rho N_{av}}{M} \right) (\Delta x) \left[\frac{63\pi\sigma^{12}}{256} f_1(x, z) - \frac{3\pi\sigma^6}{8} f_2(x, z) \right] \end{aligned} \quad (5.15)$$

where,

$$f_1(x, z) = \frac{0.0031746 h' (315x^8 + 840h'^2x^6 + 1008h'^4x^4 + 576h'^6x^2 + 128h'^8)}{(x^2 + h'^2)^{9/2} x^{10}} \Bigg|_{h'=z}^{h'=z+t} \quad (5.16)$$

$$f_2(x, z) = \frac{h' (3x^2 + 2h'^2)}{3(x^2 + h'^2)^{3/2} x^4} \Bigg|_{h'=z}^{h'=z+t} \quad (5.17)$$

In order to obtain the net force acting on atom P from the rectangular region in x , y and z directions, the energy of interaction U has to be differentiated as follows:

$$F_x = -\frac{dU}{dx}; \quad F_y = -\frac{dU}{dy}; \quad F_z = -\frac{dU}{dz} \quad (5.18)$$

As it can be seen from the above derivation, the final analytical solution turns out to be complicated, cumbersome and computationally demanding to implement in a molecular dynamics simulation, and all combinations of atoms and rectangular regions will have to be considered at each time step. A simpler approximation is presented in the next section.

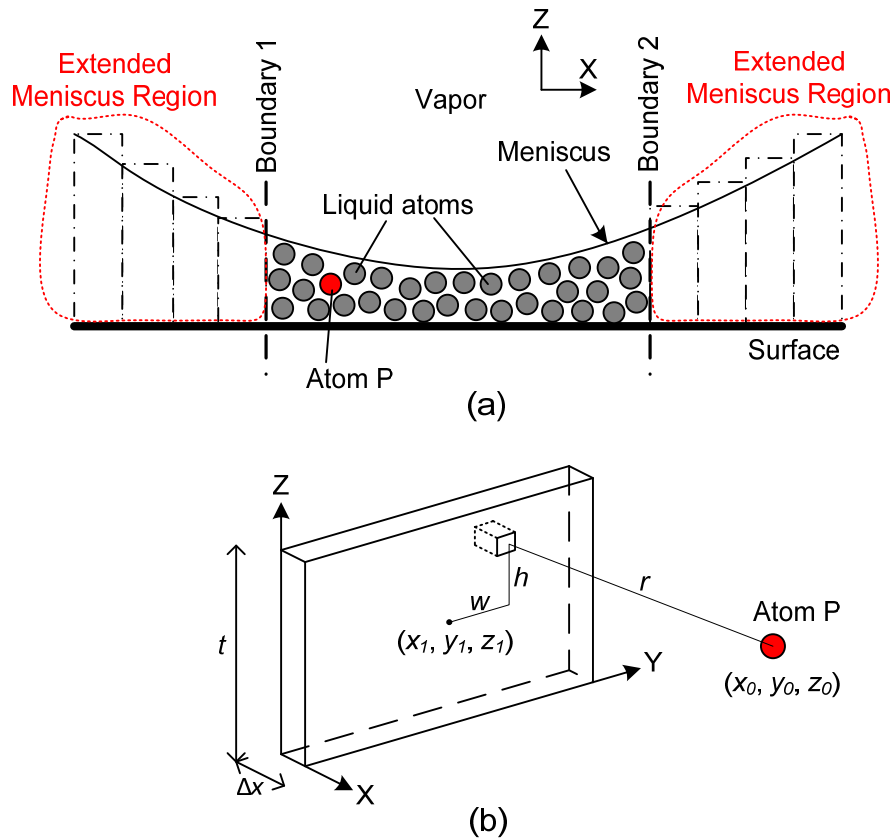


Figure 5-19. (a) Schematic of a meniscus to compute forces acting by the extended meniscus region on liquid atoms in the bounded meniscus region, and (b) configuration for force interaction between an atom and a rectangular region

Curve-Fitted Meniscus Boundary Condition

In this present work, the meniscus was formed using the presence of nanochannels as shown in schematic of Fig. 5-20. During initial equilibrium, the meniscus was divided into equal

length slices of 0.5σ (shown in Fig. 12 as 1, 2, 3, 4, 5... N) and the liquid atoms in the meniscus were assigned to their respective slices. The force exerted by the nanochannel, which includes atoms of argon as well as platinum wall, on all the atoms present in each slice was computed using molecular dynamics simulation in x, y and z-directions. Figure 5-21 shows the variation of forces acting on the slices as a function of distance from the nanochannel.

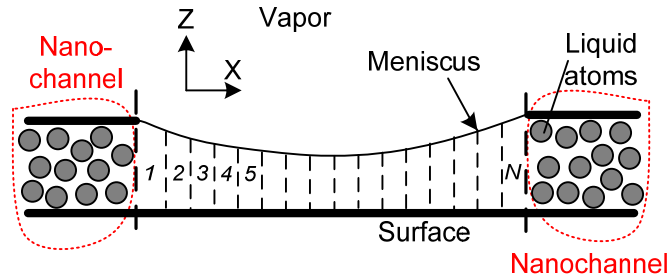


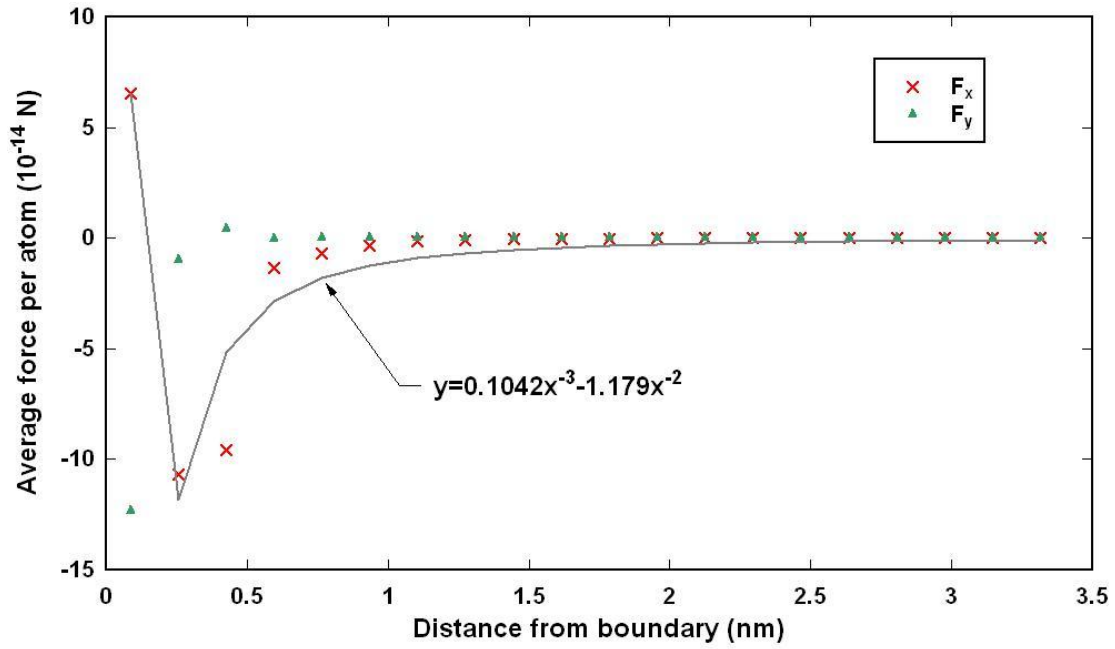
Figure 5-20. Schematic showing meniscus and nanochannels used in the present work to determine the force distribution along the meniscus length by the nanochannels

Force in the y direction is nearly zero, as expected, since the boundary conditions are periodic. Forces in x and z directions follow a trend similar to Lennard-Jones potential. However, the force curves here are significantly steeper. A function similar to the Lennard-Jones potential, $F_x = Ax^{-B} - Cx^{-D}$, is used for curve fitting. This external force can be applied as a meniscus boundary condition for a Lennard-Jones fluid. The following curve fits, as shown in Figs. 5-21a and 5-21b, match the data points:

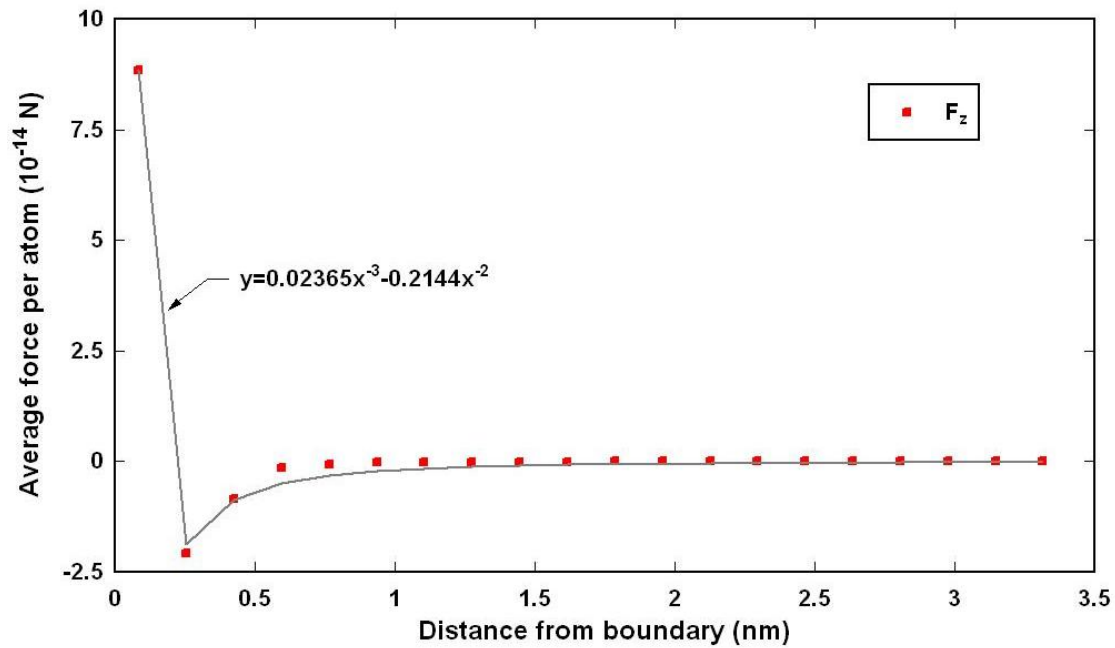
$$F_x = 0.1042x^{-3} - 1.179x^{-2}; \quad F_y = 0; \quad F_z = 0.02365x^{-3} - 0.2144x^{-2} \quad (5.19)$$

where x is in nm and F is in 10^{-14} N. A general force function can be derived based on the above trends. Thus, a meniscus can be formed by applying a force, $F_n = An^{-3} - Cn^{-2}$ ($n = x, y$ or z ; n is in nm ; F is in 10^{-14} N), at the boundaries of the fluid. The coefficients A and C can be chosen

based on the strength and depth of the force required, which will in turn affect the curvature of the meniscus.



(a)



(b)

Figure 5-21. Force distribution on the meniscus by the nanochannel as a function of the distance from the nanochannel (a) F_x and F_y , (b) F_z

CHAPTER 6 CONCLUSION AND FUTURE WORK

Conclusion

Proposed Thermal Wall Model

A novel ‘fluid-heated wall thermal equilibrium model’ for numerically simulating heating/cooling of fluid atoms by wall atoms is proposed.

- In order to validate the proposed model, the thermal conductivity of argon and the change in internal energy of the system are obtained from simulation and compare well to those from the thermodynamic properties of argon.
- As the two properties evaluated are state-dependent only, additional validation cases are run to test the time-dependent nature of the model by placing liquid argon between two platinum walls with simultaneous heating/cooling of the walls.
- The temperature gradient, along the height of the channel, is evaluated and compared to the analytical solution obtained by solving 1-D heat equation and excellent agreement was found between the predicted and theoretical results.
- Additional simulations are conducted with heating at both walls by increasing the wall temperatures to 120 K for two different nanochannel heights. It is concluded that heat transfer occurs at a faster rate than predicted by the heat equation at nanoscale.
- The error between the molecular dynamics simulation and the heat equation’s analytical result depends on the length scale of the problem and reduces with the increase in channel height. The results compared well in the previous case (with heating and cooling at the walls) since higher heating rate at the upper wall is matched with higher cooling rate at the lower wall. These comparisons show the physical soundness of the proposed model.
- The Maxwell speed distribution (MSD) was used to provide another verification of the proposed ‘fluid-wall thermal equilibrium’ model. At high temperatures argon vapor would behave like an ideal gas. The proposed heat transfer model is responsible for imparting kinetic energy to the argon atoms and evaporation. The simulation results of an evaporating argon thin film on platinum surface matched well with the MSD function; this verifies that the velocities imparted by the proposed fluid-wall heat transfer model follow expected physics and at high temperatures argon vapor behaves like an ideal gas.

Transient Film Evaporation

The ‘fluid-wall thermal equilibrium model’ is used to capture the nano-scale physics of transient phase transition of a thin liquid argon film on a heated platinum surface and the eventual colloidal adsorption phenomenon as the evaporation is diminishing using molecular dynamics. The objective was to provide microscopic characterizations of the dynamic thermal energy transport mechanisms during the liquid film evaporation and also the resulting non-evaporable colloidal adsorbed liquid layer at the end of the evaporation process.

- The simulation domain is constructed of platinum wall atoms with argon as the working fluid. Phase change process is studied by simulating evaporation of a thin liquid argon film on the platinum wall.
- High heat transfer and evaporation rates are obtained.
- Gradual vaporization of the film takes place exponentially decreasing with time and a non-evaporating film is obtained.
- A Hamaker-type analysis is done for the non-evaporating film and the Hamaker constant is obtained using molecular dynamics which has not been attempted before using molecular dynamics simulation. The value of the Hamaker-type constant falls in the typical range.
- This analysis is quantifies the non-evaporating film and makes an attempt to use molecular dynamics simulation results in continuum mechanics.

Simulation of Seven Cases in Nanochannel Film Evaporation

The transient film evaporation simulation is extended further to gain better understanding on the occurrence of the non-evaporating film, and the parameters which govern its formation. Seven cases were studied to determine the effect of variation of nanochannel height and variation of liquid film thickness on heat transfer rate and evaporation rate.

- Non-evaporating film was obtained in cases 1-6.
- The starting heat transfer rate depends on the evaporation rate (due to phase change) and the thickness of liquid film (more atoms implies more energy stored).

- Net heat flux increases with increase in both nanochannel height and liquid film thickness, and et evaporation flux increases with an increase in nanochannel height.
- However, an optimum film thickness exists for a fixed nanochannel height as total number of liquid atoms & vapor volume compete with each other.
- Non-evaporating film thickness, liquid-vapor equimolar position, vapor pressure and Hamaker constant of the non-evaporating films were evaluated.
- The value of Hamaker constant increases with an increase in vapor pressure.
- Vapor pressure was plotted against vapor density for initial and final states, and all the states were found to lie on the vapor saturation curve confirming the occurrence of non-evaporating film.
- Case 7 was designed to simulate evaporation from the upper wall of the nanochannel and condensation on the lower wall. All liquid film from the upper wall was evaporated and no non-evaporating film was obtained.
- Study of all cases show that pressure and temperature are the dominant factors governing the formation of non-evaporating film, whereas wall-liquid molecular interaction is a lesser factor. Wall-liquid molecular interaction only governs the wettability of surface, and a non-evaporating film may or may not form on a specific wall-liquid pair depending on the vapor pressure and wall temperature.

Nano-Droplet Impact on a Homogeneous Surface

The dynamics of nano-droplet impact on a homogeneous surface was also simulated using molecular dynamics. The wettability and temperature of the surface was varied to study four cases. An elliptical interfacial fit was obtained from the computed interface markers with the value of $R^2 \geq 0.999$. Contact angle made by the drop with the wall was obtained using the interfacial fit.

- The nano-drops accelerate significantly on reaching close to the wall and the actual impact velocity is higher than that expected to reach by the application of the external force.
- Complete spreading was obtained for the high wettable surface at 90 K, whereas drop after impact on the low wettable surface at 90 K oscillated about a mean contact angle of 126.7° .

- Liedenfrost phenomenon was observed at wall temperature of 300 K for both cases of wettability, although it was seen that the evaporation rate reduced significantly for the low wettable surface.

Meniscus Evaporation at Nanoscale

The non-evaporating region and the interline region of a three-phase contact line are on the order of nanometers, and hence the heat and mass transfer characteristics are studied using molecular dynamics. A concave meniscus was formed by placing liquid argon between a lower and an upper platinum wall, with an opening in the upper wall. After reaching initial equilibrium, the liquid meniscus was heated by the platinum wall and evaporation was observed. Two cases are studied where in one only a part of the platinum wall is increased in temperature while in the other all the walls temperatures are elevated to obtain evaporation. The liquid meniscus was divided into 10 equal regions, and variation of temperature, energy, total number of liquid atoms in each region was studied over the period of simulation. A non-evaporating film was formed at the center of the meniscus. Heat and mass transfer continued to occur from the interline regions (regions surrounding the non-evaporating film). Very high heat flux rate of the order of 100 MW/m² and high evaporation rates of the order of 1000 kg/m²s are achievable from nanoscale evaporating meniscus. Capillary and disjoining pressures of the liquid meniscus were also computed. The disjoining pressure increased significantly after the formation of the non-evaporating film. High negative capillary pressures were obtained towards the end of the simulation. The reason for the negative pressure is that the liquid film at the ends of the meniscus is being pulled by the liquid in the nanochannel, and also towards the center of the meniscus due to high disjoining pressure. It is shown that cavitation cannot occur as the capillary size is smaller than the critical cavitation radius, and thus the meniscus can exist in metastable state. Negative capillary pressure is not uncommon, and has been experimentally measured by researchers. A meniscus boundary condition was developed using analytical and curve-fitting

methods. The analytical solution turns out to be complicated, cumbersome and computationally demanding to implement in a molecular dynamics simulation. A simpler approximation, using curve-fitting over the statistical data computed from this work, leads to a force function of the form $F_n = An^{-3} - Cn^{-2}$ which can be applied at the boundaries of a liquid film to create a meniscus.

Future Work

For the future work, we will follow the multiscale approach with an innovative three-region model (molecular dynamics, coarse-grained, continuum) to ensure a smooth matching between the nanoscale and the continuum. As shown in Figure 6-1, a multiscale three-region model is proposed where an additional microscale region will be sandwiched between the nano region and the continuum macro region to ensure a smooth transition for accurate results. The three-region model will be applied in the liquid region only, whereas direct nano to continuum matching will be done in the vapor region. The reason is that the density of vapor region is significantly less compared to liquid, and creating coarse-grained model would not be practical. The numerical scheme for each of the three regions is explained next.

Molecular Dynamics Simulation (Nano Region)

As explained in Chapter 2, all MD simulations follow Newton's second law for simple atomic systems or in a more generalized form (Lagrangian/Eulerian formulation) for complex geometry systems. The force on each molecule by all other molecules in the system can be determined by using the molecular interaction potential function. From this force, the equation of motion can be integrated over time to obtain the new positions and velocities of each molecule. This information can be statistically analyzed by space/time averaging to provide macroscopic physical properties, and thus the evolution of the system can be studied.

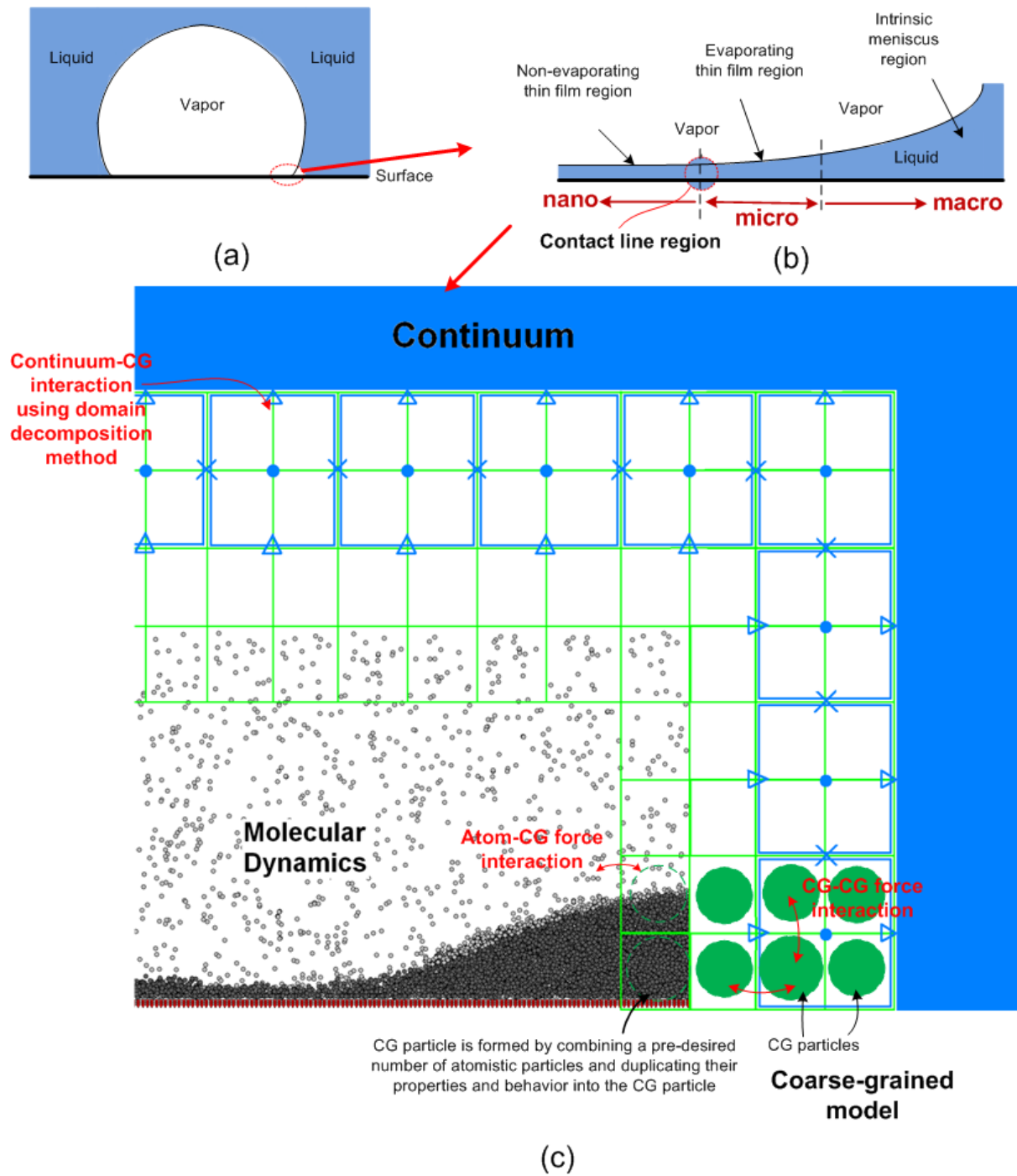


Figure 6-1. Schematic showing multi-scale method of solution for proposed work

Coarse-Grained Method (Micro Region)

The coarse-grained (CG) approach is basically still a discrete particle method where the particles are not the actual atoms or molecules, instead, each CG particle (a quasi-molecule) represents a group of real particles. The number of real particles represented by a CG particle depends on the coarseness level specified. After the details in an actual atomistic description are reduced, the accessible time- and length- scales of molecular simulations can be increased. CG models involve two steps: the first step is to group the degrees of freedom (molecules) in the system into fewer structural units of CG particles. The second step is the construction of an effective force field to describe the interaction between the CG particles. The force-matching (FM) method (Chu et al. 2006) will be used to derive equivalent CG force fields directly from the underlying atomistic forces. The FM procedure applied to the CG trajectories and forces will yield the effective interaction between CG particles as is present in the underlying atomistic simulation. The coarse-grain concept has been extensively researched and developed by the group led by Prof. S. Izvekov. A full review of this method is given in Izvekov and Voth (2005).

Finite Volume Method (Macro Continuum Region)

The numerical algorithm of the finite volume method (FVM), a widely used numerical solution technique in computational fluid dynamics (CFD) for a continuum domain, consists of the following steps:

- Formal integration of the governing differential equations of fluid flow and heat transfer over all the finite control volumes of the solution domain
- Discretization involves the substitution of a variety of finite-difference-type approximations for the terms in the integrated equation representing flow processes such as convection, diffusion and sources. This converts the integral equations into a system of algebraic equations.
- Solution of the algebraic equations (matrix inversion) by an iterative method

The first step, the control volume integration, distinguishes the finite volume method from all other CFD techniques. The resulting statements express the exact conservation of relevant properties for each finite size cell. This clear relationship between the numerical algorithm and the underlying physical conservation principle forms makes the concepts of FVM more effective and accurate than finite-difference, finite element and spectral methods.

Multi-Scale Model and Matching Procedure

Figure 6-1 above shows a schematic of the multiscale model based on the above methods applied to the bubble growth and departure dynamics. Figure 6-1(a) represents a typical bubble on a flat heater surface. Figure 6-1(b) depicts the zoomed-in region at the three-phase contact line and showcases the multi-scale nature of the problem. It has been widely accepted that the three-phase contact line region is constituted of: non-evaporating adsorbed thin film region, evaporating thin-film region (micro layer) and bulk liquid region (macro layer). It is important to model the regions at their respective length-scales to obtain accurate solutions and understand the underlying physics. Figure 6-1(c) shows the MD, AA-CG and FVM methods implementation in the proposed work.

MD simulation and MD-CG matching (nano-micro matching)

The matching between the nano and micro regions will be accomplished by a very attractive approach that is based on creating a mixed all-atom and coarse-grained particle (AA-CG) model (Shi et al. 2006), in which the most interesting part of the system is represented in full atomistic detail, and the remaining parts are modeled at the CG level. The mixed AA-CG model will be used and implemented in the proposed work for matching the two parts. The interactions in the mixed AA-CG model can be classified into: atom-atom, atom-CG and CG-CG interactions.

Forces on all atoms and CG sites are given as:

$$F_i^{atom} = \sum_{j \in atoms, j \neq i} F_{ij}^{atom-atom} + \sum_{j \in CG} F_{ij}^{atom-CG} ;$$

$$F_i^{CG} = \sum_{j \in atoms} F_{ij}^{atom-CG} + \sum_{j \in CG, j \neq i} F_{ij}^{CG-CG}$$

As explained in the previous section, CG particles will be constructed and their force fields will be derived using the FM method. Figure 6-1(c) shows the CG particles as large dots. The AA-CG method accounts for all atom-atom, atom-CG and CG-CG interactions, and thus MD and CG length- and time- scales will be matched intuitively.

CG and FVM matching (micro-macro matching)

Domain decomposition technique will be used to match the CG-FVM for liquid domain, and MD-FVM for vapor domain. The schematic of the technique is shown in Figure 6-2. Initially a steady state solution is assumed in either of the domain, say in CG domain, Ω_{CG} . The solution in Ω_{CG} becomes the overlapped boundary condition for the continuum domain, $\Gamma_{cont-IBC}$. Now, we obtain a solution in Ω_{cont} using $\Gamma_{cont-IBC}$ and non-overlapped, $\Gamma_{cont-EBC}$. The resulting solution in Ω_{cont} gives a new boundary condition Γ_{CG-IBC} for the CG domain. A new solution in Ω_{CG} is obtained using the new boundary conditions. These steps are repeated to march forward in time and study the system evolution. The key element of this method is the scheme for coupling the CG and continuum solutions to ensure continuity of fluxes across the overlap region. Liu et al. (2007) used the same scheme to couple MD-continuum simulations to study heat transfer in a fluid layer confined between flat and rough surfaces. Their results matched well with pure MD results. Our proposed work differs in the way that we have added an additional CG model between the MD and continuum levels to ensure smoother transitioning between the nano and micro length scales in liquid domain. This will lead to more accurate results, as well as application to longer length scales in liquids as density is higher. “Constrained dynamics” will be used to couple the CG and continuum velocities in momentum equations, and temperatures and

energy will be coupled by applying velocity rescaling. Mass fluxes will be coupled by adding/removing CG particles. As can be seen in Figure 6-1, blue boxes depict the staggered grids for continuum simulation. The properties will be averaged from the CG sites: u_x defined at crosses, u_y defined at triangles, and p and T defined at circles. These matching techniques will ensure coupling at different time- and length- scales, and passing of information between them while ensuring conservation of mass, momentum and energy.

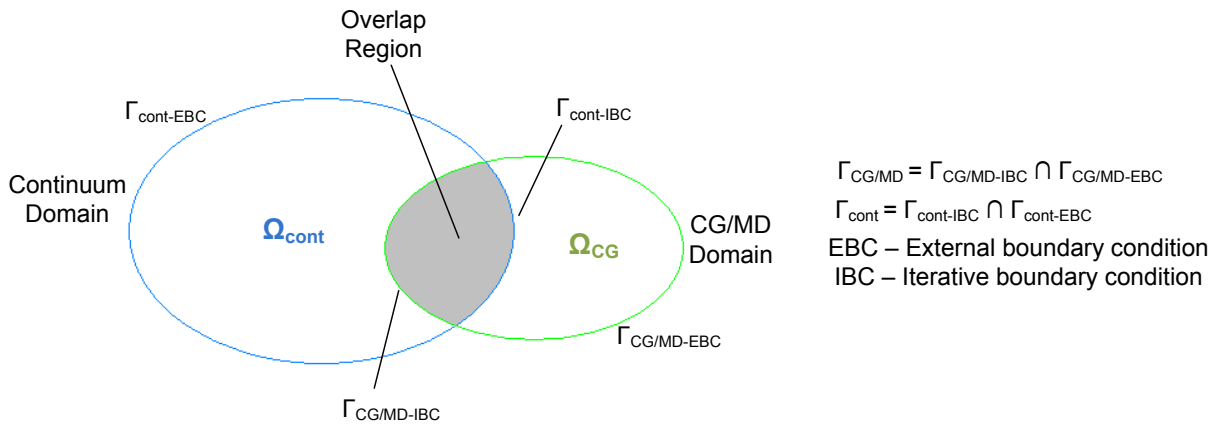


Figure 6-2. Domain Decomposition method

LIST OF REFERENCES

- Abraham FF. 1978. The interfacial density profile of a Lennard-Jones fluid in contact with a (100) lennard-jones wall and its relationship to idealized fluid/wall systems: A monte carlo simulation. *J. Chem. Phys.* 68 : 3713-6
- Adão MH, de Ruijter M, Voué M, De Coninck J. 1999. Droplet spreading on heterogeneous substrates using molecular dynamics. *Phys Rev E.* 59 : 746
- Allen MP, Tildesley DJ. 1987. *Computer simulation of liquids*, Oxford England; New York: Clarendon Press; Oxford University Press. 385pp
- Angell CA. 1988. Approaching the limits. *Nature.* 331 : 206-7
- Blake TD. 2006. The physics of moving wetting lines. *J. Colloid Interface Sci.* 299 : 1-13
- Briggs LJ. 1955. Maximum superheating of water as a measure of negative pressure. *J. Appl. Phys.* 26 : 1001-3
- Bussmann M, Mostaghimi J, Chandra S. 1999. On a three-dimensional volume tracking model of droplet impact. *Phys. Fluids.* 11 : 1406-17
- Butt H, Cappella B, Kappl M. 2005. Force measurements with the atomic force microscope: Technique, interpretation and applications. *Surface Science Reports.* 59 : 1-152
- Carey VP. 1992. *Liquid-vapor phase-change phenomena*, Taylor and Francis. 672pp
- Chen T, Chung JN. 2003a. Heat-transfer effects of coalescence of bubbles from various site distributions. *Proceedings: Mathematical, Physical and Engineering Sciences.* 459 : 2497-527
- Chen T, Chung JN. 2002. Coalescence of bubbles in nucleate boiling on microheaters. *Int. J. Heat Mass Transfer.* 45 : 2329-41
- Chen T, Chung JN. 2003b. An experimental study of miniature-scale pool boiling. *J. Heat Transfer.* 125 : 1074-86
- Chen T, Klausner JF, Chung JN. 2004. Subcooled boiling heat transfer and dryout on a constant temperature microheater. *Int J Heat Fluid Flow.* 25 : 274-87
- Chen W, Fish J. 2006. A generalized space-time mathematical homogenization theory for bridging atomistic and continuum scales. *Int J Numer Methods Eng.* 67 : 253-71
- Chen X, Wu NJ, Smith L, Ignatiev A. 2004. Thin-film heterostructure solid oxide fuel cells. *Appl. Phys. Lett.* 84 : 2700-2
- Chu J-, Izveko S, Voth GA. 2006. The multiscale challenge for biomolecular systems: Coarse-grained modeling. *Molecular Simulation.* 32 : 211

- Daiguji H, Hihara E. 1999. Molecular dynamics study of the liquid-vapor interface of lithium bromide aqueous solutions. *Heat and Mass Transfer*. 35 : 213-9
- Davidson MR. 2000. Boundary integral prediction of the spreading of an inviscid drop impacting on a solid surface. *Chemical Engineering Science*. 55 : 1159-70
- de Andrade J, Stassen H. 2004. Molecular dynamics studies of thermal conductivity time correlation functions. *Journal of Molecular Liquids*. 110 : 169-76
- Delgado-Buscalioni R, Coveney PV. 2003. Continuum-particle hybrid coupling for mass, momentum, and energy transfers in unsteady fluid flow. *Phys Rev E*. 67 : 046704
- Dhir VK, Liaw SP. 1989. Framework for a unified model for nucleate and transition pool boiling. *ASME J. Heat Transfer*. 111 : 739-46
- Dhir VK. 2006. Mechanistic prediction of nucleate boiling heat transfer--achievable or a hopeless task? *J. Heat Transfer*. 128 : 1-12
- Dhir VK. 2001. Numerical simulations of pool-boiling heat transfer. *AICHE J*. 47 : 813-34
- Ding H, Spelt PDM. 2007. Inertial effects in droplet spreading: A comparison between diffuse-interface and level-set simulations. *J. Fluid Mech*. 576 : 287-96
- Ding H, Spelt PDM. 2007. Wetting condition in diffuse interface simulations of contact line motion. *Phys Rev E*. 75 : 046708
- Drazer G, Khusid B, Koplík J, Acrivos A. 2005. Wetting and particle adsorption in nanoflows. *Phys. Fluids*. 17 : 017102
- Dussan V. EB. 1976. The moving contact line: The slip boundary condition. *Journal of Fluid Mechanics Digital Archive*. 77 : 665-84
- Dussan V. EB, Davis SH. 1974. On the motion of a fluid-fluid interface along a solid surface. *Journal of Fluid Mechanics Digital Archive*. 65 : 71-95
- Dussan EB. 1979. On the spreading of liquids on solid surfaces: Static and dynamic contact lines. *Annu. Rev. Fluid Mech*. 11 : 371-400
- Fedorchenko AI, Wang A, Wang Y. 2005. Effect of capillary and viscous forces on spreading of a liquid drop impinging on a solid surface. *Phys. Fluids*. 17 : 093104
- Fisher JC. 1948. The fracture of liquids. *J. Appl. Phys*. 19 : 1062-7
- Flekkoy EG, Wagner G, Feder J. 2000. Hybrid model for combined particle and continuum dynamics. *EPL (Europhysics Letters)*. 52 : 271-6
- Francois M, Shyy W. 2003. Computations of drop dynamics with the immersed boundary method, part 2. Drop impact and heat transfer. *Numerical Heat Transfer, Part B: Fundamentals: An International Journal of Computation and Methodology*. 44 : 119

- Fuentes J, Cerro RL. 2007. Surface forces and inertial effects on moving contact lines. *Chemical Engineering Science*. 62 : 3231-41
- Fukai J, Zhao Z, Poulikakos D, Megaridis CM, Miyatake O. 1993. Modeling of the deformation of a liquid droplet impinging upon a flat surface. *Phys. Fluids A*. 5 : 2588-99
- Fukai J, Tanaka M, Miyatake O. 1998. Maximum spreading of liquid droplets colliding with flat surfaces. *J. Chem. Eng. Japan*. 31 : 456-61
- Genske P, Stephan K. 2006. Numerical simulation of heat transfer during growth of single vapor bubbles in nucleate boiling. *International Journal of Thermal Sciences*. 45 : 299-309
- Gentner F, Rioboo R, Baland JP, De Coninck J. 2004. Low inertia impact dynamics for nanodrops. *Langmuir*. 20 : 4748-55
- Gunjal PR, Ranade VV, Chaudhari RV. 2005. Dynamics of drop impact on solid surface: Experiments and VOF simulations. *AIChE J*. 51 : 59-78
- Hadjiconstantinou NG. 1999. Hybrid Atomistic–Continuum formulations and the moving contact-line problem. *Journal of Computational Physics*. 154 : 245-65
- Hamaker HC. 1937. The London—van der waals attraction between spherical particles. *Physica*. 4 : 1058-72
- Han DG, Choi GM. 1998. Computer simulation of the electrical conductivity of composites: The effect of geometrical arrangement. *Solid State Ionics*. 106 : 71-87
- Hanasaki I, Nakatani A, Kitagawa H. 2004. Molecular dynamics study of ar flow and he flow inside carbon nanotube junction as a molecular nozzle and diffuser. *Science and Technology of Advanced Materials*. 5 : 107-13
- Haramura Y, Katto Y. 1983. A new hydrodynamic model of critical heat flux, applicable widely to both pool and forced convection boiling on submerged bodies in saturated liquids. *Int. J. Heat Mass Transfer*. 26 : 389-99
- Hirschfelder JO. 1954. *Molecular theory of gases and liquids*, New York: Wiley. 1249pp
- Huh C, Scriven LE. 1971. Hydrodynamic model of steady movement of a solid/liquid/fluid contact line. *J. Colloid Interface Sci*. 35 : 85-101
- Ingebrigtsen T, Toxvaerd S. 2007. Contact angles of lennard-jones liquids and droplets on planar surfaces. *The Journal of Physical Chemistry C*. 111 : 8518-23
- Israelachvili J, Israelachvili JN. 1992. *Intermolecular and surface forces*, Academic Press London. 450pp. 2nd ed.
- Izvekov S, Voth GA. 2005. A multiscale coarse-graining method for biomolecular systems. *The Journal of Physical Chemistry B*. 109 : 2469-73

- Johnston HL, Grilly ER. 1942. Viscosities of carbon monoxide, helium, neon, and argon between 80Å° and 300Å°K. coefficients of viscosity. *J. Phys. Chem.* 46 : 948-63
- Kandlikar SG, Kuan WK, Mukherjee A. 2005. Experimental study of heat transfer in an evaporating meniscus on a moving heated surface. *J.Heat Transfer.* 127 : 244-52
- Kimura T, Maruyama S. 2003. *A molecular dynamics simulation of water droplet in contact with a platinum surface. Presented at 6th ASME/JSME Thermal Engg. Conf. Hawaii, 2003, A1-183.*
- Klein SA. 2007. *EES manual for windows, F-chart software,*
- Koplik J, Banavar JR, Willemsen JF. 1989. Molecular dynamics of fluid flow at solid surfaces. *Physics of Fluids A.* 1 : 781
- Koplik J, Banavar JR, Willemsen JF. 1988. Molecular dynamics of poiseuille flow and moving contact lines. *Phys. Rev. Lett.* 60 : 1282
- Liao J, Mei R, Klausner JF. 2004. The influence of the bulk liquid thermal boundary layer on saturated nucleate boiling. *Int J Heat Fluid Flow.* 25 : 196-208
- Lienhard JH, Dhir VK. 1973. *Extended hydrodynamic theory of the peak and minimum pool boiling heat fluxes. Rep. CR-2270, NASA,*
- Liu J, Chen S, Nie X, Robbins MO. 2007. A continuum–atomistic simulation of heat transfer in micro- and nano-flows. *Journal of Computational Physics.* 227 : 279-91
- Lunkad SF, Buwa VV, Nigam KDP. 2007. Numerical simulations of drop impact and spreading on horizontal and inclined surfaces. *Chemical Engineering Science.* 62 : 7214-24
- Mareschal M, Baus M, Lovett R. 1997. The local pressure in a cylindrical liquid--vapor interface: A simulation study. *J. Chem. Phys.* 106 : 645-54
- Markvoort AJ, Hilbers PAJ, Nedeá SV. 2005. Molecular dynamics study of the influence of wall-gas interactions on heat flow in nanochannels. *Phys. Rev. E.* 71 : 066702
- Martín ME, Aguilar MA, Chalmet S, Ruiz-López MF. 2002. An iterative procedure to determine lennard-jones parameters for their use in quantum mechanics/molecular mechanics liquid state simulations. *Chem. Phys.* 284 : 607-14
- Maruyama S, Kimura T. 2000. A molecular dynamics simulation of a bubble nucleation on solid surface. *Int. J. Heat Tech.* 18 : 69-74
- Maruyama S, Kimura T. 1999. A study on thermal resistance over a solid-liquid interface by the molecular dynamics method. *Therm. Sci. Eng.* 7 : 63

- Maruyama S, Kurashige T, Matsumoto S, Yamaguchi Y, Kimura T. 1 February 1998. Liquid droplet in contact with a solid surface. *Microscale Thermophysical Engineering*. 2 : 49,62(14)
- Michels A, Wijker H, Wijker H. 1949. Isotherms of argon between 0°C and 150°C and pressures up to 2900 atmospheres. *Physica*. 15 : 627-33
- Moffatt HK. 1964. Viscous and resistive eddies near a sharp corner. *Journal of Fluid Mechanics Digital Archive*. 18 : 1-18
- Moore FD, Mesler RB. 1961. The measurement of rapid surface temperature fluctuations during nucleate boiling of water. *AICHE J*. 7 : 620-4
- Mukherjee A, Dhir VK. 2004. Study of lateral merger of vapor bubbles during nucleate pool boiling. *J. Heat Transfer*. 126 : 1023-39
- Mukherjee A, Kandlikar SG. 2007. Numerical study of single bubbles with dynamic contact angle during nucleate pool boiling. *Int. J. Heat Mass Transfer*. 50 : 127-38
- Mukherjee A, Kandlikar SG. 2006. Numerical study of an evaporating meniscus on a moving heated surface. *J. Heat Transfer*. 128 : 1285-92
- Nagayama G, Cheng P. 2004. Effects of interface wettability on microscale flow by molecular dynamics simulation. *International Journal of Heat and Mass Transfer*. 47 : 501-13
- Nagayama G, Tsuruta T, Cheng P. 2006. Molecular dynamics simulation on bubble formation in a nanochannel. *Int. J. Heat Mass Transfer*. 49 : 4437-43
- Nie X, Robbins MO, Chen S. 2006. Resolving singular forces in cavity flow: Multiscale modeling from atomic to millimeter scales. *Phys. Rev. Lett*. 96 : 134501
- Nijmeijer MJP, Bakker AF, Bruin C, Sikkenk JH. 1988. A molecular dynamics simulation of the lennard-jones liquid--vapor interface. *J. Chem. Phys*. 89 : 3789-92
- NIST chemistry webbook. <http://webbook.nist.gov/chemistry/fluid/>
- Nosonovsky M, Bhushan B. 2008. Phase behavior of capillary bridges: Towards nanoscale water phase diagram. *Physical chemistry chemical physics : PCCP*. 10 :
- Nukiyama S. 1934. The maximum and minimum values of heat transmittal from metal to boiling water under atmospheric pressure. *J. Japan Soc. Mech. Eng*. 37 : 367
- O'Connell ST, Thompson PA. 1995. Molecular dynamics-continuum hybrid computations: A tool for studying complex fluid flows. *Phys Rev E*. 52 : R5792
- Ohara T, Suzuki D. 2000. Intermolecular energy transfer at a solid-liquid interface. *Nanoscale and Microscale Thermophysical Engineering*. 4 : 189

- Panchamgam SS, Chatterjee A, Plawsky JL, Wayner Jr. PC. 2008. Comprehensive experimental and theoretical study of fluid flow and heat transfer in a microscopic evaporating meniscus in a miniature heat exchanger. *Int. J. Heat Mass Transfer*. 51 : 5368-79
- Park H, Carr WW, Zhu J, Morris JF. 2003. Single drop impaction on a solid surface. *AICHE J*. 49 : 2461-71
- Park SH, Weng JG, Tien CL. 2001. A molecular dynamics study on surface tension of microbubbles. *Int. J. Heat Mass Transfer*. 44 : 1849-56
- Pasandideh-Fard M, Qiao YM, Chandra S, Mostaghimi J. 1996. Capillary effects during droplet impact on a solid surface. *Phys. Fluids*. 8 : 650-9
- Phan CM, Nguyen AV, Evans GM. 2006. Combining hydrodynamics and molecular kinetics to predict dewetting between a small bubble and a solid surface. *J. Colloid Interface Sci*. 296 : 669-76
- Priezjev NV. 2007. Rate-dependent slip boundary conditions for simple fluids. *Phys. Rev. E*. 75 : 051605
- Qian T, Wang X, Sheng P. 2006. A variational approach to moving contact line hydrodynamics. *J. Fluid Mech*. 564 : 333-60
- Rapaport DC. 1995. *The art of molecular dynamics simulation*, Cambridge ; New York: Cambridge University Press. 400pp
- Reznik SN, Yarin AL. 2002. Spreading of an axisymmetric viscous drop due to gravity and capillarity on a dry horizontal wall. *Int. J. Multiphase Flow*. 28 : 1437-57
- Sadasivan P, Unal C, Nelson R. 1995. Perspective: Issues in CHF modeling---the need for new experiments. *J. Heat Transfer*. 117 : 558-67
- Sadus RJ. 1999. *Molecular simulation of fluids*, Amsterdam: Elsevier Science. 552pp
- Sakashita H, Kumada T. 19930815. A new model for CHF in pool boiling at higher pressure. *JSME international journal.Ser.B, Fluids and thermal engineering*. 36 : 422-8
- Schoen PAE, Poulidakos D, Arcidiacono S. 2005. Phase change of a confined subcooled simple liquid in a nanoscale cavity. *Phys Rev E*. 71 : 041602
- Shi Q, Izvekov S, Voth G. 2006. Mixed atomistic and coarse-grained molecular dynamics: Simulation of a membrane-bound ion channel. *The Journal of Physical Chemistry B*. 110 : 15045-8
- Shikhmurzaev YD. 2006. Singularities at the moving contact line. mathematical, physical and computational aspects. *Physica D*. 217 : 121-33

- Sikalo S, Wilhelm H-, Roisman IV, Jakirlic S, Tropea C. 2005. Dynamic contact angle of spreading droplets: Experiments and simulations. *Phys. Fluids*. 17 : 062103
- Son G. 2001. A numerical method for bubble motion with phase change. *Numerical Heat Transfer, Part B: Fundamentals: An International Journal of Computation and Methodology*. 39 : 509
- Spijker P, ten Eikelder, H. M. M., Markvoort AJ, Nedeja SV, Hilbers PAJ. 2008. Implicit particle wall boundary condition in molecular dynamics. *Proceedings of the Institution of Mechanical Engineers -- Part C -- Journal of Mechanical Engineering Science*. 222 : 855-64
- Stoddard SD, Ford J. 1973. Numerical experiments on the stochastic behavior of a lennard-jones gas system. *Phys. Rev. A*. 8 : 1504
- Stokes RJ, Evans DF. 1996. *Fundamentals of interfacial engineering*, New York: VCH Publishers. 701pp
- Sutmann G. 2002. *Classical molecular dynamics, quantum simulations of complex many-body systems: From theory to algorithms - lecture notes. NIC Series. Rep. 10*,
- Tas NR, Mela P, Kramer T, Berenschot JW, van dB. 2003. Capillarity induced negative pressure of water plugs in nanochannels. *Nano Letters*. 3 : 1537-40
- Thompson PA, Brinckerhoff WB, Robbins MO. 1993. Microscopic studies of static and dynamic contact angles. *J. Adhes. Sci. Technol.* 7 : 535,554(20)
- Thompson PA, Robbins MO. 1989. Simulations of contact-line motion: Slip and the dynamic contact angle. *Phys. Rev. Lett.* 63 : 766
- Thompson PA, Troian SM. 1997. A general boundary condition for liquid flow at solid surfaces. *Nature*. 389 : 360-2
- Tomar G, Biswas G, Sharma A, Agrawal A. 2005. Numerical simulation of bubble growth in film boiling using a coupled level-set and volume-of-fluid method. *Phys. Fluids*. 17 : 112103
- Tyree MT. 2003. Plant hydraulics: The ascent of water. *Nature*. 423 : 923-
- Voronov RS, Papavassiliou DV, Lee LL. 2006. Boundary slip and wetting properties of interfaces: Correlation of the contact angle with the slip length. *J. Chem. Phys.* 124 : 204701
- Wagner G, Flekkoy E, Feder J, Jossang T. 1 August 2002. Coupling molecular dynamics and continuum dynamics. *Comput. Phys. Commun.* 147 : 670,673(4)
- Wayner Jr. PC. 1999. Intermolecular forces in phase-change heat transfer: 1998 kern award review. *AIChE J.* 45 : 2055-68

- Wemhoff AP, Carey VP. 2005. Molecular dynamics exploration of thin liquid films on solid surfaces. 1. monatomic fluid films. *Nanoscale and Microscale Thermophysical Engineering*. 9 : 331
- Weng J, Park S, Lukes JR, Tien C. 2000. Molecular dynamics investigation of thickness effect on liquid films. *J. Chem. Phys.* 113 : 5917-23
- Wu CYW. 2003. A molecular dynamics simulation of bubble nucleation in homogeneous liquid under heating with constant mean negative pressure. *Nanoscale and Microscale Thermophysical Engineering*. 7 : 137
- Wu J, Dhir VK, Qian J. 2007. Numerical simulation of subcooled nucleate boiling by coupling level-set method with moving-mesh method. *Numerical Heat Transfer, Part B: Fundamentals: An International Journal of Computation and Methodology*. 51 : 535
- Wu YW, Pan C. 2006. Molecular dynamics simulation of thin film evaporation of Lennard-Jones liquid. *Nanoscale and Microscale Thermophysical Engineering*. 10 : 157
- Xu JL, Zhou ZQ. 2004. Molecular dynamics simulation of liquid argon flow at platinum surfaces. *Heat and Mass Transfer*. 40 : 859-69
- Xu J, Li Y. 2007. Boundary conditions at the solid–liquid surface over the multiscale channel size from nanometer to micron. *International Journal of Heat and Mass Transfer*,. 50 : 2571-81
- Yamamoto M, Kinoshita M, Kakiuchi T. 2000. Structure of the pt(111)/liquid interface: A first-principles/RHNC calculation. *Electrochim. Acta*. 46 : 165-74
- Yang S. 2006. Effects of surface roughness and interface wettability on nanoscale flow in a nanochannel. *Microfluidics and Nanofluidics*. 2 : 501-11
- Yang SH, Nosonovsky M, Zhang H, Chung K. 2008. Nanoscale water capillary bridges under deeply negative pressure. *Chemical Physics Letters*. 451 : 88-92
- Yi P, Poulikakos D, Walther J, Yadigaroglu G. 2002. Molecular dynamics simulation of vaporization of an ultra-thin liquid argon layer on a surface. *International Journal of Heat and Mass Transfer*. 45 : 2087-100
- Zhang ZM. 2007. *Nano/microscale heat transfer*, New York, NY: McGraw-Hill. 479pp
- Ziarani AS, Mohamad AA. 2008. Effect of wall roughness on the slip of fluid in a microchannel. *Nanoscale and Microscale Thermophysical Engineering*. 12 : 154
- Zuber N. 1959. *Hydrodynamic aspects of boiling heat transfer*. Rep. AEC Report No. AECU-4439

BIOGRAPHICAL SKETCH

Shalabh Chandra Maroo was born in 1982, in Bhilai, India. He attended high school at Deepika E. M. School in Rourkela, India and graduated in 1999. He competed in Indian Institute of Technology-Joint Entrance Examinations and was selected for bachelor's program in mechanical engineering at Indian Institute of Technology (IIT), Bombay, India. He received his Bachelor of Technology degree from IIT Bombay in 2003. Following graduation, he was admitted to the graduate program in mechanical engineering at the University of Florida in August, 2003. In December 2005, he completed his research work for a Master of Science degree with Dr. D. Yogi Goswami on 'Theoretical Analysis of Solar Driven Flash Desalination System based on Passive Vacuum Generation'. Shalabh joined Dr. Jacob N. Chung's research group in mechanical engineering at the University of Florida in January 2006 for this doctoral research work. He completed his research work for the Doctor of Philosophy degree in Fall 2009.